Main Manuscript for

Dysfunctional S1P/S1PR1 signaling in the dentate gyrus drives vulnerability of chronic pain-related memory impairment

Mengqiao Cui[1,2,3#], Xiaoyuan Pan[1,2,3#], Zhijie Fan[1,2,3#], Shulin Wu[1,2,3], Ran Ji[1,2,3], Xianlei Wang[1,2,3], Xiangxi Kong[1,2,3], Zhou Wu[1,2,3], Lingzhen Song[1,2,3], Weiyi Song[1,2,3,4], Jun-Xia Yang[1,2,3], Hongjie Zhang[5], Hongxing Zhang[1,2,3], Hai-Lei Ding[1,2,3*], Jun-Li Cao[1,2,3,6*]

[1] Jiangsu Province Key Laboratory of Anesthesiology, Xuzhou Medical University, Xuzhou, Jiangsu 221004, China.

[2] Jiangsu Province Key Laboratory of Anesthesia and Analgesia Application Technology, Xuzhou Medical University, Xuzhou, Jiangsu 221004, China.

[3] NMPA Key Laboratory for Research and Evaluation of Narcotic and Psychotropic Drugs, Xuzhou Medical University, Xuzhou, Jiangsu 221004, China.

[4] School of Public Health, Xuzhou Medical University, Xuzhou, Jiangsu 221004, China

[5] Faculty of Health Sciences, University of Macau, Taipa, Macau, China.

[6] Department of Anesthesiology, the Affiliated Hospital of Xuzhou Medical University, Xuzhou, Jiangsu 221004, China.

[#] These authors contributed equally to this work.

* Correspondence should be addressed:

E-mail: haileimdar@yahoo.com (H.L.D.) and caojl0310@aliyun.com (J.L.C.)

Author Contributions: J-L.C., H-L.D., H.Z. and M.C. conceived the idea, M.C., X.P., Z.F., S.W., R.J., X.W., X.K., Z.W., L.S., W.S., and J-X.Y. performed the experimental research, M.C., X.P. and Z.F. drafted the original manuscript, J-L.C., H-L.D., H.Z. and H.Z. edited the manuscript. All the authors read and approved the final manuscript.

Competing Interest Statement: The authors have declared that no conflict of interest exists.

Abstract

Memory impairment in chronic pain patients is substantial and common, and few therapeutic strategies are available. Chronic pain-related memory impairment has susceptible and unsusceptible features. Therefore, exploring the underlying mechanisms of its vulnerability is essential for developing effective treatments. Here, combining two spatial memory tests (Y-maze test and Morris water maze), we segregated chronic pain mice into memory impairment-susceptible and -unsusceptible subpopulations in a chronic neuropathic pain model induced by chronic constrictive injury of the sciatic nerve. RNA-seq analysis and gain/loss-of-function study revealed that S1P/S1PR1 signaling is a determinant for vulnerability to chronic pain-related memory impairment. Knockdown of the S1PR1 in the DG promoted a susceptible phenotype and led to structural plasticity changes of reduced excitatory synapse formation and abnormal spine morphology as observed in susceptible mice, while overexpression of the S1PR1 and pharmacological administration of S1PR1 agonist in the DG promoted an unsusceptible phenotype and prevented the occurrence of memory impairment, and rescued the morphological abnormality. Finally, GO enrichment analysis and biochemical evidence indicated that down-regulation of S1PR1 in susceptible mice may impair DG structural plasticity via interaction with actin cytoskeleton rearrangement-related signaling pathways including Itga2 and its downstream Rac1/Cdc42 signaling and Arp2/3 cascade. These results reveal a novel mechanism and provide a promising preventive and therapeutic molecular target for vulnerability to chronic pain-related memory impairment.

Keywords: Chronic pain; memory; dentate gyrus; sphingosine 1-phosphate; synaptic plasticity.

Introduction

Clinical and preclinical studies have demonstrated that chronic pain impairs memory or accelerates memory decline (1-3). Memory impairment is also a potential contributing factor to the maintenance of chronic pain and poor treatment response (2, 4, 5). Although memory deficits in chronic pain patients are substantial and common, some clinical observations indicate high heterogeneity (1, 6), suggesting that chronic pain-related memory impairment exhibits susceptible and unsusceptible features. However, few preclinical studies model this clinical scenario and explore its underlying mechanisms.

Findings from both human and animal studies have indicated that cognitive dysfunction associated with chronic pain is linked to structural and functional deficits within the hippocampus (7-11). In particular, the dentate gyrus (DG), as part of the hippocampus, plays a crucial role in memory formation processing (12, 13). The DG has been postulated to perform a variety of mnemonic tasks, such as pattern separation (14), novelty detection (15), and processing information related to spatial contexts (16). Nevertheless, the impact of pain-related cognitive syndromes on the dendritic morphologies of DG neurons, such as dendritic complexity, is inconsistent across different studies (7, 8, 17), and the molecular mechanisms remain minimally understood. The principal cell type of the DG is the dentate granule cells (DGCs), which are divided into immature and mature ones (18). Immature newborn DGCs undergo neurogenesis and play key roles in learning and memory due to their high excitability and enhanced synaptic plasticity (19, 20). Our previous study found that mice with chronic pain-related memory impairment showed significantly reduced adult neurogenesis in the DG (9). Contrarily, mature DGCs are less excitable and exhibit reduced synaptic plasticity to an extent, but emerging evidence suggests that this cell population is equally recruited in memory formation (21-25). It is intriguing to understand how mature DGCs would change in the state of chronic pain and by what molecular mechanism they facilitate chronic pain-related memory impairment.

Sphingosine 1-phosphate (S1P) is a bioactive sphingolipid metabolite, functioning as a key signaling molecule in a variety of cellular processes, such as cell division, adhesion, migration, and death (26-28). S1P acts both through extracellular and intracellular modes (27-29). In its extracellular mode, increasing evidence has suggested that the S1P system is a modulator of pain and memory processing pathways through S1P receptors 1-5 (S1PR1-5), particularly S1PR1. For instance, in models of traumatic nerve injury, astrocyte-mediated S1PR1

neuroinflammation contributes to central sensitization through increased S1P production and IL-1β release in the spinal cord, and beneficial effects of pain alleviation can be observed following IL-10-dependent S1PR1 antagonism (30). While there is evidence on S1P signaling regulating pain perception in the spinal cord, its role in higher pain centers remains largely unexplored. In regard to S1P function in memory processing, a recent study has hinted at the possibility of CNS S1PR1 agonism in the cellular repositioning of new DGCs and in regulating the integration of new neurons into pre-existing circuits, which may govern the process of memory formation (31). Additionally, activation of S1PR1 after traumatic brain injury in rats can significantly enhance neurogenesis and neurocognitive function (32). Importantly, increasing evidence suggests that the S1P receptor signaling pathway has profound effects on the regulation of synaptic strength, including modulating synaptic architecture and plasticity, and mediating excitatory synaptic transmission in the hippocampus (33-35). However, there is limited understanding regarding the involvement of S1P signaling in chronic pain-related memory impairment, as well as the interactive pathways that may underlie the effects.

In the present study, by employing an array of techniques including rodents-based behavioral tests, RNA-Seq, imaging, pharmacological and biochemical approaches, we elucidated a pivotal role of S1PR1 within the hippocampal DG in the context of chronic pain associated memory impairment. Memory impairment-susceptible mice exhibited decreased S1PR1 expression in the hippocampal DG. Knockdown of S1PR1 in the DG facilitated the development of a vulnerable phenotype and led to abnormal structural plasticity in DGCs. Conversely, overexpression of S1PR1 or pharmacological administration of an S1PR1 agonist in the DG, promoted an unsusceptible phenotype, thereby averting the onset of memory impairment, and alleviated morphological abnormalities in DGCs. Subsequent mechanistic investigation demonstrated that, loss of S1PR1 in the DG results in actin dysregulation via interaction with integrin α2 (ITGA2) and its downstream Rac1/Cdc42 signaling and Arp2/3 cascade, leading to abnormal structural synaptic plasticity and ultimately causes memory impairment. Taken together, this study identified potential molecular mechanisms and promising therapeutic targets for preventing and treating vulnerability to memory impairment associated with chronic pain.

Results

Segregation of chronic pain mice into memory impairment-susceptible and -unsusceptible subpopulations

We utilized sciatic nerve chronic constriction injury (CCI) in C57BL/6J mice to model chronic pain state and tested the memory performance of mice with chronic neuropathic pain. CCI induced long-lasting mechanical allodynia (Supplemental Figure 1A) and thermal hyperalgesia (Supplemental Figure 1B). No significant change in locomotor functions was observed in these injured mice (Supplemental Figure 1C and 1D). Consistent with our recent study (9), only chronic (21~28 days, referred to as CCI-Chronic) and not acute (5~7 days, referred to as CCI-Acute) exposure to constrictive injury-induced neuropathic pain impaired spatial memory formation in both Y-maze test (Figure 1A, B, D, E) and Morris water maze (MWM) test (Figure 1A, C, F, G).

To investigate whether memory impairment has susceptible and unsusceptible features in CCI-induced chronic neuropathic pain mice, we analyzed results from Y-maze and MWM tests using the k-means clustering algorithm and segregated into two clusters in a large number of CCI mice (k=2). After assigning each data point to its closest k-center, we drew a median between both the centroids as a cutoff value. One cluster, including mice displaying a ratio of time more than the cutoff value, was defined as the unsusceptible mouse cluster. The other cluster, including mice exhibiting a ratio of time less than the cutoff value, was defined as the susceptible mouse cluster. Using this algorithm, a ratio of 40% (percent time spent in the novel arm) and a ratio of 36% (percent time in the target quadrant) were set as cutoff values for Y-maze test (Figure 1E, left) and MWM test (Figure 1G, left), respectively. Accordingly, in the Y maze test, 43% of CCI-Chronic mice were unsusceptible, and the remaining 57% were susceptible (Figure 1E, right). In the MWM test, 52% of CCI-Chronic mice were unsusceptible, and 48% were susceptible (Figure 1G, right).

We then used a four-quadrant chart to plot the data of CCI-Chronic mice memory performance for examining the consistency between the two behavioral assays. One variable, the percent time in the quadrant, was represented on the x-axis, and another variable, the percent time in the novel arm, was represented on the y-axis. The quadrants are determined by dividing the chart into four parts based on the cutoff values of Y-maze and MWM tests. As shown in the chart (Figure 1H, left), quadrant 1 (top right) and 3 (bottom left) respectively displayed

unsusceptible and susceptible mice in both Y-maze and MWM tests, while quadrant 2 (top left) and 4 (bottom right) displayed mice unsusceptible in one test but susceptible in the other one. The bar graph (Figure 1H, right) showed that the majority of CCI-Chronic mice exhibited consistent memory performance in the two behavioral tests (Susceptible: 47%; unsusceptible: 43%), and only 10% of mice displayed susceptibility in a single test (Y maze: 8%; MWM, 2%), suggesting good agreement between the two different assays. Given that the MWM test cannot be conducted once a week for multiple repeated measurements for the same batch of mice, the Y maze test was used to investigate the duration of memory impairment induced by chronic pain. The results showed that memory impairment can last at least 63 days post CCI surgery, providing a workable time window for further investigations (Supplemental Figure 2A, B).

We next examined whether the susceptibility or insusceptibility to memory impairment in mice with chronic pain is associated with the pain threshold. Linear regression, followed by a goodness-of-fit measure of R-squared (r^2), was used to determine the correlation between the two variables: percent time spent in the novel arm and pain threshold, or percent time in the target quadrant and pain threshold. The statistics revealed no correlation between memory performance for each mouse against its thermal pain threshold (r^2=0.04, Supplemental Figure 3A; r^2=0.05, Supplemental Figure 3B). Furthermore, we administered the CCI-Chronic mice with the *selective COX-2 inhibitor* NSAID analgesic meloxicam. Recommended doses for meloxicam in mice range from 1 to 10 mg/kg *i.p.* (36), and the duration of action (10mg/kg) lasts at least 24 hrs on day 7 post intraperitoneal injection once daily (Supplemental Figure 4). Here, CCI-Chronic mice were subjected to pain treatment by meloxicam (10mg/kg) for 7 days (once daily from day 28 to 34 post CCI) (Figure 1I). During the duration of analgesic effects (day 34~35 post CCI) (Figure 1I), we conducted the Y-maze test and found that the analgesia could not relieve the memory impairment (Figure 1J). Consistently, the percentage of susceptible and unsusceptible mice remained stable (Figure 1K), further indicating that the susceptibility or insusceptibility to memory impairment is marginally correlated with the pain tolerance of mice.

S1PR1 expression is decreased in the hippocampal DG of susceptible mice

Hippocampal DG plays a vital role in learning and memory formation. To identify molecular mechanisms possibly contributing to susceptibility to memory impairment, we analyzed the hippocampal DG by RNA-Seq on day 28 after CCI when the mice with chronic pain were

segregated into unsusceptible and susceptible subpopulations by Y-maze and MWM tests. We detected a total of 510 differentially expressed genes (DEGs) between Sham and susceptible mice, with 330 genes (65%) upregulated and 180 genes (35%) downregulated (Figure 2A). We noticed that KEGG analysis revealed significant enrichment of six downregulated genes in the lipid metabolism pathway for Sham versus susceptible mice (Figure 2B and 2C). Combining the trend analysis of Sham versus unsusceptible versus susceptible mice, we found in the trend pattern of Figure 2D (Left: Sham; middle, unsusceptible; right: susceptible), sphingolipid metabolism was significantly enriched (Figure 2E). In particular, transcription of *Sptlc3* was downregulated (Figure 2C and 2E). *Sptlc3* encodes the subunit of the serine palmitoyltransferase (SPT) which catalyzes the rate-limiting step in sphingolipid biosynthesis (37). Defective SPT leads to disturbed sphingolipid homeostasis and failure of the subsequent production of metabolites such as glucosylceramide (38) and sphingosine 1-phosphate (S1P) (39), contributing to the occurrence of biological disorders. Previous studies have found that S1P/S1PR1 signaling is highly involved in hippocampus-engaged behaviors (31), we then verified the expression of S1PR1 in the hippocampal DG by Western blotting (WB), with no change of S1PR1 observed on day 7 after CCI (Figure 2F and 2H) but significant downregulation in susceptible mice compared with Sham and unsusceptible ones (Figure 2G and 2I).

Furthermore, we characterized the expression profile of S1PR1 in the hippocampal DG. Immunofluorescence staining results showed that S1PR1 was mostly co-expressed with neuronal nuclear protein (NeuN) in neurons and merely co-expressed with glial fibrillary acidic protein (GFAP) in astrocytes or ionized calcium-binding adaptor molecule 1 (Iba1) in microglia (Supplemental Figure 5A and 5C). We also detected S1PR1 was highly co-expressed with calcium-calmodulin (CaM)-dependent protein kinase II (CaMKII)-expressing excitatory neurons but sparsely with glutamic acid decarboxylase 67 (GAD67)-expressing inhibitory neurons (Supplemental Figure 5B and 5D). Taken together, these findings raised the possibility that S1P/S1PR1 may participate in the occurrence of chronic pain-related memory impairment.

Knockdown of S1PR1 in the hippocampal DG promotes memory impairment susceptibility

To figure out the causal link between S1PR1 and chronic pain-related memory impairment, we generated recombinant adeno-associated virus 2/9 (AAV2/9) expressing a small hairpin RNA targeting S1PR1 (rAAV-CaMKIIa-EGFP-5'miR-30a-shRNA(S1pr1)-3'-miR30a-WPREs, the shRNA sequence is provided in Supplemental Table 1). Following the schematic experimental procedure shown in Figure 3A, intra-DG injection was conducted (Figure 3B and Supplemental Figure 6A). We first confirmed the knockdown efficiency of the virus in the hippocampal DG using WB (Figure 3C). We then examined the effects of knockdown of S1PR1 in the DG on pain threshold. Compared with mice expressing scramble shRNA, mice expressing shS1pr1 in the DG had no effects on pain sensation (Figure 3D). Next, we assessed the effects of loss of S1PR1 in the DG on memory-related behaviors. In the Y-maze test, reduction of S1PR1 worsened the performance of Sham-treated mice by reducing the distance travelled and time spent in the novel arm, as well as enhancing the memory impairment of CCI-treated mice (Figure 3E). The results were consistent in the MWM test (Figure 3F). Consequently, knockdown of S1PR1 in the CCI-treated mice led to more susceptible mice (up to 86%) to memory impairment (Figure 3G). Thus, the above results suggest that DG S1PR1 exerts a negative regulatory effect on chronic pain-related memory impairment.

Upregulation of S1PR1 in the hippocampal DG prevents the development of memory impairment susceptibility

To gain a deeper understanding of the functional consequences of enhanced S1P/S1PR1 signaling in the hippocampal DG, we generated recombinant adeno-associated virus 2/9 (AAV2/9) expressing the S1PR1 coding sequence (rAAV-CaMKIIa-S1pr1-P2A-EGFP-WPRE-hGH-polyA, sequence referred to Supplemental Table 1). Following the experimental flowchart depicted in Figure 4A, intra-DG injection was conducted (Figure 4B and Supplemental Figure 6B). We first confirmed the overexpression efficiency of the virus in the hippocampal DG using WB (Figure 4C). Next, we assessed how S1PR1 overexpression in the DG affected pain threshold. Compared with the mice expressing the scramble shRNA, mice overexpressing S1PR1 in the DG had no effects on pain sensitization (Figure 4D). We then examined whether overexpression of S1PR1 in the DG influences chronic pain-related memory impairment according to behavioral paradigms of Y-maze and MWM tests. In the Y-maze and MWM tests, overexpression of S1PR1 in CCI-treated mice significantly improved the spatial memory

formation by promoting insusceptibility to memory impairment (up to 82%), but had no obvious effects on Sham-treated mice (Figure 4E-G).

A previous study demonstrated that chronic administration of the selective S1PR1 agonist SEW2871 for 14 days inhibited the reduction of S1PR1 expression and improved impaired spatial memory in rats (40). The dose used in the study (40, 41) was effective to induce biological responses without causing kidney and liver injuries (41). We then investigated whether a continuous 14-day local infusion of SEW2871 in the DG from day 7 post CCI could inhibit the reduction of S1PR1 expression and confer insusceptibility to memory impairment. For this purpose, a cannula was implanted into the DG of mice, and the S1PR1 agonist SEW2871 at a dose of 0.7mg/kg/day (40) was administered into the DG from day 7 to 21 post CCI surgery (Figure 5A and 5B). WB analysis revealed that bilateral DG injection of S1PR1 agonist SEW2871 inhibited the reduction of S1PR1 expression (Figure 5C), but did not alter the basal nociception of thermal stimuli (Figure 5D). In contrast, intra-DG administration of SEW2871 in CCI-treated mice significantly increased the distance traveled and time in the novel arm in the Y-maze (Figure 5E), decreased escape latency and increased percent time in the quadrant in the MWM (Figure 5F), resulting in an increased ratio (up to 80%) of unsusceptible mice (Figure 5G). Thus, it can be inferred from the above observations that upregulation of S1PR1 in the hippocampal DG promotes insusceptibility to chronic pain-related memory impairment.

S1PR1 deficiency in the hippocampal DG modulates structural plasticity of DGCs

We next questioned how DG S1P/S1PR1 signaling modulates memory impairment. Adult neurogenesis enhances the plasticity of the hippocampus (42), as well as preexisting granule neurons of the DG undergo dynamic alterations that include dendritic extension and retraction, synapse creation, and elimination (43). Given that almost all the excitatory inputs from all sources towards DGCs are situated on their dendritic spines while the inhibitory connections are distributed in different layers (18), we decided to examine the morphological changes of excitatory synapses which technically facilitates our observation. First, we utilized transmission electron microscope (TEM) to observe changes in the number of excitatory synapses and postsynaptic densities (PSD) in mice expressing shs1pr1 and scrambled shRNA (Figure 6A). In line with the behavioral tests, Sham-shS1pr1 mice showed a decreased number of excitatory synapses (Figure 6B), accompanied by a shorter PSD length and width compared with Sham-Scramble mice (Figure 6C). Furthermore, Golgi staining (Figure 6D) revealed that Sham-shS1pr1 mice had a lower dendritic intersection number (Figure 6E), shortened total dendritic

length (Figure 6F), decreased mushroom/stubby type (Figure 6G, left) spines, and no change in thin/filopodia type (Figure 6G, right) dendritic spines. Additionally, CCI-shS1pr1 mice showed even more pronounced phenotypes as described above compared with CCI-Scramble mice (Figure 6A-6G). Additionally, overexpression of S1PR1 in the DG significantly restored structural synaptic plasticity by increasing the number of excitatory synapses, PSD length and width (Figure 7A-C). Golgi staining results revealed that the intersection number of dendritic branches (Figure 7D-E), the total length of dendrites (Figure 7F), and the number of mushroom/stubby type dendritic spines (Figure 7G, left) increased in response to the intervention. Consistently, TEM images and Golgi staining revealed that continuous activation of S1PR1 in the DG significantly prevented the occurrence of defective synaptic plasticity (Figure 7H-N), indicating that activation of S1PR1 in the DG confers insusceptibility to memory impairment.

Next, we assessed whether the above structural plasticity changes can be observed in susceptible mice. First, we examined the number of neurons between susceptible and unsusceptible mice by staining for NeuN. The statistical result showed that the number is not grossly different between the two populations (Supplemental Figure 7). We then found that the synaptic structural plasticity in the hippocampal DG is disrupted in susceptible mice, but not in Sham and unsusceptible ones. TEM was also used to observe changes in the number of excitatory synapses and postsynaptic densities (PSD) (Supplemental Figure 8A and 8H). The results showed that 7-day CCI mice exhibited a similar number of excitatory synapses (Supplemental Figure 8B), as well as PSD length and width, to Sham mice (Supplemental Figure 8C). On day 21 post CCI, susceptible mice displayed a decreased number of excitatory synapses (Supplemental Figure 8I), accompanied by shortened PSD length and width compared with unsusceptible and Sham mice (Supplemental Figure 8J). Furthermore, Golgi staining was utilized to identify the dendritic formation and spine morphology (Supplemental Figure 8D and 8K). 7-day CCI mice showed no altered dendritic intersection number (Supplemental Figure 8E), total dendritic length (Supplemental Figure 8F), mushroom/stubby type (Supplemental Figure 8G, left) and thin/filopodia type (Supplemental Figure 8G, right) dendritic spines. On day 21 post CCI, susceptible mice displayed a decreased dendritic intersection number (Supplemental Figure 8L), shortened total dendritic length (Supplemental Figure 8M), and a decreased number of mushroom/stubby type dendritic spines (Supplemental Figure 8N, left) compared with unsusceptible and Sham mice. However, there were no changes in the number of thin/filopodia type (Supplemental Figure 8N, right) dendritic spines. Overall,

these findings suggest that the variation in structural plasticity of the hippocampal DG underlies susceptibility and insusceptibility to chronic pain-related memory impairment, and it is modulated by S1P/S1PR1 signaling.

Defective S1P/S1PR1 signaling induced dysregulation of actin cytoskeleton organization in susceptible mice

Neuronal structural plasticity, such as morphogenesis of dendrites and dendritic spines, is primarily regulated by the actin cytoskeleton (44, 45). Disruption of normal actin organization has been associated with numerous neurological and psychiatric diseases (46). It has been demonstrated that S1P/S1PRs modulate significant cytoskeletal rearrangements in various cellular systems through actin regulatory proteins such as Rho GTPases, including Rac1 and Cdc42 (28, 47). These proteins promote filopodia formation by stimulating actin polymerization through WAVE and the Arp2/3 complex (47, 48). Additionally, we analyzed the RNA-Seq data to identify genes that may be involved in S1PR1-regulated cytoskeletal dynamics in our animal model. In the KEGG analysis comparing Sham versus susceptible mice and the trend analysis (Sham versus unsusceptible versus susceptible mice), integrin α2 (encoded by Itga2) was found to be enriched and downregulated among cell adhesion molecules and regulation of actin cytoskeleton pathway genes (Figure 8A and 8B). Integrins serve as linkers between the extracellular matrix and intracellular actin cytoskeleton, mediating cytoskeletal organization (49). Therefore, we asked whether S1P/S1PR1 induces structural plasticity in susceptible mice by regulating actin dynamics in the DG. To address this, we verified the expression levels of actin regulatory proteins, including Rac1, Cdc42, Arp2, Arp3 and Itga2, in 7-day CCI mice (Figure 8C and 8D), unsusceptible mice, and susceptible mice (Figure 8E and 8F). To figure out the regulation is specifically S1PR1-dependent, but not through other S1PRs and Rho GTPase, we also checked the expression level of S1PR2 and Rho GTPase RhoA which interacts with S1PR2 (28, 47, 50) (Supplemental Figure 9). We observed a significant decreased in the levels of Rac1, Cdc42, Arp2, Arp3 and Itga2 in susceptible mice, but not in Sham and unsusceptible mice. As expected, there is no change in the expression level of S1PR2 and RhoA in CCI animals. To determine whether the reduction in levels of these proteins is associated with downregulated S1PR1 signaling, we examined lysates of hippocampal DG tissue extracted from S1PR1 DG conditional knockdown mice, revealing decreased levels of Rac1, Cdc42, Arp2,

Arp3 and Itga2 as assayed by WB (Figure 8G and 8H). Conversely, S1PR1 overexpression in the DG led to increased levels of Rac1, Cdc42, Arp2, Arp3 and Itga2 (Figure 8I and 8J). These data indicate that S1PR1 functions upstream of Rac1, Cdc42, Arp2/3 and Itga2. Given a previous study suggesting the involvement of an isoform of integrin ITGB4 in S1PR1-mediated Rac1 activation (51), our results raise the possibility that dysregulated actin rearrangement elicited by S1PR1 downregulation in the DG may be influenced by Itga2-dependent activation of the Rac1/Cdc42 signaling cascade and Arp2/3 dependent actin polymerization.

S1P/S1PR1 regulates actin polymerization by interaction with ITGA2

We then investigated the regulatory role of S1P/S1PR1 signaling in actin polymerization. The polymerization of monomeric actin (G-actin) into actin filaments (F-actin) to form the actin cytoskeleton frequently occurs primarily at or near the plasma membrane. The organization of actin filaments determines the shape, stiffness, and movement of the cell surface and also facilitates spine morphology and function (52). Thus, we first examined actin polymerization by quantifying the transition from G-actin to F-actin transition. Densitometric analysis of F-actin/G-actin Western blots (Figure 9A and 9B) indicated a significant decrease in the relative percentage of F-actin in the DG of susceptible mice compared with that of Sham and unsusceptible mice. Immunofluorescence observations using a fluorescently conjugated phalloidin, which binds only to F-actin, revealed that HT-22 mouse hippocampal neuronal cells with knockdown of S1PR1 had accumulated F-actin aggregates mostly around the nuclei and lost the majority of the thinner filament bundles (Figure 9C) compared with control cells. Similarly, we utilized primary hippocampal cells to investigate the neuron morphology and distribution of F-actin. We observed less branches and accumulated F-actin aggregates rather than diffused distribution compared with control cells. Furthermore, we investigated whether S1PR1 regulates actin polymerization via interaction with ITGA2. We conducted yeast two-hybrid screening *in vitro* and a co-immunoprecipitation assay *in vivo* to examine the interaction between the two proteins. To identify putative interaction between S1PR1 and ITGA2, the full sequences of S1PR1 (cloned into the pBT3-STE vector) and ITGA2 (cloned into the pPR3-C vector) were used as bait and prey, respectively (Supplemental Figure 10A and 10B). The auto-activation test showed that positive controls (the pNubG-Fe65 and pTSU2-APP vector together) grew on

the DDO (SD/-Trp/-Leu), TDO (SD/-Trp/-Leu/-His) and QDO (SD/-Trp/-Leu/-His/-Ade) plates. Meanwhile, the negative control (the pPR3-N and pTSU2-APP vectors together), the pPR3-N empty vector, and the pBT3-STE vector with s1pr1 grew on the DDO and TDO but not on the QDO plate (Supplemental Figure 11). These results indicated that S1PR1 did not exhibit auto-activation activity in yeast. Next, a yeast two-hybrid assay was performed by co-transforming pBT3-STE-s1pr1 and pPR3-C-itga2 in the NMY51 yeast strain. Yeast cells harboring both s1pr1 and itga2 grew vigorously on both DDO media and QDO/X-gal media (Figure 9D). Additionally, in a CoIP assay, total protein extracts from the mice DG were immunoprecipitated by the anti-S1PR1-specific antibody and analyzed by immunoblotting probed with the anti-S1PR1 and anti-ITGA2 antibodies with immunoglobulin G as the negative control. The in vivo CoIP assay showed that S1PR1 interacts with ITGA2 in the DG (Figure 9E). The above results indicated that S1PR1 may physically interact with ITGA2. To determine the functional interaction between S1PR1 and ITGA2 in regulating chronic pain-related memory impairment, a recombinant adeno-associated virus 2/9 (AAV2/9) expressing a small hairpin RNA targeting ITGA2 was generated (rAAV-CaMKIIa-EGFP-5'miR-30a-shRNA (Itga2)-3'-miR30a-WPREs, the sequence of shRNA referred to Supplemental Table 1). Following the schematic experimental procedure shown in Figure 9F, intra-DG injection of the ITGA2 knockdown virus was conducted (Figure 9G and Supplemental Figure 6C). We first confirmed the knockdown efficiency of the virus in the hippocampal DG using WB (Figure 9H). We then examined the effects of knockdown of ITGA2 in the DG on pain threshold and memory performance. Consistent with the effects of S1PR1 knockdown in the DG, compared with mice expressing scramble shRNA, mice expressing shItga2 in the DG had no effects on the pain sensation (Figure 9I) and worsened memory-related behaviors in the Y-maze and MWM tests (Figure 9J and 9K). To further demonstrate that S1PR1 and ITGA2 participate in the same pathway, we knocked down the two proteins at the same time (Figure 9L and 9M). As expected, it did not elicit addictive effects on behavioral tests of Y-maze and MWM tests compared to the knockdown of each one of them in isolation (Figure 9N and 9O). Overall, these findings suggest that DG S1PR1 may govern the susceptibility of memory impairment by regulating actin polymerization via interaction with ITGA2.

Discussion

The current study aimed to explore a disease model of chronic pain-related memory impairment and uncover the molecular underpinnings of both susceptibility to chronic pain-related memory impairment and factors that promote susceptibility to such variations. We established a paradigm to segregate mice with chronic pain into memory impairment-susceptible and -unsusceptible subpopulations. Susceptible mice displayed long-lasting memory impairment 21 days after CCI surgery, while unsusceptible mice continued to maintain normal memory function. Importantly, TEM and Golgi staining assays revealed that susceptible mice exhibited signs of reduced excitatory synapse formation and abnormal spine morphology in the brain area of the hippocampal DG involved in cognition/memory. Interestingly, the phenotypic variability in mice is attributed to dysregulation of S1P/S1PR1/integrin α2 signaling-induced disorganization of actin cytoskeleton through the Rac1/Cdc42 signaling and Arp2/3 cascade (Figure 10). These are significant findings that demonstrate with certainty that comorbidity of memory impairment in complicated chronic pain syndromes has a pathophysiological substrate in the brain that could be a key therapeutic target for intervention.

Several studies have shown that neuronal plastic changes in the hippocampus are highly relevant to chronic pain-induced memory impairment. For example, the hippocampal extracellular matrix (ECM) exhibits aberrated structural synaptic plasticity connected to deficiencies in working location memory in a mouse model of chronic pain. These deficits are also correlated with decreased hippocampus dendritic complexity (7). Moreover, rodents with neuropathic pain show altered short-term synaptic plasticity related to the decrease in hippocampus volume detected in patients. The anomaly may be the cause of the typical learning and emotional deficiencies seen in people with chronic pain (11). In addition, the hippocampus regions involved in the processing of pain information show abnormalities in neurite arborization, dendritic length, and dendritic spine architecture (53). Consistently, we found that hippocampal DG neurons displayed decreased excitatory synapses and altered spine morphology in susceptible mice. Although extensive investigations have proven the link between hippocampal DG function with memory formation, it remains unclear what regulates the plastic changes in the hippocampal DG, a well-studied brain area responsible for memory formation, and how it participates in the modulation of memory impairment in chronic pain. Interestingly, using RNA-Seq, we detected significant transcriptional downregulation of sphingolipid metabolism in the DG, which we verified at protein levels due to dysregulation of S1P/S1PR1 signaling. A previous study found that the expression of S1PR1 is upregulated in

freshly formed DG cells, which is required for neurite arborization and horizontal-to-radial repositioning of these cells (31). They also raised a question of whether S1PR1 regulates mature DGC activity. In the current study, we mainly focused on S1P function in mature DGCs. We knocked down DG S1PR1 and found that the loss of S1PR1 in the DG induced more susceptible mice to memory impairment without affecting pain threshold. Additionally, we also overexpressed DG S1PR1 and noticed that it promoted mice to be unsusceptible to memory impairment, similarly irrelevant to sensitivity to thermal pain stimuli. These findings imply that S1PR1 in the DG may exclusively negatively regulate chronic pain-related memory impairment. Nevertheless, CNS S1PR1 activation has also been reported in conditions with cisplatin-induced cognitive impairment (54), and peripheral administration of either agonist or functional S1PR1 antagonist can ameliorate spatial memory impairment (40, 55). Herein, the mechanisms of action of S1PR1 signaling (agonism or antagonism) with regard to the memory performance remain controversial.

Further, our study pointed out that S1PR1 activation in the DG may not be involved in the processing of pain. To date, a growing body of evidence has shown that activation of S1P axis at spinal cord triggers the occurrence of peripheral sensitization of pain. Activation of S1PR1 in astrocytes in the spinal cord contributes to neuropathic pain (30), and mice with astrocyte-specific alterations of S1PR1 in the spinal cord did not experience neuropathic pain (56). Additionally, elevated S1P levels at spinal cord injury sites attract macrophages and microglia, and their activation worsens the inflammatory response (57). Moreover, an S1PR1 antagonist lessens neuropathic pain induced by spinal cord injury by inhibiting neuroinflammation and glial scar formation (58). In contrast with the evidence available in the spinal cord, the role of S1P signaling in higher pain centers is poorly understood (59). The present study provides evidence that in the hippocampal DG, S1P/S1PR1 signaling is irrelevant to pain perception.

Then how does S1PR1 regulate the structural plasticity in the DG and further affect memory formation in chronic neuropathic pain? Our study provides a notable insight by uncovering an integrin α2-dependent modification of the actin cytoskeleton through the activation of the Rac1/Cdc42 signaling cascade and Arp2/3-dependent actin polymerization. Actin cytoskeleton rearrangement is associated with synapse formation, spine architecture and function, thus affecting numerous processes such as memory formation (60-62). Rho GTPases (RhoA, Rac1 and Cdc42) are key regulators of cytoskeleton assembly and are masters in maintaining spine morphology and memory (63). For example, Rac1 induces branching of actin filaments in

lamellipodia by mediating actin polymerization via activating the Arp2/3 complex (64-66). Cdc42 is also an important signaling protein for reorganization of actin cytoskeleton and morphogenesis of cells. Loss of Cdc42 causes deficits in synaptic plasticity and remote memory recall (67). Given the evidence that S1P/S1PR1 modulates significant cytoskeletal rearrangements via actin regulatory proteins of Rho GTPases Rac1 and Cdc42, but not through RhoA which interacts with S1PR2 (28, 47, 50), we therefore examined the expression of Rac1 and Cdc42 at protein levels. Our findings revealed a significant downregulation of Rac1 and Cdc42 expression in susceptible mice and mice with S1PR1 knockdown in the DG, suggesting that S1PR1 functions upstream of Rac1 and Cdc42 in the DG. Consistent with this observation, we detected a downregulation of the actin polymerization modulator Arp2/3 complex. Actin remodeling involves the dynamic alterations in actin polymerization that contribute to the structural changes observed at neural synapses. Actin polymerization of the transition of G-actin into F-actin is crucial for orchestrating all the modifications necessary to facilitate synaptic communication by increasing spine volume. Conversely, the inability to form F-actin results in contrasting outcomes of decreased spine volume and diminished synaptic communication (68). To further elucidate the causal relationship between DG S1PR1 and actin remodeling, we quantitated F-actin and G-actin in the mouse DG, and generated a S1PR1 knockdown HT-22 cell line to visualize F-actin by phalloidin staining. Our findings in susceptible mice indicate a significant inhibition of the transition from G-actin to F-actin, suggesting the involvement of S1P/S1PR1 in DG actin polymerization. RNA-Seq data further revealed that integrin alpha 2 may participate in this regulatory process. Integrins are linkers of the extracellular matrix and intracellular actin cytoskeleton mediating cytoskeletal organization (69). The concomitant alteration in expression levels of Itga2 with S1PR1, and the physical and functional analysis between the two proteins of S1PR1 and ITGA2, indicate their collaboration in the regulation of cytoskeleton arrangement.

This study has potential limitations. First, the memory performance in the chronic pain model is exclusively evaluated based on spatial cues which mainly rely on the hippocampal functions. Further validation using various types of memory tests would strengthen the evidence for the categorization of mice into susceptible and unsusceptible subgroups. Additionally, the study would also benefit from a comprehensive exploration on the impact of different types of chronic pain on memory impairment. Different chronic pains including chronic nociceptive pain, chronic neuropathic pain, composite pain and chronic psychological pain, have different pathological

mechanisms and impacts on memories. It is worth noting that preclinical and clinical research has demonstrated that the influence of pain intensity on memory function in chronic pain patients remains controversial (70). Thus, future research needs to facilitate the investigation of differences between the various subtypes of chronic pains and comorbid memory impairment. Furthermore, the reliance on animal models may limit the generalizability of the findings to humans. Based on the current data, decreased serum S1P level could be a potential biomarker for evaluating the susceptibility of memory impairment. In future studies, it would be interesting to examine whether S1P levels in the serum of patients with pain is associated with memory impairment. Besides, except for S1PR1 and ITGA2 there are also other potential molecular targets implicated in this study, more work is needed to define their roles on the disease occurrence.

In summary, our study develops a paradigm for separating the susceptible and unsusceptible subgroups to chronic pain-induced memory impairment and delineates the key role of S1P/S1PR1 signaling in vulnerability to memory impairment. Since there are currently few pharmacological alternatives for the treatment of the comorbidity, these findings may serve as a foundation for the development of optimal preventive and therapeutic medications. Additionally, the strategy this study used to categorize memory impairment susceptibility may inspire new methods for stratifying patient populations in clinical settings.

Methods

Animals. Male C57BL/6J mice (8-10 weeks old) were housed 4-6 per cage with ad libitum access to food and water, at a constant temperature (22 to 25˚C) and humidity (40% to 60%). They were kept under a 12:12 light/dark cycle (lights on at 8:00 AM). All animal protocols were approved by the Animal Care and Use Committee of Xuzhou Medical University (202209S054, 202309T017).

Virus vectors, chemicals, and antibodies. Information for viral vectors, chemicals, and antibodies used in the present study was listed in Supplemental Tables 1-3.

Chronic neuropathic pain model. Chronic constrictive injury (CCI) of the sciatic nerve was used to establish chronic neuropathic pain, as described previously (71). Briefly, mice were

anesthetized by 1% pentobarbital sodium (40 mg/kg, *i.p.*) and the left sciatic nerve was exposed by separating the muscles at the mid-thigh level then loosely ligated with three non-absorbable 4-0 slik braided suture proximal to the trifurcation at a 1.0 to 1.5 mm interval. After suturing and sterilizing, animals were placed in a recovery cage on a heating pad. For the following behavioral tests, a control group and an experimental group is identical in all respects of handling and experimental conditions, except for one difference-nerve injury.

Paw withdrawal threshold (PWT). Mechanical allodynia was measured by PWT in a double-blinded manner by using the up and down method with von Frey filaments. Mice were placed on a wire mesh grid and allowed for 60-minute acclimation. A von Frey hair weighing 0.008 to 2.0 g was used. The filaments (from 0.16g filament) were perpendicularly applied to the plantar surface of the left hind paw through the wire mesh grid. Once a positive response is observed, change the filament to next lowest level. In the absence of a response, move to the next highest filament. Paw withdrawal, flinching, or paw licking was considered a positive response. 50% PWT was determined using the “up-down” method.

Paw withdrawal latency (PWL). Thermal hyperalgesia was evaluated by PWL in a double-blinded manner following Hargreaves *et al*. (72). Briefly, the mice were placed on a glass platform and allowed for 60-minute acclimation. Thermal stimulation was focused on the plantar surface of the left hind paw through the glass plate. The time taken to withdraw from the heat stimulus is recorded for 3 times at an interval of 5 minutes for rest. The average time was considered as the PWL. Thermal stimulation was no more than 20 seconds.

Behavioral test battery to assess learning and memory. We followed the golden rule that we start with the least stressful test (Y-maze) and leave the most stressful of all for last (Morris Water maze). Additionally, we also ensured that between tests the animals have enough resting time to decrease carryover effects from prior tests. A common order of behavioral tests associated with learning and memory are Y-maze forced alternation (Y maze in this study), novel object recognition, Morris water maze, radial arm water maze and Y-maze spontaneous alternation (73).

Y maze. Testing occurs in a Y-shaped apparatus consisting of 3 white, enclosed arms with an angle of 120 □ from each other, each arm measuring 30 cm in length, 6 cm in width, and 15 cm in height, named the arms of the maze A, B and C. The experiment was started after the mice had habituated for half an hour in the behavioral chamber, and within 10 min of training,

after the C-arm (novel arm) was occluded with a white plastic plate, mice were gently placed in the A-arm so that they were free to explore in both A and B arms. The mice were then returned to their home cage and allowed to move freely for 1 hour. During the test period (5 min), the C-arm (novel arm) was opened, and the time and distance of the mice's exploration in the three arms were traced by a video-tracking system. The percent time and distance of mice exploring in the C-arm (novel arm) were analyzed.

Morris water maze (MWM) test. MWM test was performed in a round tank (100 cm in diameter and 51 cm in depth) with a small platform (8.5 cm in diameter, submerged 0.5 cm below water surface). The water was dyed with nontoxic and edible titanium dioxide. A computerized video tracking system (ANY-maze, Stoelting Co., IL, USA) was located 200 cm above the center of the tank to record performance. The tank was divided into 4 equal quadrants, southwest (SW), northwest (NW), northeast (NE) and southeast (SE). The platform is placed in the center of SW quadrant. Different graphic cues were put up on the walls of the four orientations to help the mice to build up spatial memory. Mice were trained for 4 days and tested for 2 days. During acquisition training, four trials were conducted every day, starting from the NE quadrant. Animals were placed in the water with its head facing the wall of the tank. The time (s) when the animal touched the underwater platform was recorded. If the time exceeds 60s, guide the animal to the platform and keep them stay for 10 seconds. Hereafter, the animals were dried and placed into a care cage. The interval between the two training sessions is 15 ~ 20min. On the first test day, escape latency assay and probe trials were given. The animals were placed in the diagonal quadrant (NE) of the platform quadrant, and the time to reach the platform and the swimming path of the mice were recorded. On the second text day, the platform was removed, and the percent time of total 30s of each animal spent in the target quadrant and the number of platform-site crossovers were recorded as the index of spatial memory.

Transmission Electron Microscope. Mice were deeply anesthetized by 1% pentobarbital sodium (40 mg/kg, *i.p.*) and their brains were collected on the ice to extract dentate gyrus of hippocampus(1mm*1mm*0.5mm) within one minute. After primary fixation with 4% paraformaldehyde and 3% glutaric dialdehyde solution at 4°C overnight and post-fixation with 1% osmium tetroxide in 0.1 M sodium phosphate buffer at 37°C for 2 h, tissues were washed with ddH_2O 4 times for 10 minutes each time. Different concentrations of ethanol and acetone are used to dehydrate the tissues gradiently. Then they were embedded with paraffin at different

temperatures for 48h. Semithin sections at a 1μm thickness were prepared and stained with toluidine blue as survey sections and are viewed using a light microscope in order to locate and trim the regions of hippocampal granule cell layer. Subsequently, ultrathin sections at a 70nm were obtained and sequentially stained with uranyl acetate and lead citrate for TEM observation. 4-6 images for each animal were recorded at 6300x magnification, and a counting frame (5x5 μm^2) was placed on each image for counting the number of excitatory synapses and measuring PSD width and length.

Golgi staining. Golgi staining was performed using FD Rapid Golgi Stain (FD NeuroTechnologies). Mice were anesthetized by 1% pentobarbital sodium (40 mg/kg, *i.p.*). Dissected mouse brains were immersed in solutions A and B in brown bottles for 14 days. The bottles were rotated occasionally to ensure perfect immersion. 14 days later, brains were transferred to solution C for 48 hours at 4 ℃ in the dark. The brains were sliced using a vibratome (Leica) at a thickness of 100 μm and mounted on gelatin coated slides. After reimmersion in solution C for 2 minutes and subsequent air drying, the brain slices were washed twice for 4 minutes each with ddH_2O and stained with solution D and E for 10 minutes. Stained brain slices were washed again with ddH_2O twice for 4 minutes each and then gone through gradient dehydration with gradient alcohol (50%, 75%, 95% ,100% ethanol, each 4 minutes). Fully dehydrated brain slices were washed with xylene 3 times for 4 minutes each and then mounted by coverslips using neutral gum as mounting media. Slides were stored in room temperature in the dark. Images of dendritic spines were captured using open field fluorescence microscope and analyzed with ImageJ and Sholl (74).

Immunohistochemistry. Mice were deeply anesthetized by 1% pentobarbital sodium (40 mg/kg, *i.p.*) and sequentially perfused with phosphate-buffered saline (PBS) followed by 4% paraformaldehyde solution. The brains were removed, postfixed with 4% paraformaldehyde solution at 4°C overnight and dehydrated in 30% sucrose solution for 48-h. Brain slices were prepared coronally with freezing microtome (VT1000S, Leica Microsystems) at a 30-μm thickness and were incubated with the blocking buffer containing 1% BSA and 0.1% Triton X-100 in PBS for 2 hours at room temperature and then overnight at 4 □C with the primary antibodies. After the slices were washed with TBS 3 times for 10 minutes each time, they were incubated with secondary antibodies for 2 hours at room temperature and followed by washing with PBS and mounting. After staining, slices were visualized with the laser scanning confocal microscopy (LSM880; Zeiss).

Western blotting. Hippocampal dentate gyrus was rapidly stripped and sonicated (Bioruptor™ UCD-200) in RIPA buffer (P0013B, Beyotime Biotechnology) with 1% cocktail (B14001, Bimake) followed by centrifuge (12000rpm, 15 min). Two DGs from one animal were used for each sample. Proteins were then electrophoresed in a 10% SDS polyacrylamide gel (PG112, Shanghai EpiZyme Scientific) and transferred onto a PVDF membrane (IPVH00010, millipore). The membranes were rinsed in triple and blocked with 5% skim milk before incubation with primary antibodies (Supplemental Table 3) at 4°C for 12 hours. After washing with TBST, membranes were incubated with secondary antibodies (Supplemental Table 3) for 2 hrs at room temperature. The final visualization of the membranes was achieved by ECL Chemiluminescent (BLH01S100CN, Bioworld). We then used housekeeping protein normalization for normalizing Western blot data. GAPDH was used as the internal control. The stained blot is imaged, a rectangle is drawn around the target protein in each lane, and the signal intensity inside the rectangle is measured by using ImageJ. The signal intensity obtained can then be normalized by being divided by the signal intensity of the loading internal control (GAPDH) detected on the same blot. The average of the ratios from the control group is calculated, and all individual ratios are divided by this average to obtain a new set of values, which represent the normalized values.

RNA-seq. Sham, unsusceptible and susceptible mice were sacrificed and the DG was rapidly dissected under RNase-free conditions. Total RNA was extracted using Trizol reagent kit (Invitrogen, Carlsbad, CA, USA) according to the manufacturer's protocol. RNA quality was assessed on an Agilent 2100 Bioanalyzer (Agilent Technologies, Palo Alto, CA, USA) and checked using RNase free agarose gel electrophoresis. After total RNA was extracted, eukaryotic mRNA was enriched by Oligo(dT) beads. Then the enriched mRNA was fragmented into short fragments using fragmentation buffer and reversely transcribed into cDNA by using NEBNext Ultra RNA Library Prep Kit for Illumina (NEB #7530, New England Biolabs, Ipswich, MA, USA). The purified double-stranded cDNA fragments were end repaired, A base added, and ligated to Illumina sequencing adapters. The ligation reaction was purified with the AMPure XP Beads (1.0X), and polymerase chain reaction (PCR) amplified. The resulting cDNA library was sequenced using Illumina Novaseq6000 by Gene Denovo Biotechnology Co. (Guangzhou, China).

Stereotaxic surgeries. Mice were deeply anesthetized by 1% pentobarbital sodium (40 mg/kg, *i.p.*) and mounted on a stereotaxic apparatus (RWD). A midline incision was made on the scalp

after disinfection, The skull was leveled and drilled a small hole in the skull with a dental drill. Virus was bilaterally injected into the DG of hippocampus (-1.3 A/P, ±1.95 M/L, and -2.02 D/V) by a 5ul Hamilton syringe at a rate of 0.1 μl/min by a microinjection pump (Harvard Apparatus, Holliston, MA). For the infusion of S1PR1 agonist, guide cannula (internal diameter 0.34 mm, RWD) was unilaterally implanted into DG of hippocampus (-1.3 A/P, -1.95 M/L, and -2.02 D/V). After surgery, the mice were placed on a hot blanket for 1 hour and returned to the home cages.

Local infusion. To deliver S1PR1 agonist SEW2871(0.7μM in 200nL) to the hippocampal DG, 10μl syringe (Hamilton) connected to an internal stainless-steel syringe and infusion pump inserted into a guide cannula were used. SEW2871 was delivered into the right DG of hippocampus at a flow rate of 100 nl/min. For multiple infusions, mice were deeply anesthetized by 1% pentobarbital sodium (40 mg/kg, *i.p.*).

Cell culture, transfection and flow cytometry sorting. HT-22 (HT-22 mouse hippocampal neuronal cell line) cells were maintained in Dulbelcco's modified Eagle's medium supplemented with 10% (vol/vol) fetal bovine serum (Invitrogen) in 5% CO2 atmosphere at 37 °C. The cell culture was around 70% confluent before transfection in a 6-well plate. Cells were incubated with transfection solution containing viruses (AAV-U6-shRNA(scramble)-GFP and AAV-U6-shRNA(s1pr1)-GFP) and polyrene in serum-free medium at 37 °C for 8 hours. The media were changed to fresh growth medium with serum post transfection. The transfection efficiency was determined as the percentage of cells expressing GFP in the entire cell population. In order to harvest the stable s1pr1 knock-down virus transfected cell line, we conducted flow cytometry sorting. Briefly, we discarded the original medium of the adherent cultured AAV-U6-shRNA(scramble)-GFP- and AAV-U6-shRNA(s1pr1)-GFP-transfected HT-22 cells, washed with sterilized 1×PBS once, added EDTA-free trypsin to digest for 3 minutes, and terminated the digestion by an equal volume of serum-containing medium. Subsequently, the cell suspension was collected, centrifuged at 600 rpm for 4 min. The supernatant was discarded and resuspended with sterilized 1xPBS into flow tubes. GFP-positive cells (transfected cells) were sorted out by flow cytometry (Beckman CytoFLEX SRT, Beckman) for subsequent experimental processes.

In vivo co-immunoprecipitation assay. Dentate gyrus tissues were carefully dissected, lysed in RIPA buffer (P0013B, Beyotime Biotechnology) with 1× Protease inhibitor cocktail (B14001, Bimake), sonicated (Diagenode, UCD-200) and centrifuged at 12000 rpm for 15 min at 4°C. The supernatant was taken for the co-immunoprecipitation assay using BeaverBeads® Protein A Immunoprecipitation Kit (Beaver, 22202-20) following the manufacturer' s instructions. Briefly,

30 μl Protein A beads were mixed with 5μg/mL anti-S1PR1 antibody (Abcam, Ab259902) and incubated with gentle rotation at room temperature for 15 min. Beads were pelleted and washed twice. Then the beads and the supernatant were incubated with rotation at room temperature for 1 h. The bound proteins were eluted from the beads with 1× Protein Loading Buffer by boiling at 95°C for 5 min. Protein samples were then separated and immunoblotted with anti-ITGA2 antibody (Bioss, bsm-52613R) by Western Blot.

Split-ubiquitin membrane-based Yeast two-hybrid system. In this ubiquitin system, ubiquitin, a protein composed of 76 amino acid residues that can mediate the ubiquitination degradation of target proteins by proteasomes, is split into two domains, namely Cub at the C-terminus and NbuG at the N-terminus, which are fused and expressed with the bait protein "Bait" and the prey protein "Prey", respectively. Here, the coding region of s1pr1 was fused to the "bait" pBT3-STE vector (Clontech) cloning at Sfi IA (5′-GGCCATTACGGCC-3′) and Sfi IB (3′-GGCCGCCTCGGCC-5′) sites. Full-length of itga2 was inserted into the Sfi IA (5′-GGCCATTACGGCC-3′) and Sfi IB (3′-GGCCGCCTCGGCC-5′) sites of the "prey" pPR3-C vector (Clontech). At the same time, Cub is also fused with transcription factor LEXa-VP16. If Bait and Prey proteins could bind, Cub and NbuG would be brought together and a complete ubiquitin would be formed, which would be recognized by the proteasome and the fused transcription factor would be cut off and enter the cell nucleus to activate the expression of the reporter gene. Series of combinations of bait and prey constructs were cotransformed into the yeast strain NMY51 (Clontech), and different concentrations of bacterial liquid were growing onto SD/-Trp/-Leu plates for 3 d at 30°C, interactions between baits and preys were examined on the selective medium SD/-Leu/-Trp/-His/-Ade. The blue colonies were chosen as candidates for possible interaction. The pNubG-Fe65 and pTSU2-APP vectors were served as positive controls, while the pPR3-N and pTSU2-APP were served as a negative control. Detailed procedures were conducted following the manufacturer' s instructions (Clontech).

k-means algorithm. k-means algorithm is used to partition the dataset into pre-defined number of clusters. Each data point belongs to a single group based on the distance between their centroids. The centroid is either the mean or median of all the points within the cluster depending on the characteristics of the data. The main procedures for k-means algorithm are as follows: (1) determine the k, namely group numbers; (2) Randomly assign a centroid to each of the k clusters; (3) Calculate the distance of all data to each of the k centroids; (4) Assign data to the closest centroid; (5) Update the centroid by taking the mean of all the points in each cluster;

(6) Repeat steps (3)-(5) until convergence; (7) The algorithm outputs the final cluster centroids and the assignment of each data point to a cluster. For categorization the mice into susceptible and unsusceptible groups (2 groups), we analyzed results from Y-maze and MWM tests using the k-means clustering algorithm and determine the k as 2. After assigning each data point to its closest k-center, we drew a median between both the centroids as a cutoff value. One cluster, including mice displaying a ratio of time more than the cutoff value, was defined as the unsusceptible mouse cluster. The other cluster, including mice exhibiting a ratio of time less than the cutoff value, was defined as the susceptible mouse cluster.

Statistics. The mice were assigned randomly to either the control group or the experimental group for each experiment. Data are presented as mean ± s.e.m. The summarized data in the violin plots were presented as the median (indicated by the bold dash line) along with the 25th and 75th percentiles (indicated by the slim dash line). K-Means cluster analysis was used to partition a given data set into a set of k groups (In this study, k=2). Unpaired Student's t-test was used to compare the mean of two independent groups. One-way analysis of variance (ANOVA) with post hoc Tukey's multiple comparisons was used to examine the differences in the means of three or more groups. Two-way analysis of variance (ANOVA) with post hoc Tukey's multiple comparisons was employed to determine the mean of a quantitative variable changes according to the levels of two independent variables. Statistical significance is indicated by asterisks as * $p < 0.05$, ** $p < 0.01$ and *** $p < 0.001$. Statistical analyses were performed using GraphPad Prism 9.0. and SPSS V22. Notably, every experiment was carried out a minimum of three times to make sure the results were consistent throughout the manuscript.

Figure legends

Figure 1. Segregation of mice with chronic pain into susceptible and unsusceptible subpopulations to memory impairment. (A) Timeline of CCI surgery, pain threshold tests, Y-maze test and MWM training. **(B)** Representative travelling traces and statistical results of Y maze test showing distance and percent time in the novel arm (Red) in CCI-Acute mice (6d post CCI, n = 8-21). **(C)** Representative travelling traces and statistical results of MWM training showing escape latency and percent time in the quadrant in CCI-Acute mice (11d post CCI, n = 8-21). **(D)** Representative travelling traces and statistical results of Y maze test showing distance and percent time in the novel arm (Red) in CCI-Chronic mice (22d post CCI, n = 8-21). **(E)** Horizontal scatterplot depicting the distribution of ratio of time in novel arm for Sham,

susceptible (S), and unsusceptible (U) mice in Y maze test. Bar graph represents the ratio of S and U mice in CCI-Chronic mice (22d post CCI, n = 71-152). **(F)** Representative travelling traces and statistical results of MWM training showing escape latency and percent time in the quadrant in CCI-Chronic mice (27d post CCI, n = 8-21). **(G)** Horizontal scatterplot depicting the distribution of ratio of time in the quadrant for Sham, S, and U mice in MWM training. Bar graph represents the ratio of S and U mice in CCI-Chronic mice (27d post CCI, n = 71-152). **(H)** Time in novel arm versus percent time in quadrant, for 152 CCI-Chronic mice. Each dot corresponds to one mouse. Colors of dots correspond to the groups of U in Y maze test but S in MWM (Red), U in both Y maze and MWM (Grey), S in Y maze test but U in MWM (Blue), and S in both Y maze and MWM(Yellow), respectively. Bar graph represents the ratio of each group in CCI-Chronic mice (n=152). **(I)** PWLs before and after administration of meloxicam (10mg/kg, *i.p.*, n = 10-20). **(J)** Statistical results of MWM training showing escape latency and percent time in the quadrant in 27d CCI mice before meloxicam administration (10mg/kg, *i.p.*, n = 10-20). **(K)** Performance of CCI mice in Y maze test before and after meloxicam administration (10mg/kg, *i.p.*). Bar graph (right) represents the ratio of U and S on 22d, 36d and 43d after CCI (n = 10-20). Data were analyzed by unpaired t test or one-way analysis of variance (one-way ANOVA), followed by post hoc Tukey's multiple comparisons between multiple groups when appropriate. All data are presented as the mean ± s.e.m. ns, not significant; *$p < 0.05$; **$p < 0.01$; ***$p < 0.001$. CCI, chronic constrictive injury; d, day; MWM, Morris water maze; PWL, paw withdrawal latency; PWT, paw withdrawal threshold; U, unsusceptible; S, susceptible.

Figure 2. S1PR1 expression is decreased in the hippocampal DG of susceptible mice. (A) Volcano plot showing RNA-Seq data for DG from Sham versus susceptible mice. DEGs are designated in red (upregulation [up]) and blue (downregulation [down]) and defined as having an FDR of less than 0.05. **(B)** Bar plot showing significant enrichment of DEGs in various pathways related with metabolism for Sham versus susceptible mice. **(C)** Relative expression levels are shown for genes related with lipid metabolism upon susceptible as compared with Sham. **(D)** Trend pattern used for analysis of Sham versus U versus S. **(E)** Bubble diagram represents the top 10 enrichment of KEGG pathways. **(F-I)** Example Western bands **(F)** and densitometric comparison **(H)** of the average expression of S1PR1 in DG lysates from Sham and CCI-Acute mice (7d post CCI). Lane1-6 represent Sham, Lane 7-12 represent CCI-Acute (n = 6); Example Western bands **(G)** and densitometric comparison **(I)** of the average expression

of S1PR1 in DG lysates from Sham, U and S mice. Lane1-4 represent Sham, Lane 5-8 represent U, and Lane 9-12 represent S (n = 4). Data were analyzed by unpaired t test or one-way analysis of variance (one-way ANOVA), followed by post hoc Tukey's multiple comparisons between multiple groups when appropriate. All data are presented as the mean ± s.e.m. ns, not significant; ***p < 0.001. CCI, chronic constrictive injury; d, day; U, unsusceptible; S, susceptible.

Figure 3. S1PR1 knockdown in the DG induces memory impairment. (A) Timeline of intra-DG virus injection, CCI surgery, pain threshold tests, Y maze test and MWM training. **(B)** A confocal image showing virus expression in the DG (Scale bar, 100 μm). **(C)** Example Western bands showing efficient S1PR1 knockdown in the DG lysates from Sham-Scramble, Sham-sh*s1pr1*, CCI-Scramble, and CCI-sh*s1pr1*. Densitometric comparison of the average expression of S1PR1 (n = 6). **(D)** Pain threshold in Sham- and CCI-treated mice subjected to Scramble/sh*s1pr1* in the DG (n = 8-10). **(E)** Quantitative summary of Y-maze showing distances traveled and time spent in the novel arm in Sham- and CCI-treated mice subjected to Scramble/sh*s1pr1* in the DG (n = 10-16). **(F)** Quantitative summary of MWM training showing escape latency and time spent in the quadrant in Sham- and CCI-treated mice subjected to Scramble/sh*s1pr1* in the DG (n = 10-16). **(G)** Ratio of U and S in CCI-Scramble and CCI-sh*s1pr1* mice. Data were analyzed by one-way analysis of variance (one-way ANOVA), followed by post hoc Tukey's multiple comparisons between multiple groups. All data are presented as the mean ± s.e.m. ns, not significant; *p < 0.05; **p < 0.01; ***p < 0.001. CCI, chronic constrictive injury; MWM, Morris water maze; PWL, paw withdrawal latency; PWT, paw withdrawal threshold; U, unsusceptible; S, susceptible.

Figure 4. Overexpression of S1PR1 in the DG rescues chronic pain-induced memory impairment. (A) Timeline of intra-DG virus injection, CCI surgery, pain threshold tests, Y maze test and MWM training. **(B)** A confocal image showing virus expression in the DG (Scale bar, 100 μm). **(C)** Example Western bands showing efficient S1PR1 overexpression in the DG lysates from Sham-Scramble, Sham-mimic, CCI-Scramble, and CCI-mimic. Densitometric comparison of the average expression of S1PR1 (n = 6). **(D)** Pain threshold in Sham- and CCI-treated mice subjected to Scramble/mimic in the DG (n = 8-10). **(E)** Quantitative summary of Y-maze showing distances traveled and time spent in the novel arm in Sham- and CCI-treated

mice subjected to Scramble/mimic in the DG (n = 10-16). **(F)** Quantitative summary of MWM training showing escape latency and time spent in the quadrant in Sham- and CCI-treated mice subjected to Scramble/mimic in the DG (n = 10-16). **(G)** Ratio of U and S in CCI-Scramble and CCI-sh*s1pr1* mice. Data were analyzed by one-way analysis of variance (one-way ANOVA), followed by post hoc Tukey's multiple comparisons between multiple groups. All data are presented as the mean ± s.e.m. ns, not significant; *p < 0.05; **p < 0.01; ***p < 0.001. CCI, chronic constrictive injury; MWM, Morris water maze; PWL, paw withdrawal latency; PWT, paw withdrawal threshold; U, unsusceptible; S, susceptible.

Figure 5. Local infusion of SEW2871 in the DG prevented the presence of chronic pain-induced memory impairment. (A) Timeline of cannula implant, CCI surgery, pain threshold tests, Y maze test and MWM training. **(B)** Confocal image showing cannula implanted in the DG (Scale bar, 100 μm). **(C)** Example Western bands showing expression of S1PR1 in DG lysates from Sham-Vehicle, Sham-SEW2871, CCI-Vehicle, and CCI-SEW2871. Densitometric comparison of the average expression of S1PR1 (n = 6). **(D)** Pain threshold in Sham- and CCI-treated mice subjected to local infusion of vehicle/SEW2871 in the DG (n = 8-10). **(E)** Quantitative summary of Y-maze showing distances traveled and time spent in the novel arm in Sham- and CCI-treated mice subjected to local infusion of vehicle/SEW2871 in the DG (n = 10-16). **(F)** Quantitative summary of MWM training showing escape latency and time spent in the quadrant in Sham- and CCI-treated mice subjected to local infusion of vehicle/SEW2871 in the DG (n = 10-16). **(G)** Ratio of U and S in CCI-vehicle and CCI-SEW2871 mice. Data were analyzed by one-way analysis of variance (one-way ANOVA), followed by post hoc Tukey's multiple comparisons between multiple groups. All data are presented as the mean ± s.e.m. ns, not significant; *p < 0.05; **p < 0.01; ***p < 0.001. CCI, chronic constrictive injury; DG, dentate gyrus; U, unsusceptible; S, Susceptible.

Figure 6. Susceptible mice exhibit altered excitatory synaptic plasticity in the hippocampal dentate gyrus. (A) Representative TEM images of synapses in the DG in Sham and CCI-Chronic mice (27d post CCI). Blue indicates presynaptic site and yellow indicates postsynaptic sites of excitatory synapses, respectively. Synaptic densities are bracketed by arrows (Scale bar, 500 nm). **(B)** Mean number of excitatory synapses per μm^2 of DG in Sham, unsusceptible and susceptible mice (n = 18-24 from 4 mice/group). **(C)** Cumulative distribution

plots for the lengths and widths of postsynaptic density in the DG in Sham, unsusceptible and susceptible mice (n = 102-156 from 4 mice/group). **(D)** Representative Golgi-staining images of dendritic spine morphology from the DG in Sham, unsusceptible and susceptible mice (Scale bar, top:50 μm; bottom:10μm). **(E)** The number of intersections of all dendritic branches in Sham, unsusceptible and susceptible mice (n = 15-18 from 4 mice/group). **(F)** Violin plots indicate the total dendritic length. **(G)** Violin plots indicate the number of mushroom/stubby type dendritic spines (left), and the number of thin/filopodia type dendritic spines (right) in Sham, unsusceptible and susceptible mice (n = 15-18 from 4 mice/group). Data were analyzed by one-way analysis of variance (one-way ANOVA), followed by post hoc Tukey's multiple comparisons between multiple groups when appropriate. All data are presented as the mean ± s.e.m. ns, not significant; *p < 0.05; **p < 0.01; ***p < 0.001. CCI, chronic constrictive injury; TEM, transmission electron microscope.

Figure 7. Overexpression of S1PR1 or local infusion of SEW2871 in the DG maintained the synaptic structural plasticity. (A) Representative TEM images of synapses in the DG in Sham- and CCI-treated mice subjected to Scramble/mimic in the DG. Blue indicates presynaptic site and yellow indicates postsynaptic sites of excitatory synapses, respectively. Synaptic densities are bracketed by arrows (Scale bar, 500 nm). **(B)** Mean number of excitatory synapses per μm^2 of DG in Sham- and CCI-treated mice subjected to Scramble/mimic (n = 18-24 from 4 mice/group). **(C)** Cumulative distribution plots for the lengths and widths of postsynaptic density in the DG in Sham- and CCI-treated mice subjected to Scramble/mimic in the DG (n = 121-162 from 4 mice/group). **(D)** Representative Golgi-staining images of dendritic spine morphology from the DG in Sham- and CCI-treated mice subjected to Scramble/mimic in the DG (Scale bar, top: 50 μm; bottom:10 μm). **(E)** The number of intersections of all dendritic branches in Sham- and CCI-treated mice subjected to Scramble/mimic in the DG (n = 18-24 from 4 mice/group). **(F)** Violin plots indicate the total dendritic length (n = 18-24 from 4 mice/group). **(G)** The number of mushroom/stubby type dendritic spines (left), and the number of thin/filopodia type dendritic spines (right) in the DG of in Sham- and CCI-treated mice subjected to Scramble/mimic in the DG (n = 18-24 from 4 mice/group). **(H)** Representative TEM images of synapses in the DG in Sham- and CCI-treated mice subjected to local infusion of vehicle/SEW2871 in the DG. Blue indicates presynaptic site and yellow indicates postsynaptic sites of excitatory synapses, respectively. Synaptic densities are bracketed by arrows (Scale

bar, 500 nm). **(I)** Mean number of excitatory synapses per μm^2 of DG in Sham- and CCI-treated mice subjected to local infusion of vehicle/SEW2871 (n = 18-24 from 4 mice/group). **(J)** Cumulative distribution plots for the lengths and widths of postsynaptic density in the DG in Sham- and CCI-treated mice subjected to local infusion of vehicle/SEW2871 in the DG (n = 121-162 from 4 mice/group). **(K)** Representative Golgi-staining images of dendritic spine morphology from the DG in Sham- and CCI-treated mice subjected to local infusion of vehicle/SEW2871 in the DG (Scale bar, top: 50 µm; bottom:10 µm). **(L)** The number of intersections of all dendritic branches in Sham- and CCI-treated mice subjected to local infusion of vehicle/SEW2871 in the DG (n = 18-24 from 4 mice/group). **(M)** Violin plots indicate the total dendritic length (n = 18-24 from 4 mice/group). **(N)** The number of mushroom/stubby type dendritic spines (left), and the number of thin/filopodia type dendritic spines (right) in the DG of in Sham- and CCI-treated mice subjected to local infusion of vehicle/SEW2871 in the DG (n = 18-24 from 4 mice/group). Data were analyzed by one-way analysis of variance (one-way ANOVA), followed by post hoc Tukey's multiple comparisons between multiple groups. All data are presented as the mean ± s.e.m. ns, not significant; *$p < 0.05$; **$p < 0.01$; ***$p < 0.001$. CCI, chronic constrictive injury; DG, dentate gyrus; TEM, transmission electron microscope.

Figure 8. Susceptible mice, S1PR1-knockdown mice and S1PR1 overexpression mice exhibit altered CDC42/RAC1 activity, ARP2/3-dependent actin signaling and engage ITGA2 in the DGCs. (A) Bubble diagram showing significant enrichment of DEGs in top 20 KEGG pathways for Sham versus susceptible mice. **(B)** Bubble diagram represents the top 20 enrichment of KEGG pathways using analysis of Sham versus U versus S. **(C)** Example Western bands showing expression of RAC1, CDC42, ARP2, ARP3, and ITGA2 in DG lysates from Sham and CCI-Acute mice (7d post CCI). **(D)** Densitometric comparison of the average expression of RAC1, CDC42, ARP2, ARP3 and ITGA2 (n = 6). **(E)** Example Western bands showing expression of RAC1, CDC42, ARP2, ARP3, and ITGA2 in DG lysates from Sham, U and S mice. **(F)** Densitometric comparison of the average expression of RAC1, CDC42, ARP2, ARP3 and ITGA2 (n = 6). **(G)** Example Western bands showing expression of RAC1, CDC42, ARP2, ARP3, and ITGA2 in DG lysates from in Sham- and CCI-treated mice subjected to Scramble/sh*s1pr1* in the DG. **(H)** Densitometric comparison of the average expression of RAC1, CDC42, ARP2, ARP3 and ITGA2 (n = 6). **(I)** Example Western bands showing expression of RAC1, CDC42, ARP2, ARP3, and ITGA2 in DG lysates from in Sham- and CCI-treated mice

subjected to Scramble/*s1pr1*-mimic in the DG. **(J)** Densitometric comparison of the average expression of RAC1, CDC42, ARP2, ARP3 and ITGA2 (n = 6). Data were analyzed by unpaired t test or one-way analysis of variance (one-way ANOVA), followed by post hoc Tukey's multiple comparisons between multiple groups when appropriate. All data are presented as the mean ± s.e.m. ns, not significant; **p* < 0.05; ***p* < 0.01; ****p* < 0.001. CCI, chronic constrictive injury; DG, dentate gyrus; U, unsusceptible; S, Susceptible.

Figure 9. S1PR1 regulates actin polymerization by interaction with ITGA2. (A-B) Quantification of F/G-actin ratio in dentate gyrus of Sham, U and S mice by Western blot. **(C)** Phalloidin staining of F-actin showing the simple cytoskeleton of s1pr1-/- knockdown HT-22 cells and primary hippocampal neurons in comparison to highly organized actin fibers present within scramble HT-22 cells and primary hippocampal neurons (Scale bar, 50 μm). **(D)** Interaction between s1pr1 and itga2 in a yeast two-hybrid system. pNubG-Fe65 and pTSU2-APP were used as a pair of positive control. pPR3-N and pTSU2-APP were used as a negative control. DDO, SD/-Trp/-Leu; QDO, SD/-Trp/-Leu/-His/-Ade. **(E)** In vivo co-immunoprecipitation assay shows that S1PR1 interacts with ITGA2 in the dentate gyrus of mice. Total protein extracts were immunoprecipitated by the anti-S1PR1-specific antibody and analyzed by immunoblot probed with the anti-S1PR1 and anti- ITGA2 antibodies. Immunoglobulin G was used as the negative control. **(F)** Timeline of intra-DG virus injection, CCI surgery, pain threshold tests, Y maze test and MWM training. **(G)** A confocal image showing virus expression in the DG (Scale bar, 100 μm). **(H)** Example Western bands showing efficient ITGA2 knockdown in the DG lysates from Sham-Scramble, Sham-shitga2, CCI-Scramble, and CCI-shitga2. Densitometric comparison of the average expression of S1PR1 (n = 3). **(I)** Pain threshold in Sham- and CCI-treated mice subjected to Scramble/shitga2 in the DG (n = 10-20). **(J)** Quantitative summary of Y-maze showing distances traveled and time spent in the novel arm in Sham- and CCI-treated mice subjected to Scramble/shitga2 in the DG (n = 10-19). **(K)** Quantitative summary of MWM training showing escape latency and time spent in the quadrant in Sham- and CCI-treated mice subjected to Scramble/shitga2 in the DG (n = 9-20). **(L)** Timeline of intra-DG virus injection, Y maze test and MWM training. **(M)** A confocal image showing virus expression in the DG (Scale bar, 100 μm). **(N)** Quantitative summary of Y-maze showing distances traveled and time spent in the novel arm in WT mice subjected to Scramble/shs1pr1/shitga2/shs1pr1+shitga2 in the DG (n = 10). **(O)** Quantitative summary of

MWM training showing escape latency and time spent in the quadrant in WT mice subjected to Scramble/shs1pr1/shitga2/shs1pr1+shitga2 in the DG (n = 10). Data were analyzed by one-way analysis of variance (one-way ANOVA), followed by post hoc Tukey's multiple comparisons between multiple groups. All data are presented as the mean ± s.e.m. ns, not significant; *p < 0.05; **p < 0.01; ***p < 0.001; ****p < 0.0001. CCI, chronic constrictive injury; d, day; MWM, Morris water maze; PWL, paw withdrawal latency; PWT, paw withdrawal threshold; DG, dentate gyrus; U, unsusceptible; S, susceptible.

Figure 10. Schematic representation of S1P/S1PR1 mediated susceptibility to chronic pain related memory impairment. (A) Mice subjected to chronic pain can be separated into memory impairment susceptible and unsusceptible subpopulations 21 days post CCI. **(B)** Structural synaptic plasticity is mainly regulated by the actin cytoskeleton organization. In the DGCs of Sham/unsusceptible mice, S1P/S1PR1 signaling mediates actin dynamics via Itga2-dependent activation of the Rac1/Cdc42 signaling cascade and Arp2/3 dependent actin polymerization, whereas in susceptible mice dysregulation of S1P/S1PR1 signaling in the DGCs leads to defective actin cytoskeleton organization which alters the synaptic plasticity. CCI, chronic constrictive injury; DGCs, dentate granule cells.

Acknowledgments

The present study was supported by the National Key Research and Development Program of China Brain Science and Brain-like Intelligence Technology (2021ZD0203100), the National Natural Science Foundation of China (82130033, 82293641, 31970937, 82271255, 82101315 and 82204081), Natural Science Foundation of Jiangsu Province (BK20220665 and BK20210908), the Priority Academic Program Development of Jiangsu Higher Education Institutions (21KJB320001), China Postdoctoral Science Foundation (2022M722676 and 2022M722675), Xuzhou Medical University start-up grant for excellent scientist (D2020053 and D2020033), Xuzhou Medical University Science and Technology Innovation Team of Youth Scientist (TD202203), Fusion Innovation Foundation of Xuzhou Medical University (XYRHCX2021009).

References

1. E. L. Whitlock *et al.*, Association Between Persistent Pain and Memory Decline and Dementia in a Longitudinal Cohort of Elders. *JAMA Intern Med* **177**, 1146-1153 (2017).
2. C. E. Phelps, E. Navratilova, F. Porreca, Cognition in the Chronic Pain Experience: Preclinical Insights. *Trends Cogn Sci* **25**, 365-376 (2021).
3. W. Zhao, L. Zhao, X. Chang, X. Lu, Y. Tu, Elevated dementia risk, cognitive decline, and hippocampal atrophy in multisite chronic pain. *Proceedings of the National Academy of Sciences* **120**, e2215192120 (2023).
4. K. Wiech, Deconstructing the sensation of pain: The influence of cognitive processes on pain perception. *Science* **354**, 584-587 (2016).
5. O. Moriarty, B. E. McGuire, D. P. Finn, The effect of pain on cognitive function: a review of clinical and preclinical research. *Prog Neurobiol* **93**, 385-404 (2011).
6. K. E. Innes, U. Sambamoorthi, The Potential Contribution of Chronic Pain and Common Chronic Pain Conditions to Subsequent Cognitive Decline, New Onset Cognitive Impairment, and Incident Dementia: A Systematic Review and Conceptual Model for Future Research. *J Alzheimers Dis* **78**, 1177-1195 (2020).
7. M. Tajerian *et al.*, The hippocampal extracellular matrix regulates pain and memory after injury. *Mol Psychiatry* **23**, 2302-2313 (2018).
8. M. Tajerian *et al.*, Brain neuroplastic changes accompany anxiety and memory deficits in a model of complex regional pain syndrome. *Anesthesiology* **121**, 852-865 (2014).
9. S. H. Xia *et al.*, Chronic Pain Impairs Memory Formation via Disruption of Neurogenesis Mediated by Mesohippocampal Brain-Derived Neurotrophic Factor Signaling. *Biol Psychiatry* **88**, 597-610 (2020).
10. G. F. Zhang *et al.*, Histone deacetylase 3 in hippocampus contributes to memory impairment after chronic constriction injury of sciatic nerve in mice. *Pain* **162**, 382-395 (2021).
11. A. A. Mutso *et al.*, Abnormalities in hippocampal functioning with persistent pain. *J Neurosci* **32**, 5747-5756 (2012).
12. C.-L. Zhang, Y. Zou, W. He, F. H. Gage, R. M. Evans, A role for adult TLX-positive neural stem cells in learning and behaviour. *Nature* **451**, 1004-1007 (2008).
13. T. Hainmueller, M. Bartos, Dentate gyrus circuits for encoding, retrieval and discrimination of episodic memories. *Nat Rev Neurosci* **21**, 153-168 (2020).
14. P. E. Gilbert, R. P. Kesner, I. Lee, Dissociating hippocampal subregions: double dissociation between dentate gyrus and CA1. *Hippocampus* **11**, 626-636 (2001).
15. M. R. Hunsaker, J. S. Rosenberg, R. P. Kesner, The role of the dentate gyrus, CA3a,b, and CA3c for detecting spatial and environmental novelty. *Hippocampus* **18**, 1064-1073 (2008).
16. J. W. Lee, M. W. Jung, Separation or binding? Role of the dentate gyrus in hippocampal mnemonic processing. *Neurosci Biobehav Rev* **75**, 183-194 (2017).
17. A. Tyrtyshnaia, I. Manzhulo, Neuropathic Pain Causes Memory Deficits and Dendrite Tree Morphology Changes in Mouse Hippocampus. *J Pain Res* **13**, 345-354 (2020).
18. D. G. Amaral, H. E. Scharfman, P. Lavenex, The dentate gyrus: fundamental neuroanatomical organization (dentate gyrus for dummies). *Prog Brain Res* **163**, 3-22 (2007).
19. G. Kempermann, H. G. Kuhn, F. H. Gage, Genetic influence on neurogenesis in the dentate gyrus of adult mice. *Proc Natl Acad Sci U S A* **94**, 10409-10414 (1997).
20. J. Ninkovic, T. Mori, M. Götz, Distinct modes of neuron addition in adult mouse neurogenesis. *J Neurosci* **27**, 10906-10911 (2007).
21. S. Tronel *et al.*, Adult-born dentate neurons are recruited in both spatial memory encoding and retrieval. *Hippocampus* **25**, 1472-1479 (2015).

22. X. Liu *et al.*, Optogenetic stimulation of a hippocampal engram activates fear memory recall. *Nature* **484**, 381-385 (2012).
23. S. Ramirez *et al.*, Creating a false memory in the hippocampus. *Science* **341**, 387-391 (2013).
24. R. L. Redondo *et al.*, Bidirectional switch of the valence associated with a hippocampal contextual memory engram. *Nature* **513**, 426-430 (2014).
25. T. J. Ryan, D. S. Roy, M. Pignatelli, A. Arons, S. Tonegawa, Memory. Engram cells retain memory under retrograde amnesia. *Science* **348**, 1007-1013 (2015).
26. S. Spiegel, D. Foster, R. Kolesnick, Signal transduction through lipid second messengers. *Curr Opin Cell Biol* **8**, 159-167 (1996).
27. S. Spiegel, S. Milstien, Sphingosine-1-phosphate: an enigmatic signalling lipid. *Nat Rev Mol Cell Biol* **4**, 397-407 (2003).
28. M. Cui, V. Göbel, H. Zhang, Uncovering the 'sphinx' of sphingosine 1-phosphate signalling: from cellular events to organ morphogenesis. *Biol Rev Camb Philos Soc* **97**, 251-272 (2022).
29. M. Maceyka, K. B. Harikumar, S. Milstien, S. Spiegel, Sphingosine-1-phosphate signaling and its role in disease. *Trends Cell Biol* **22**, 50-60 (2012).
30. Z. Chen *et al.*, Sphingosine-1-phosphate receptor 1 activation in astrocytes contributes to neuropathic pain. *Proceedings of the National Academy of Sciences* **116**, 10557-10562 (2019).
31. C. H. Yang *et al.*, Circuit Integration Initiation of New Hippocampal Neurons in the Adult Brain. *Cell Rep* **30**, 959-968.e953 (2020).
32. Y. Ye *et al.*, Activation of Sphingosine 1-Phosphate Receptor 1 Enhances Hippocampus Neurogenesis in a Rat Model of Traumatic Brain Injury: An Involvement of MEK/Erk Signaling Pathway. *Neural Plast* **2016**, 8072156 (2016).
33. T. Kanno *et al.*, Regulation of synaptic strength by sphingosine 1-phosphate in the hippocampus. *Neuroscience* **171**, 973-980 (2010).
34. L. Riganti *et al.*, Sphingosine-1-Phosphate (S1P) Impacts Presynaptic Functions by Regulating Synapsin I Localization in the Presynaptic Compartment. *J Neurosci* **36**, 4624-4634 (2016).
35. D. N. Mitroi *et al.*, Sphingosine 1-phosphate lyase ablation disrupts presynaptic architecture and function via an ubiquitin- proteasome mediated mechanism. *Sci Rep* **6**, 37064 (2016).
36. D. J. Gaertner, T. M. Hallman, F. C. Hankenson, M. A. Batchelder, "Chapter 10 - Anesthesia and Analgesia for Laboratory Rodents" in Anesthesia and Analgesia in Laboratory Animals (Second Edition), R. E. Fish, M. J. Brown, P. J. Danneman, A. Z. Karas, Eds. (Academic Press, San Diego, 2008), https://doi.org/10.1016/B978-012373898-1.50014-0, pp. 239-297.
37. T. Hornemann *et al.*, The SPTLC3 subunit of serine palmitoyltransferase generates short chain sphingoid bases. *J Biol Chem* **284**, 26322-26330 (2009).
38. H. Zhang *et al.*, Apicobasal domain identities of expanding tubular membranes depend on glycosphingolipid biosynthesis. *Nat Cell Biol* **13**, 1189-1201 (2011).
39. I. Gorshkova *et al.*, Inhibition of serine palmitoyltransferase delays the onset of radiation-induced pulmonary fibrosis through the negative regulation of sphingosine kinase-1 expression. *J Lipid Res* **53**, 1553-1568 (2012).
40. M. Asle-Rousta, S. Oryan, A. Ahmadiani, M. Rahnema, Activation of sphingosine 1-phosphate receptor-1 by SEW2871 improves cognitive function in Alzheimer's disease model rats. *Excli j* **12**, 449-461 (2013).

41. S. W. Park *et al.*, Sphinganine-1-phosphate protects kidney and liver after hepatic ischemia and reperfusion in mice through S1P1 receptor activation. *Lab Invest* **90**, 1209-1224 (2010).
42. C. L. Zhang, Y. Zou, W. He, F. H. Gage, R. M. Evans, A role for adult TLX-positive neural stem cells in learning and behaviour. *Nature* **451**, 1004-1007 (2008).
43. B. Leuner, E. Gould, Structural plasticity and hippocampal function. *Annu Rev Psychol* **61**, 111-140, c111-113 (2010).
44. L. Luo, Actin cytoskeleton regulation in neuronal morphogenesis and structural plasticity. *Annu Rev Cell Dev Biol* **18**, 601-635 (2002).
45. P. Hotulainen, C. C. Hoogenraad, Actin in dendritic spines: connecting dynamics to function. *J Cell Biol* **189**, 619-629 (2010).
46. B. W. Bernstein, M. T. Maloney, J. R. Bamburg, Actin and Diseases of the Nervous System. *Adv Neurobiol* **5**, 201-234 (2011).
47. C. Donati, P. Bruni, Sphingosine 1-phosphate regulates cytoskeleton dynamics: Implications in its biological response. *Biochimica et Biophysica Acta (BBA) - Biomembranes* **1758**, 2037-2048 (2006).
48. J. A. Green, J. G. Cyster, S1PR2 links germinal center confinement and growth regulation. *Immunol Rev* **247**, 36-51 (2012).
49. V. Adorno-Cruz, H. Liu, Regulation and functions of integrin α2 in cell adhesion and disease. *Genes Dis* **6**, 16-24 (2019).
50. N. R. Reinhard *et al.*, The balance between Gα(i)-Cdc42/Rac and Gα(1)(2)/(1)(3)-RhoA pathways determines endothelial barrier regulation by sphingosine-1-phosphate. *Mol Biol Cell* **28**, 3371-3382 (2017).
51. Y. Ephstein *et al.*, Critical role of S1PR1 and integrin β4 in HGF/c-Met-mediated increases in vascular integrity. *J Biol Chem* **288**, 2191-2200 (2013).
52. G. M. Cooper, *The Cell: A Molecular Approach. 2nd edition* (Sinauer Associates 2000, 2000).
53. A. Tyrtyshnaia, I. Manzhulo, Neuropathic Pain Causes Memory Deficits and Dendrite Tree Morphology Changes in Mouse Hippocampus. *Journal of Pain Research* **13**, 345-354 (2020).
54. S. Squillace *et al.*, Sphingosine-1-phosphate receptor 1 activation in the central nervous system drives cisplatin-induced cognitive impairment. *J Clin Invest* **132** (2022).
55. M. Zhang, Y. Hu, J. Zhang, J. Zhang, FTY720 Prevents Spatial Memory Impairment in a Rat Model of Chronic Cerebral Hypoperfusion via a SIRT3-Independent Pathway. *Front Aging Neurosci* **12**, 593364 (2020).
56. K. Stockstill *et al.*, Dysregulation of sphingolipid metabolism contributes to bortezomib-induced neuropathic pain. *Journal of Experimental Medicine* **215**, 1301-1313 (2018).
57. A. Kimura *et al.*, Essential roles of sphingosine 1-phosphate/S1P1 receptor axis in the migration of neural stem cells toward a site of spinal cord injury. *Stem Cells* **25**, 115-124 (2007).
58. K. Yamazaki *et al.*, FTY720 Attenuates Neuropathic Pain after Spinal Cord Injury by Decreasing Systemic and Local Inflammation in a Rat Spinal Cord Compression Model. *J Neurotrauma* **37**, 1720-1728 (2020).
59. S. Squillace, S. Spiegel, D. Salvemini, Targeting the Sphingosine-1-Phosphate Axis for Developing Non-narcotic Pain Therapeutics. *Trends Pharmacol Sci* **41**, 851-867 (2020).
60. F. Korobova, T. Svitkina, Molecular architecture of synaptic actin cytoskeleton in hippocampal neurons reveals a mechanism of dendritic spine morphogenesis. *Mol Biol Cell* **21**, 165-176 (2010).

61. R. Lamprecht, J. LeDoux, Structural plasticity and memory. *Nat Rev Neurosci* **5**, 45-54 (2004).
62. C. H. Bailey, E. R. Kandel, K. M. Harris, Structural Components of Synaptic Plasticity and Memory Consolidation. *Cold Spring Harb Perspect Biol* **7**, a021758 (2015).
63. S. Basu, R. Lamprecht, The Role of Actin Cytoskeleton in Dendritic Spines in the Maintenance of Long-Term Memory. *Frontiers in Molecular Neuroscience* **11** (2018).
64. L. Blanchoin *et al.*, Direct observation of dendritic actin filament networks nucleated by Arp2/3 complex and WASP/Scar proteins. *Nature* **404**, 1007-1011 (2000).
65. E. D. Goley, M. D. Welch, The ARP2/3 complex: an actin nucleator comes of age. *Nat Rev Mol Cell Biol* **7**, 713-726 (2006).
66. J. Xu, N. Galvanetto, J. Nie, Y. Yang, V. Torre, Rac1 Promotes Cell Motility by Controlling Cell Mechanics in Human Glioblastoma. *Cancers (Basel)* **12** (2020).
67. I. H. Kim, H. Wang, S. H. Soderling, R. Yasuda, Loss of Cdc42 leads to defects in synaptic plasticity and remote memory recall. *Elife* **3** (2014).
68. C. Dillon, Y. Goda, THE ACTIN CYTOSKELETON: Integrating Form and Function at the Synapse. *Annual Review of Neuroscience* **28**, 25-55 (2005).
69. C. K. Miranti, J. S. Brugge, Sensing the environment: a historical perspective on integrin signal transduction. *Nat Cell Biol* **4**, E83-90 (2002).
70. X. Liu, L. Li, F. Tang, S. Wu, Y. Hu, Memory impairment in chronic pain patients and the related neuropsychological mechanisms: a review. *Acta Neuropsychiatrica* **26**, 195-201 (2014).
71. G. J. Bennett, Y. K. Xie, A peripheral mononeuropathy in rat that produces disorders of pain sensation like those seen in man. *Pain* **33**, 87-107 (1988).
72. K. Hargreaves, R. Dubner, F. Brown, C. Flores, J. Joris, A new and sensitive method for measuring thermal nociception in cutaneous hyperalgesia. *Pain* **32**, 77-88 (1988).
73. A. Wolf, B. Bauer, E. L. Abner, T. Ashkenazy-Frolinger, A. M. Hartz, A Comprehensive Behavioral Test Battery to Assess Learning and Memory in 129S6/Tg2576 Mice. *PLoS One* **11**, e0147733 (2016).
74. M. Zhang *et al.*, Neuronal Histone Methyltransferase EZH2 Regulates Neuronal Morphogenesis, Synaptic Plasticity, and Cognitive Behavior in Mice. *Neurosci Bull* **39**, 1512-1532 (2023).

A

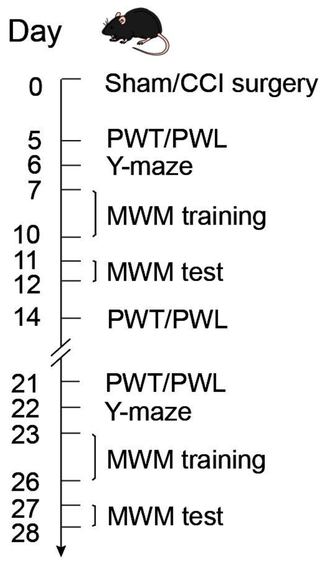

B

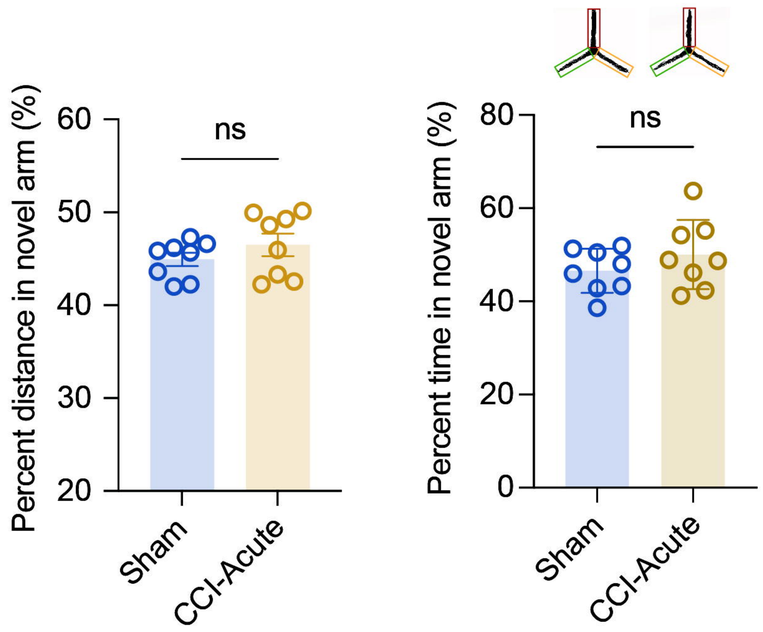

C

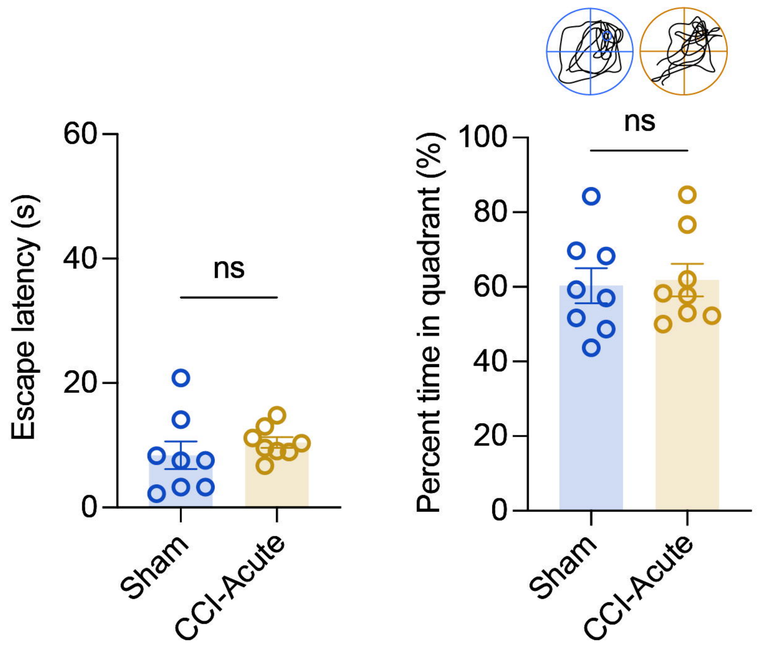

D

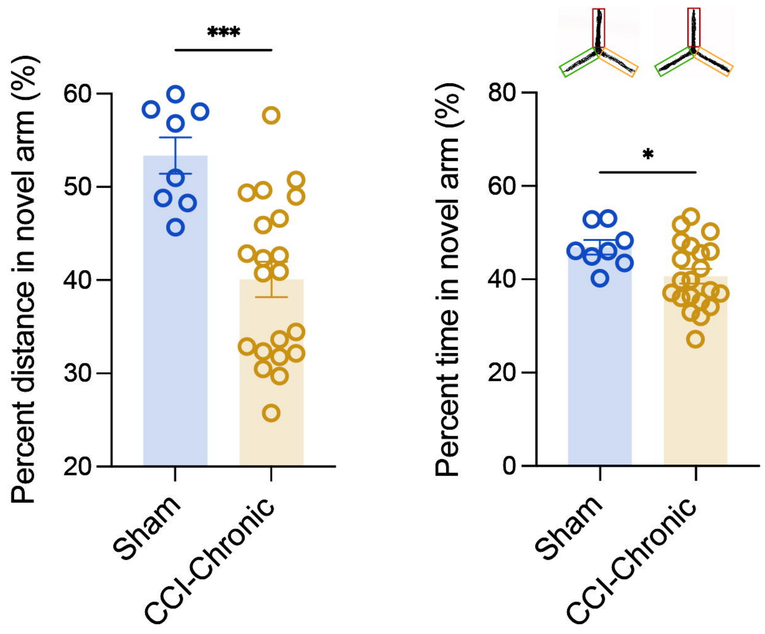

E

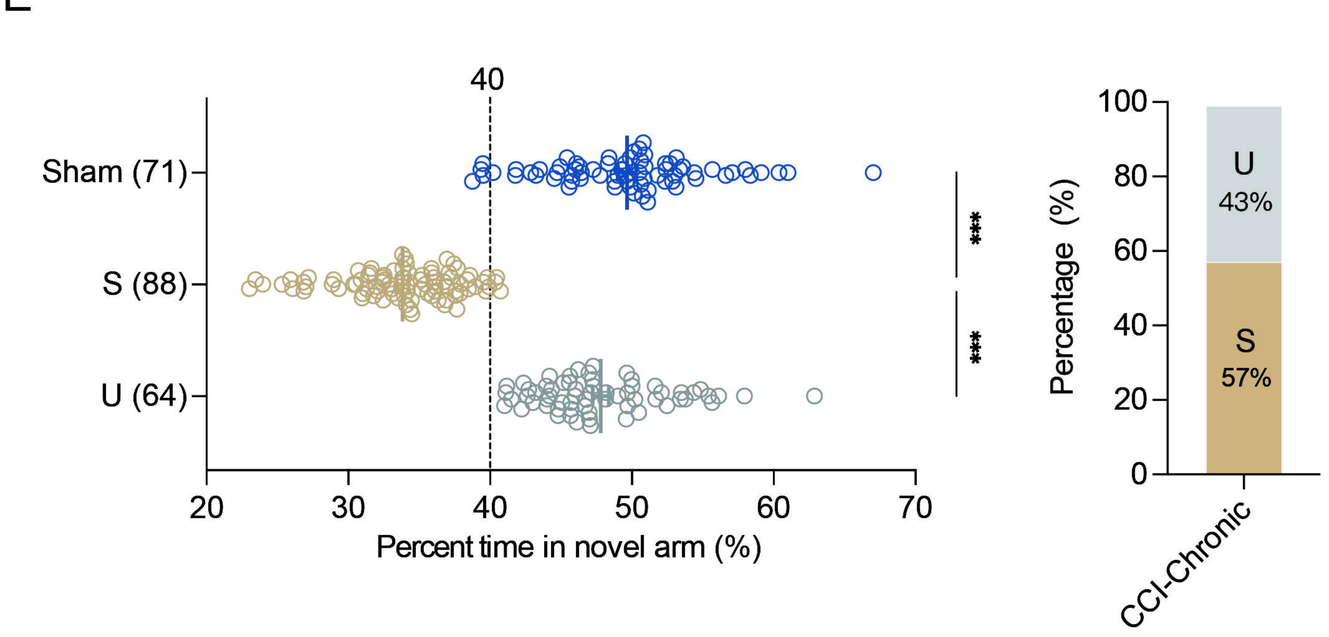

F

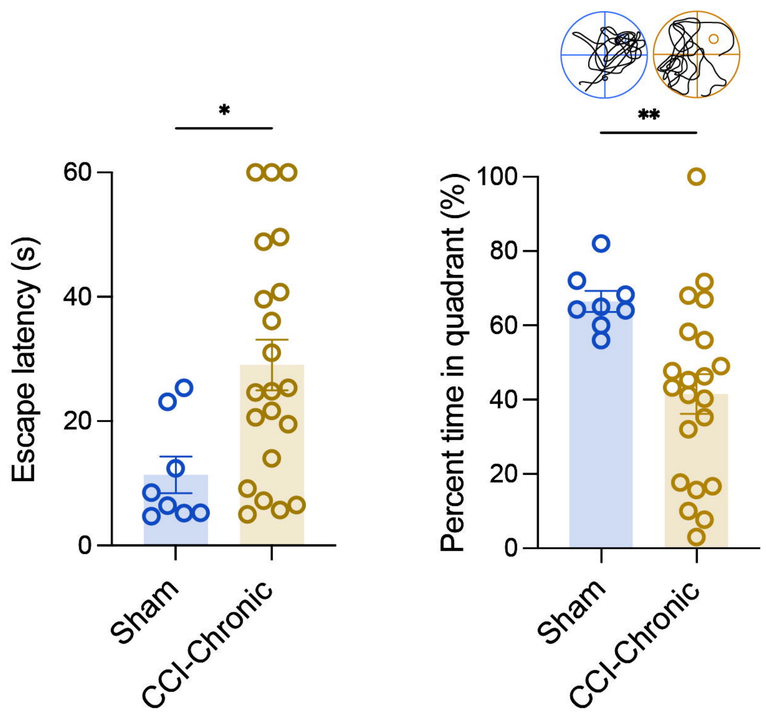

G

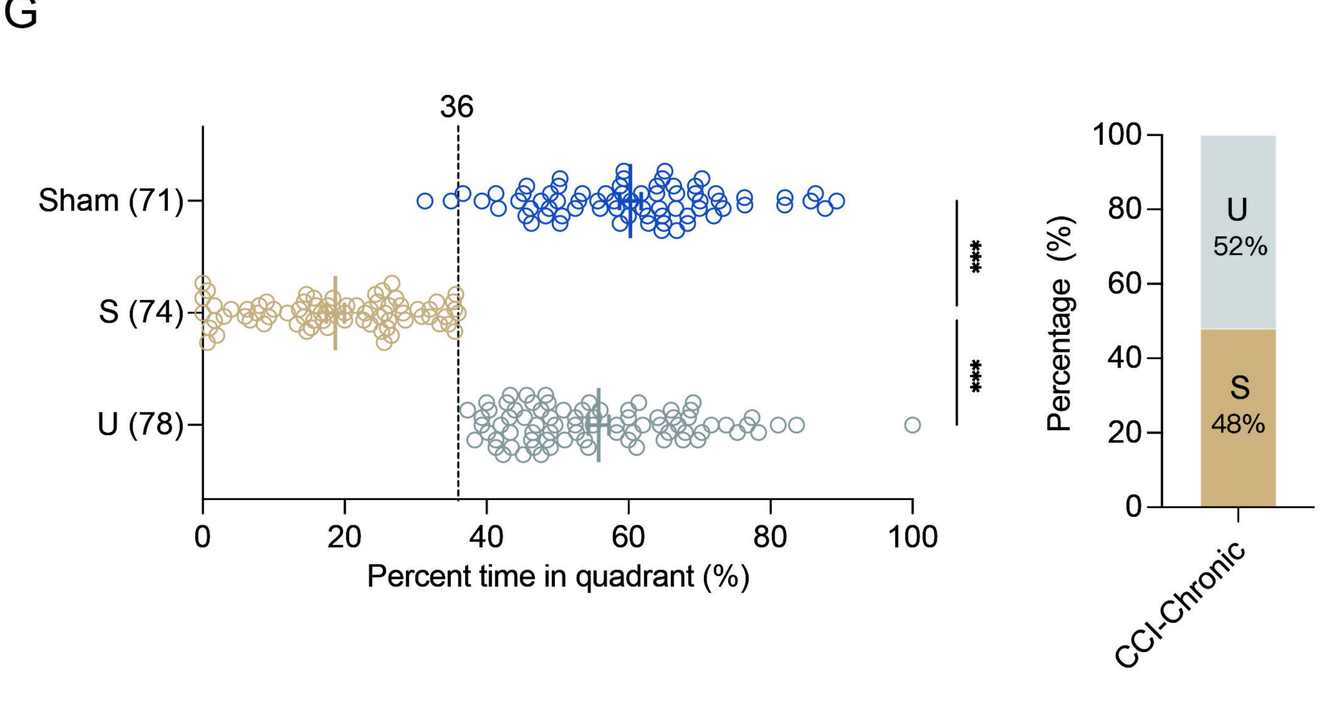

H

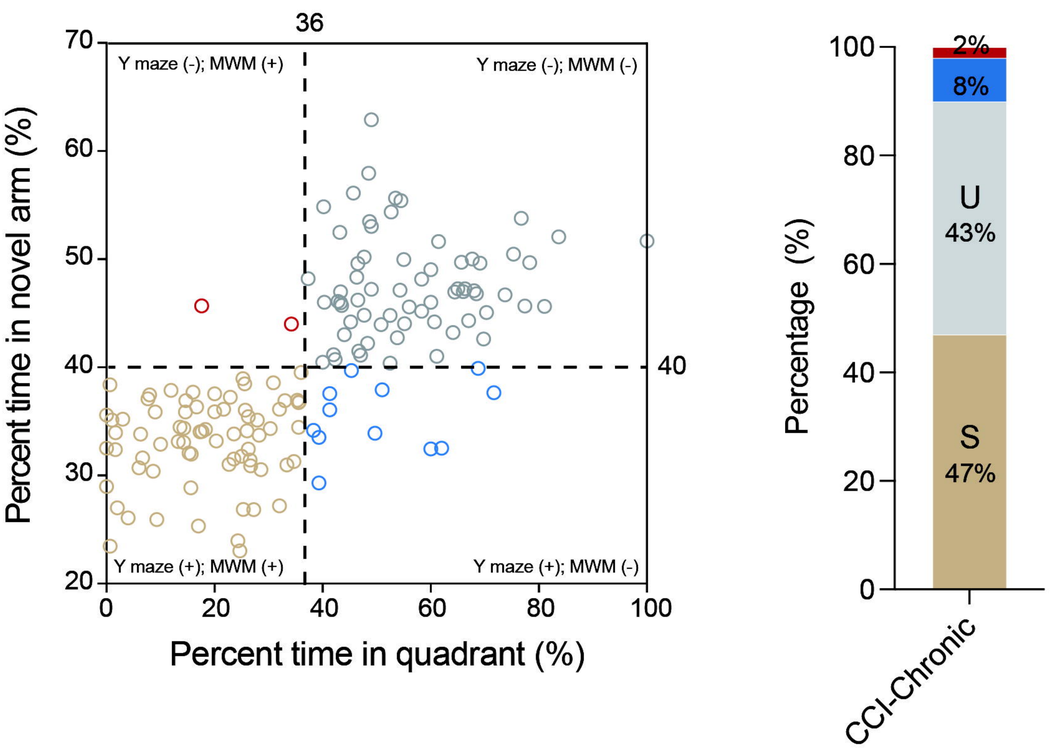

I

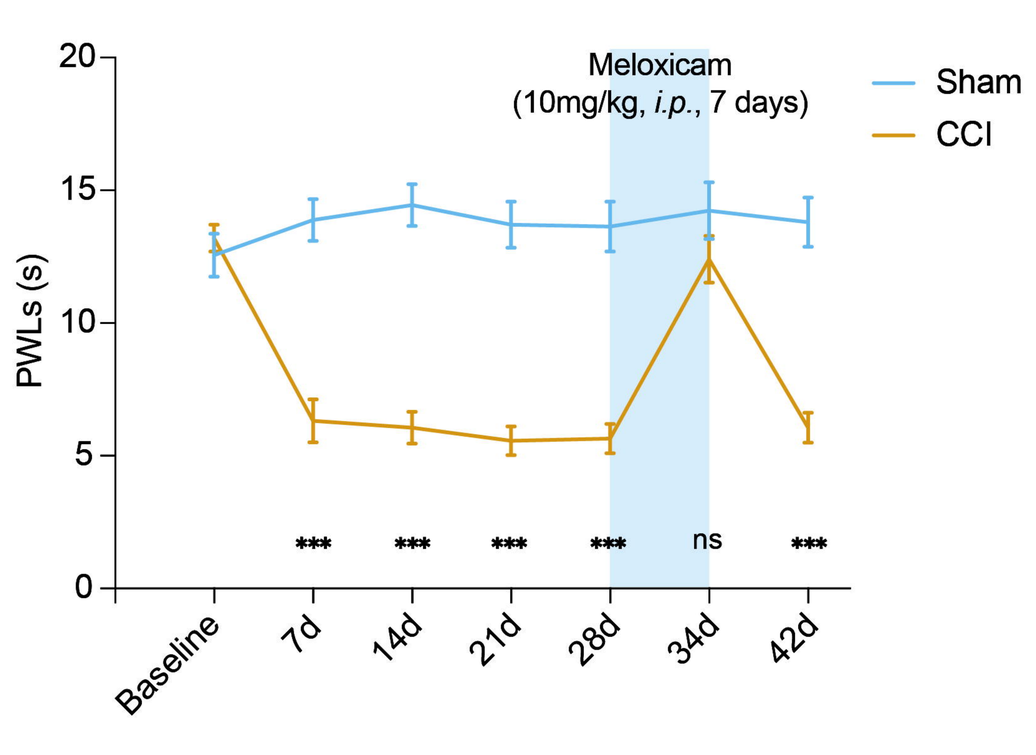

J

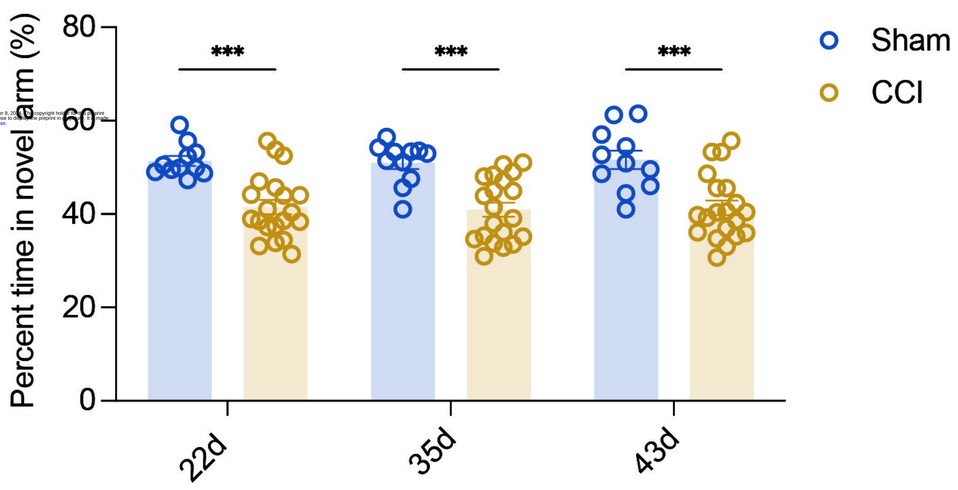

K

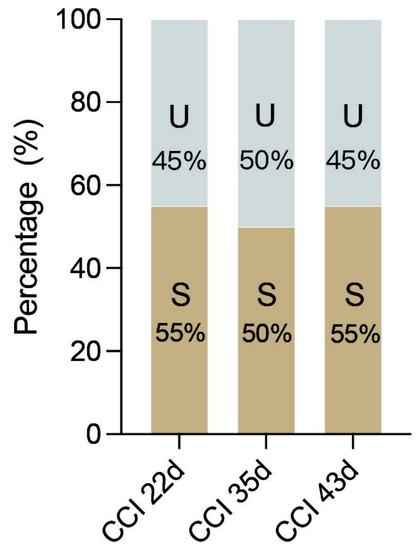

A

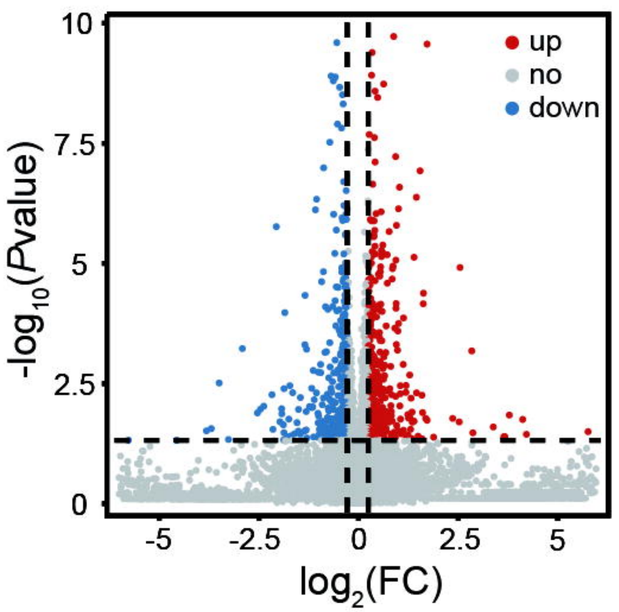

B

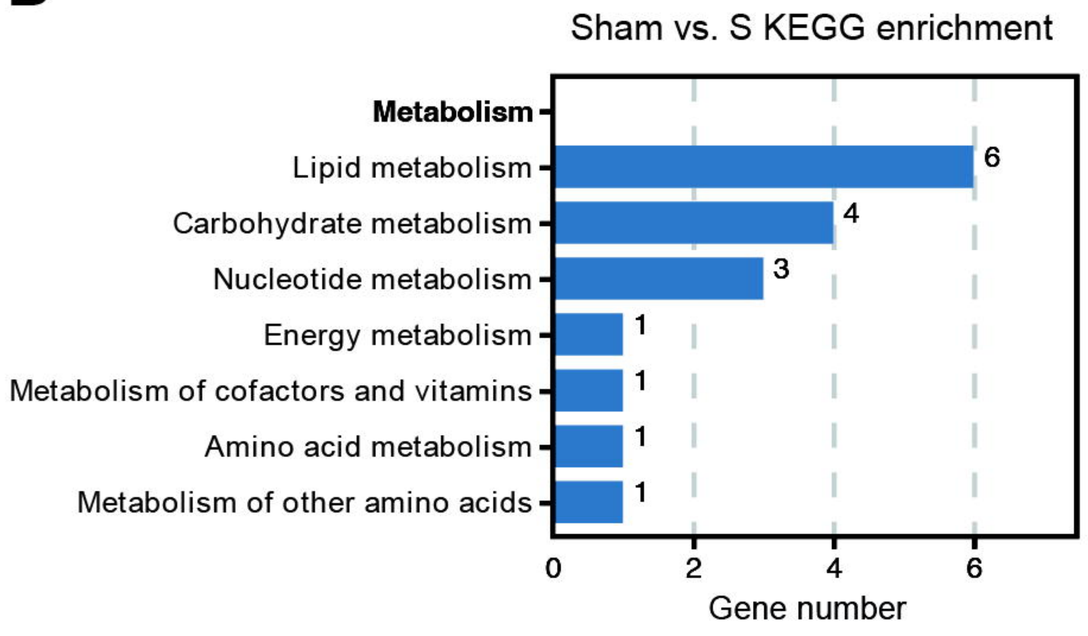

C

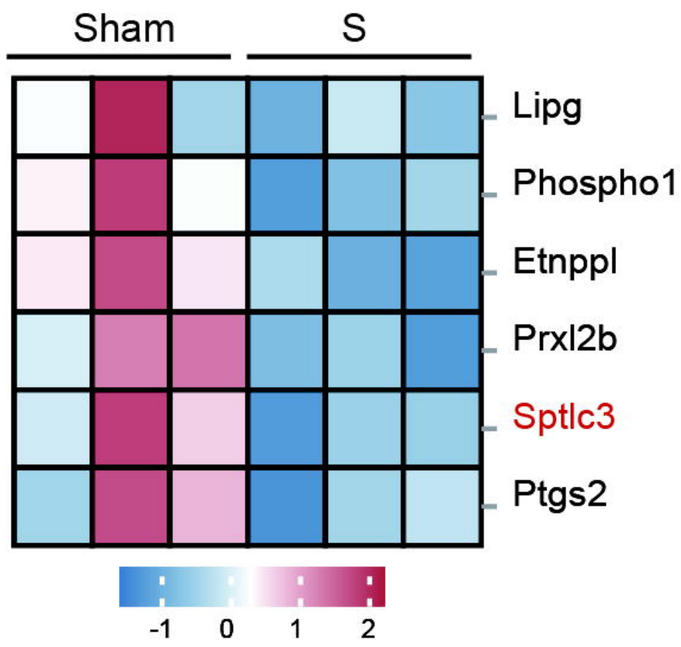

D

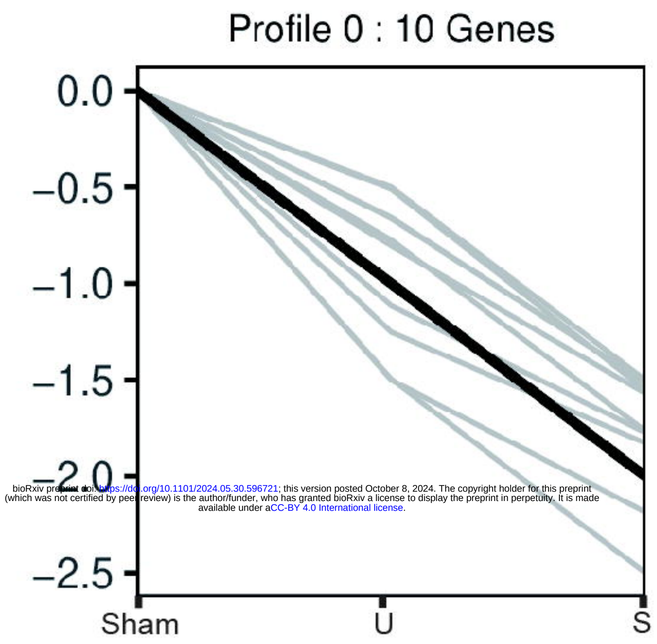

E

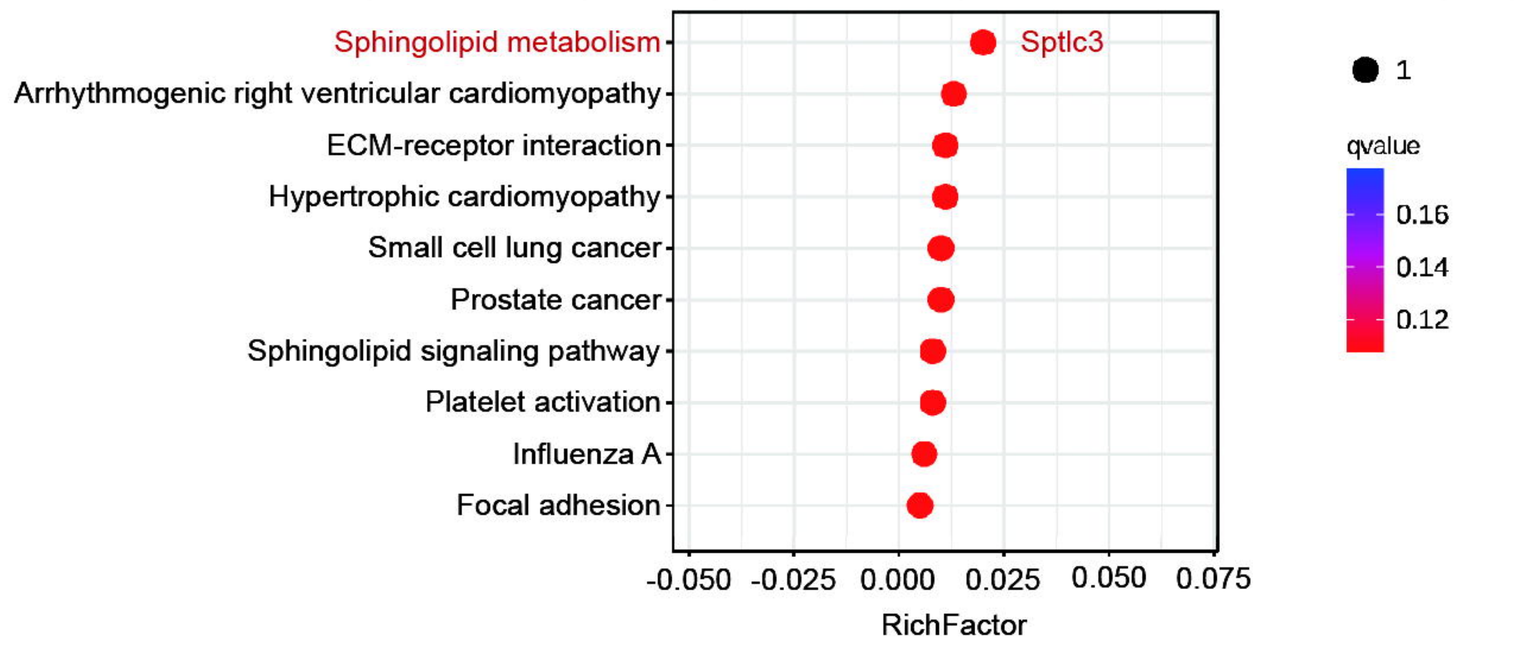

F

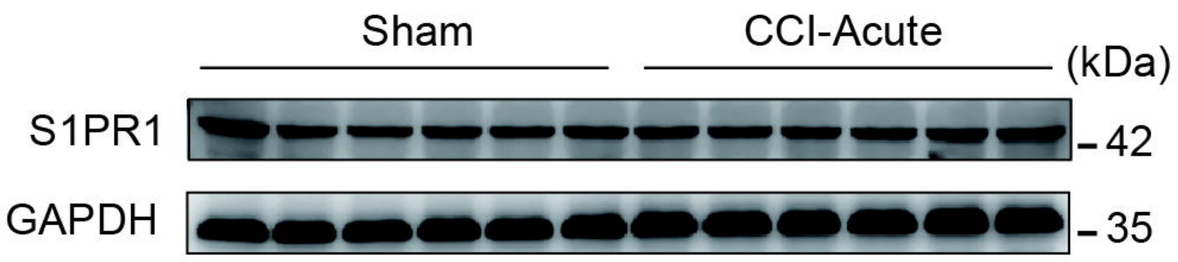

G

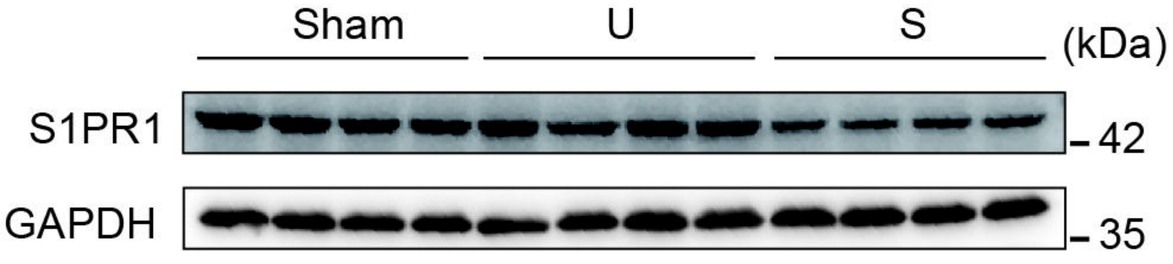

H

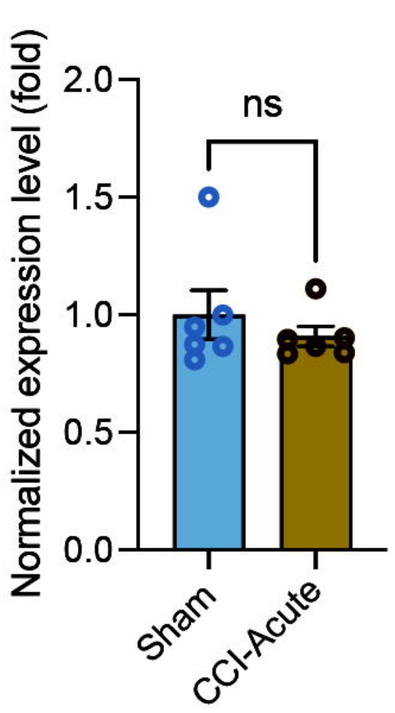

I

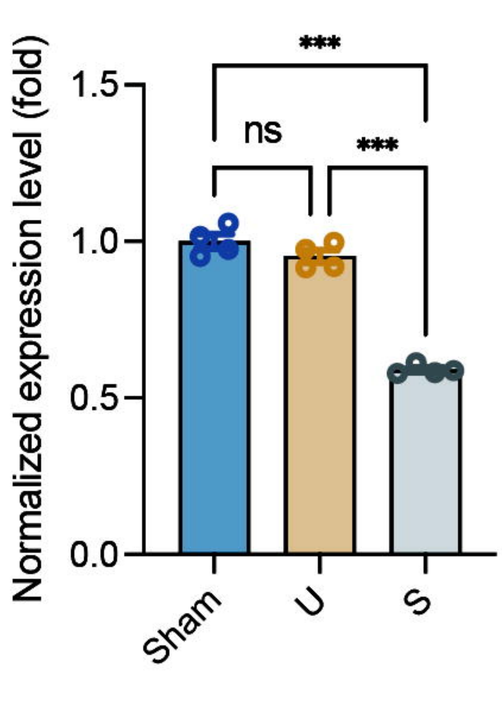

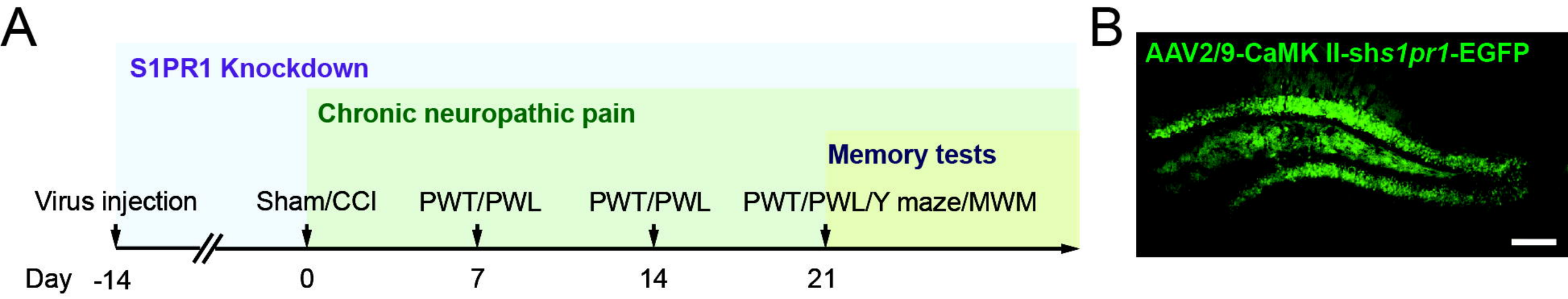

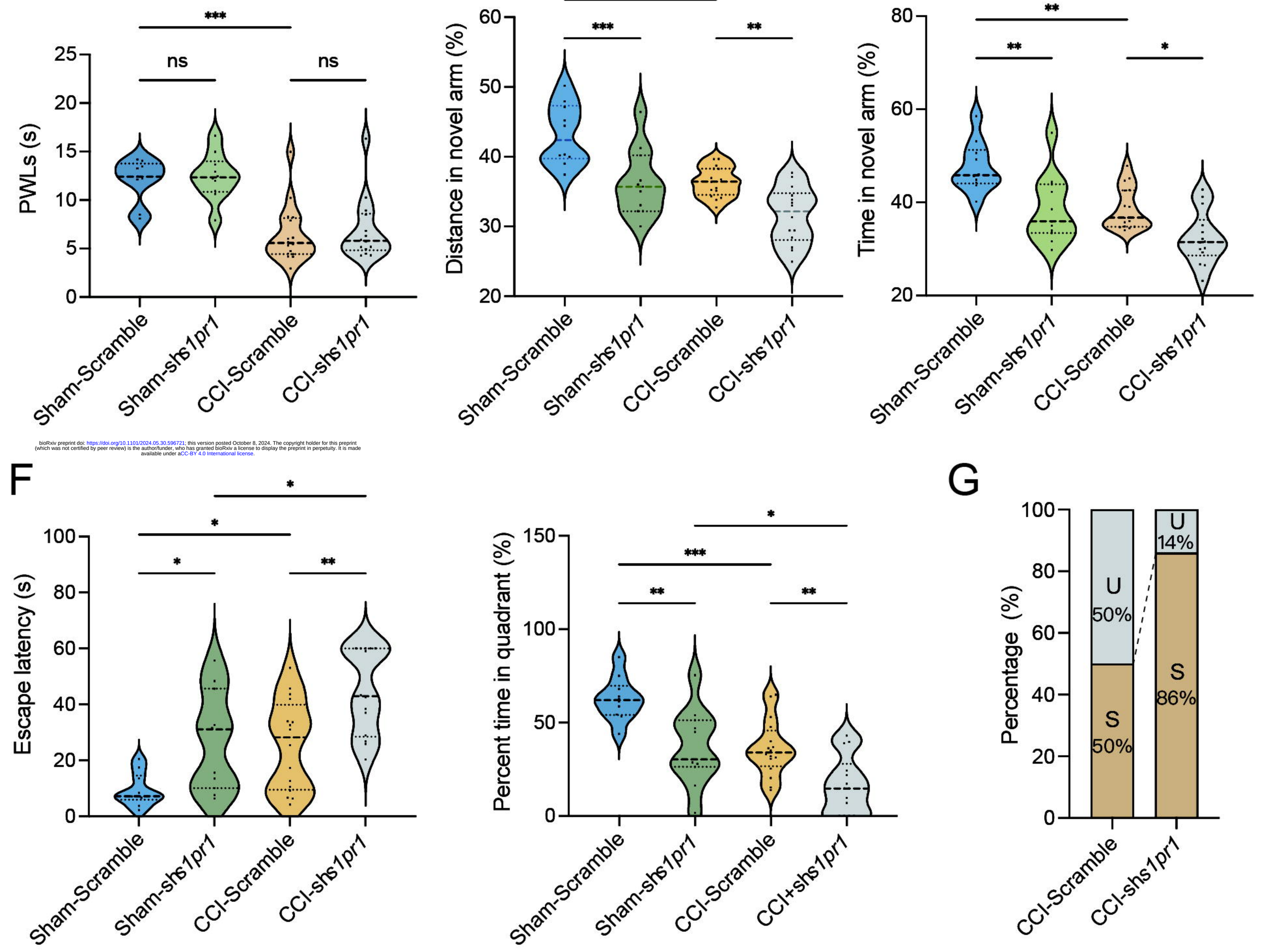

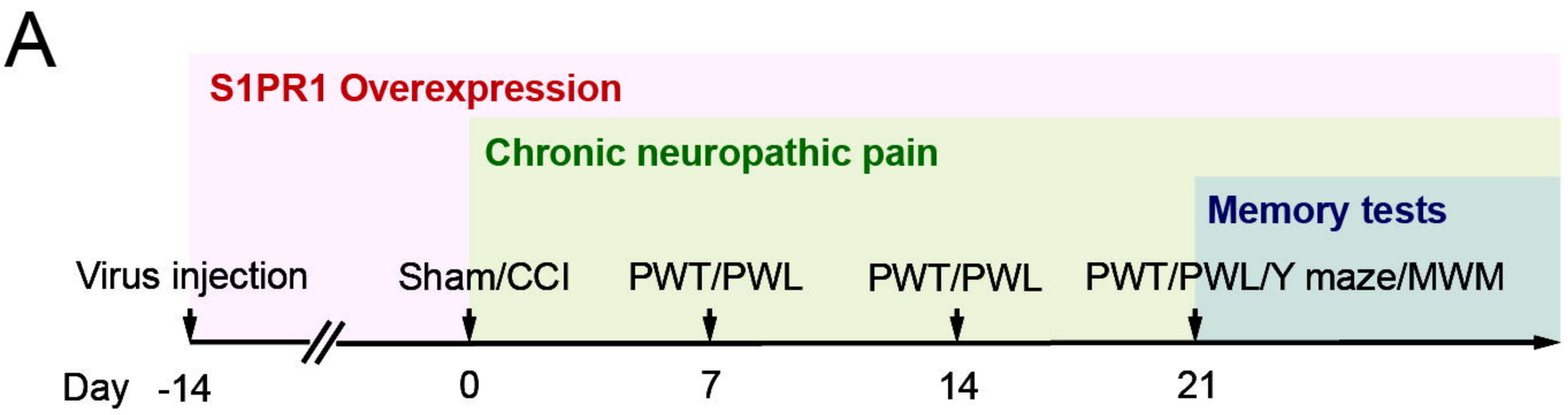

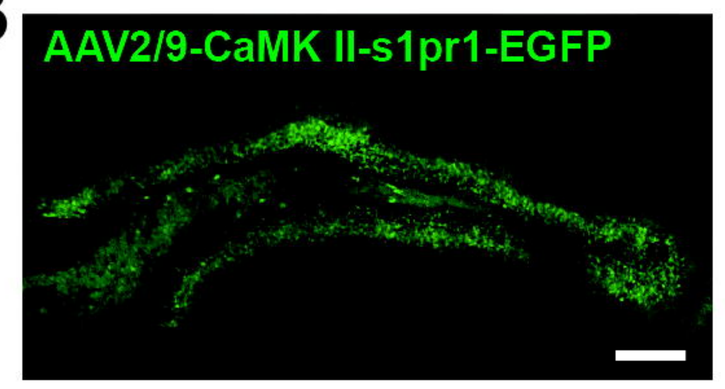

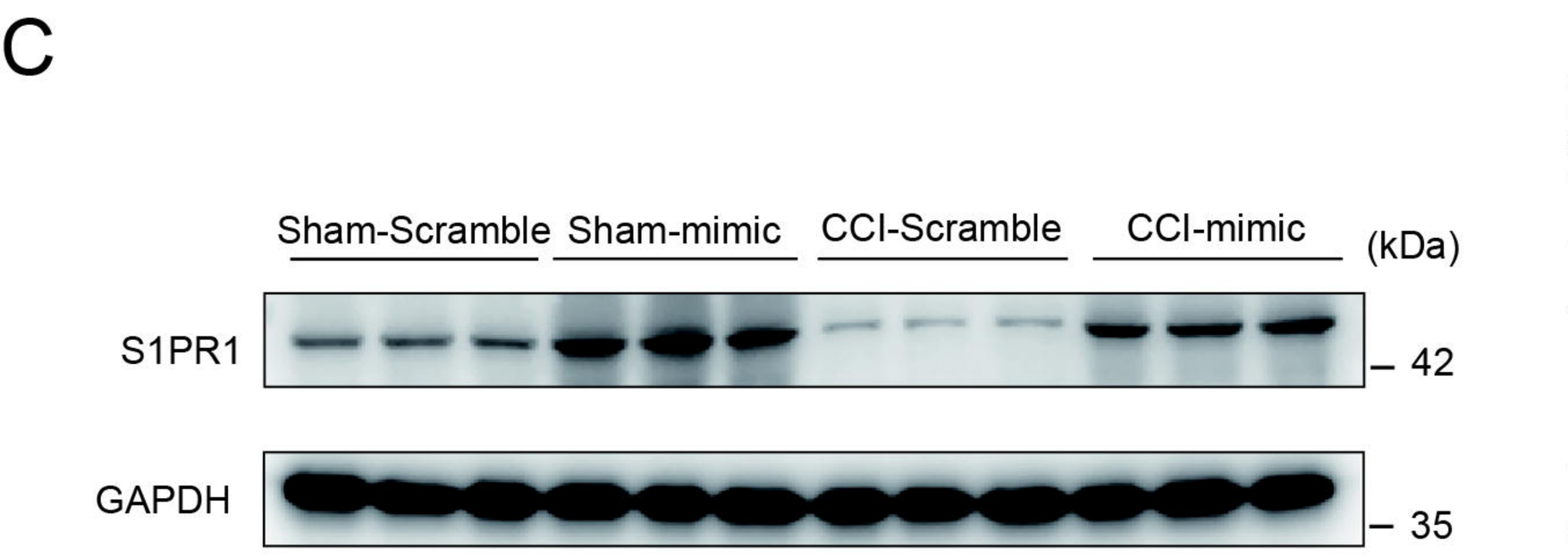

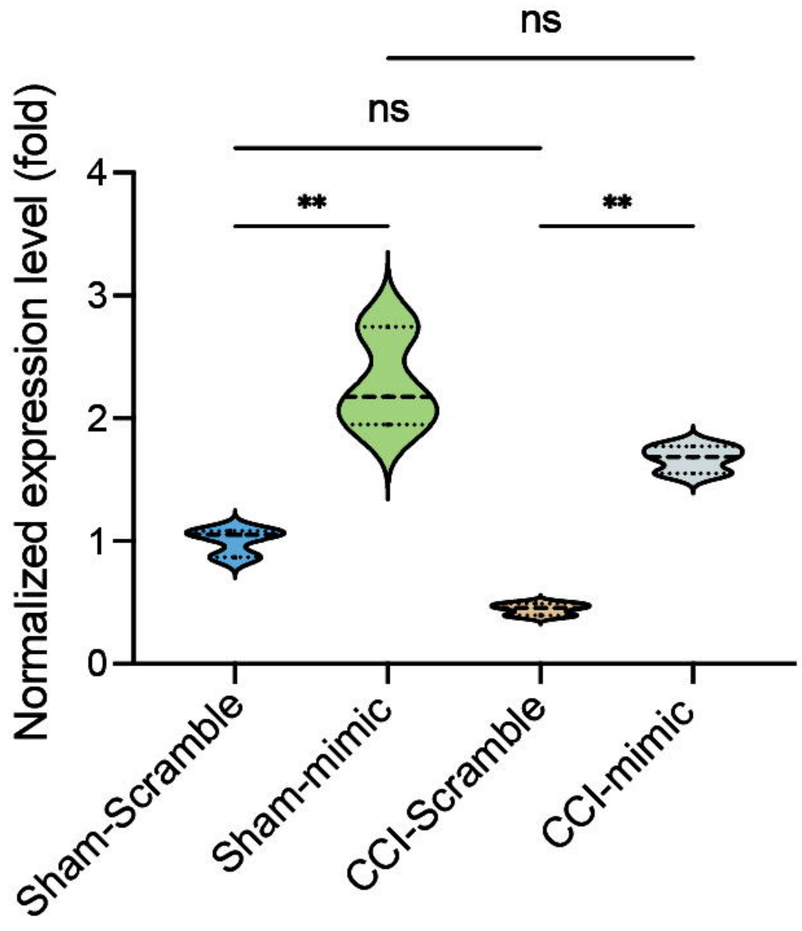

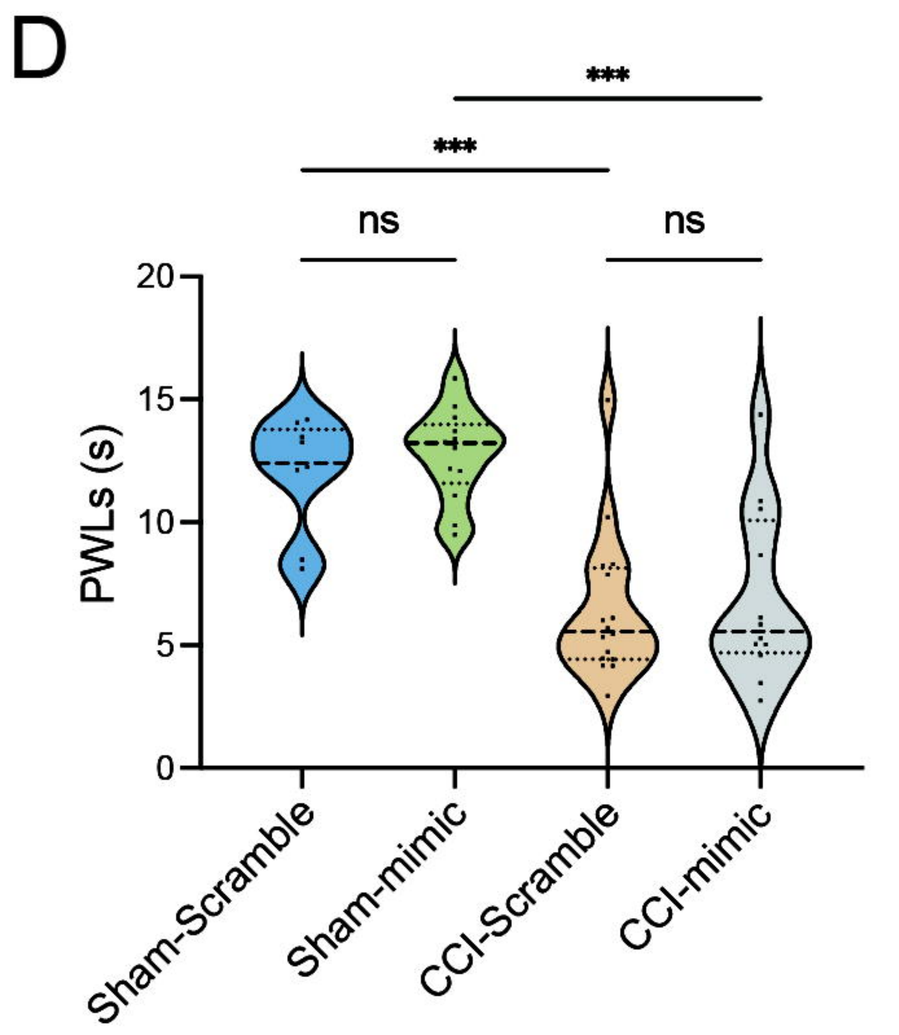

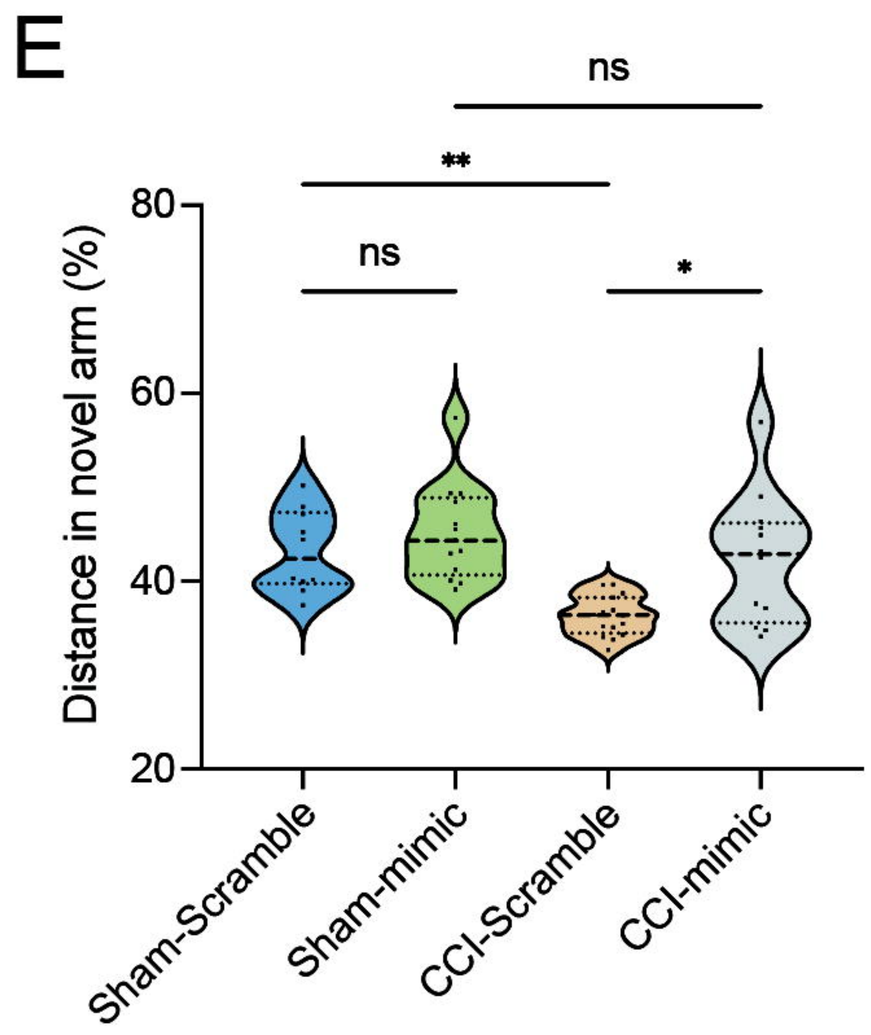

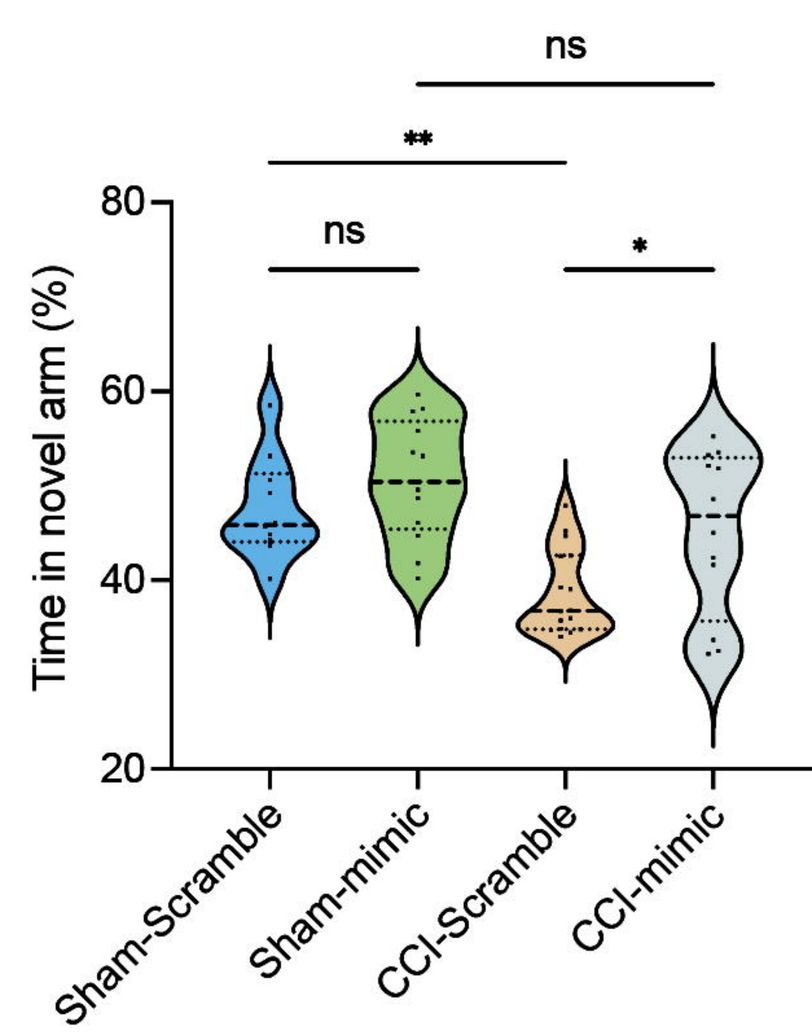

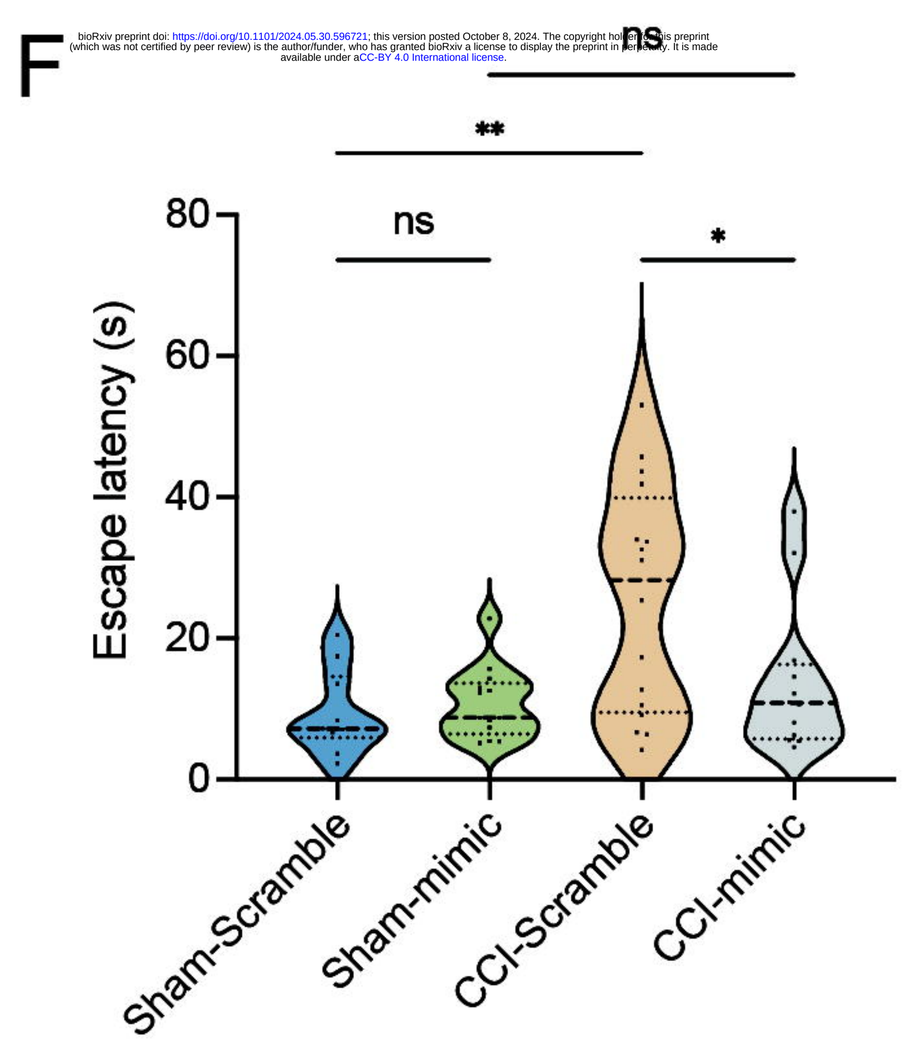

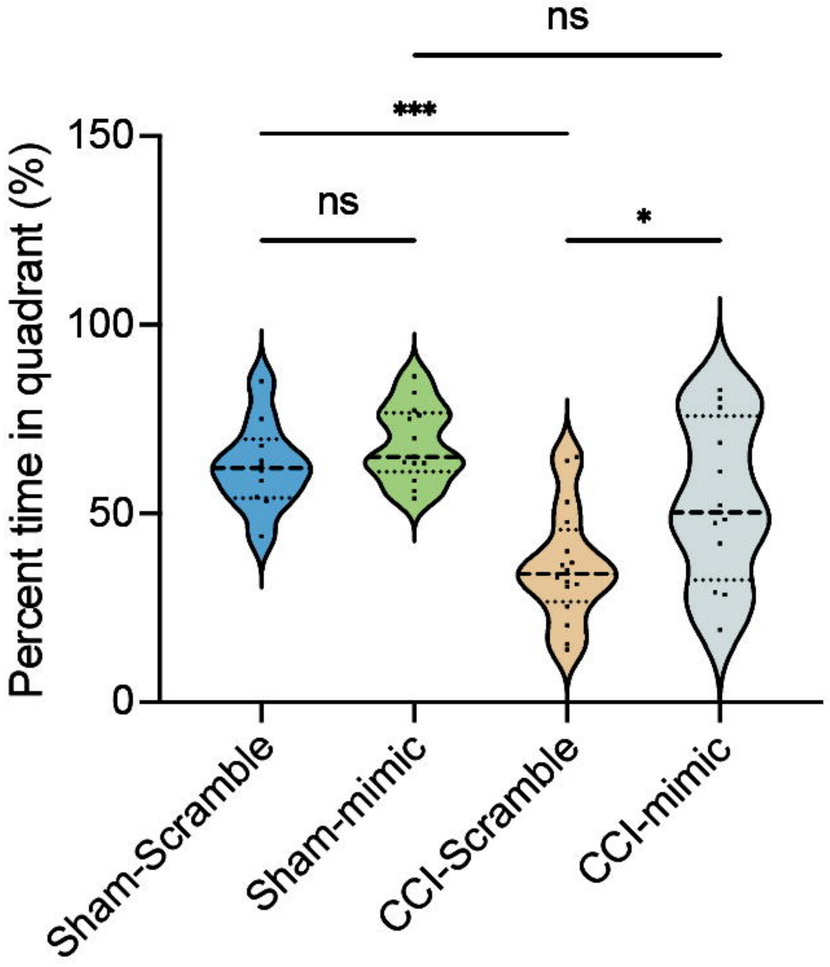

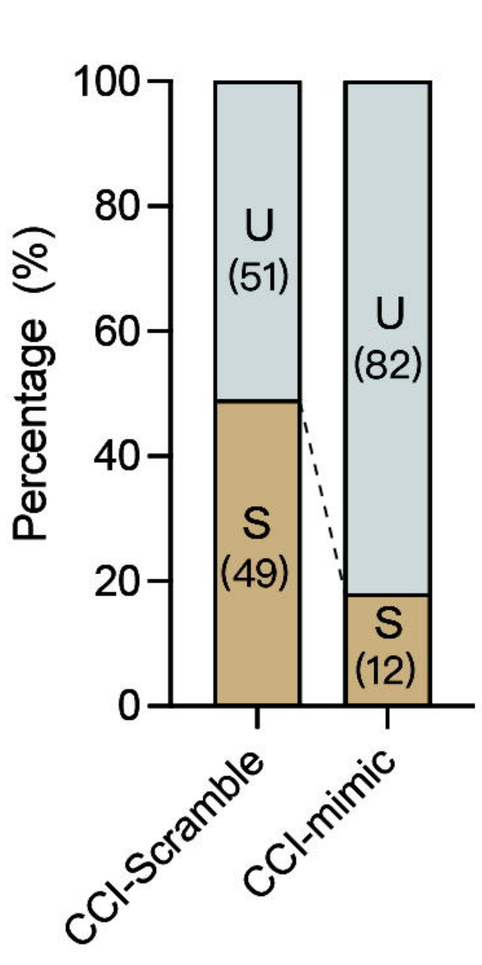

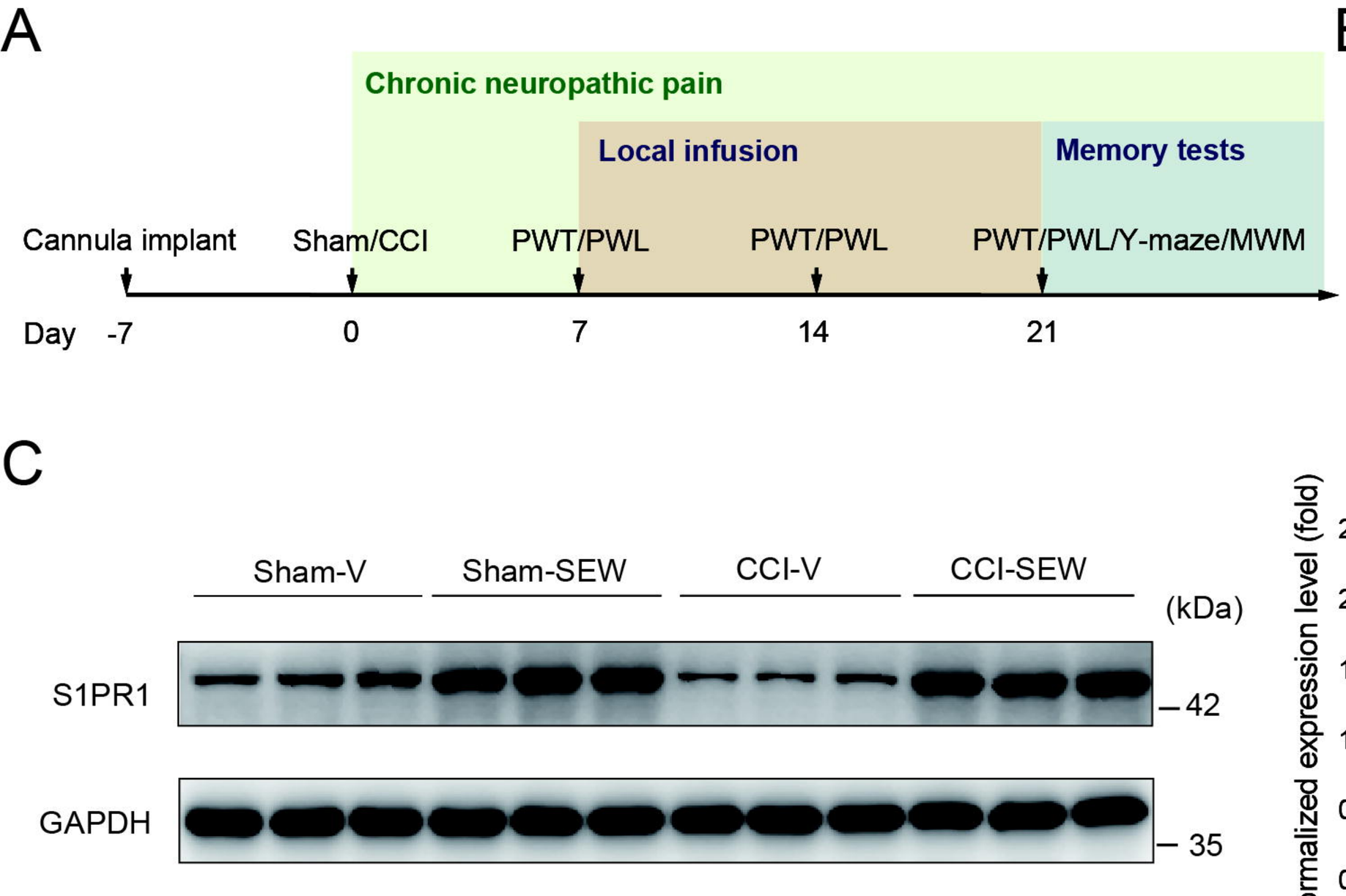

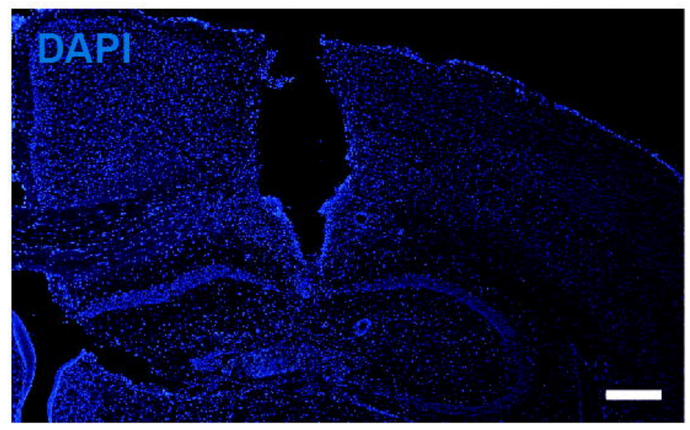

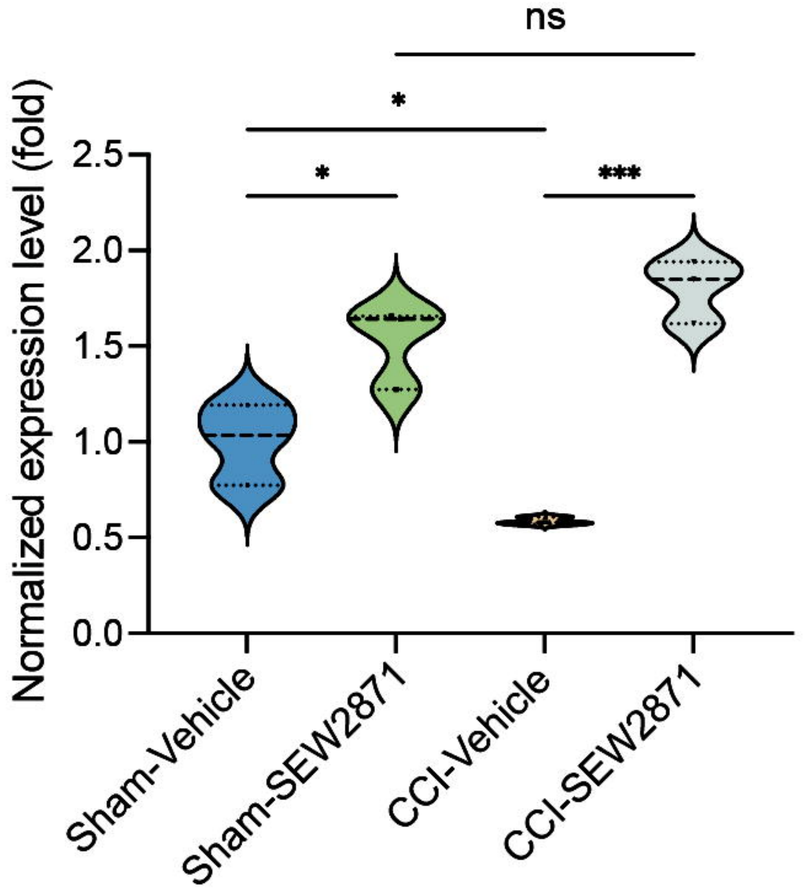

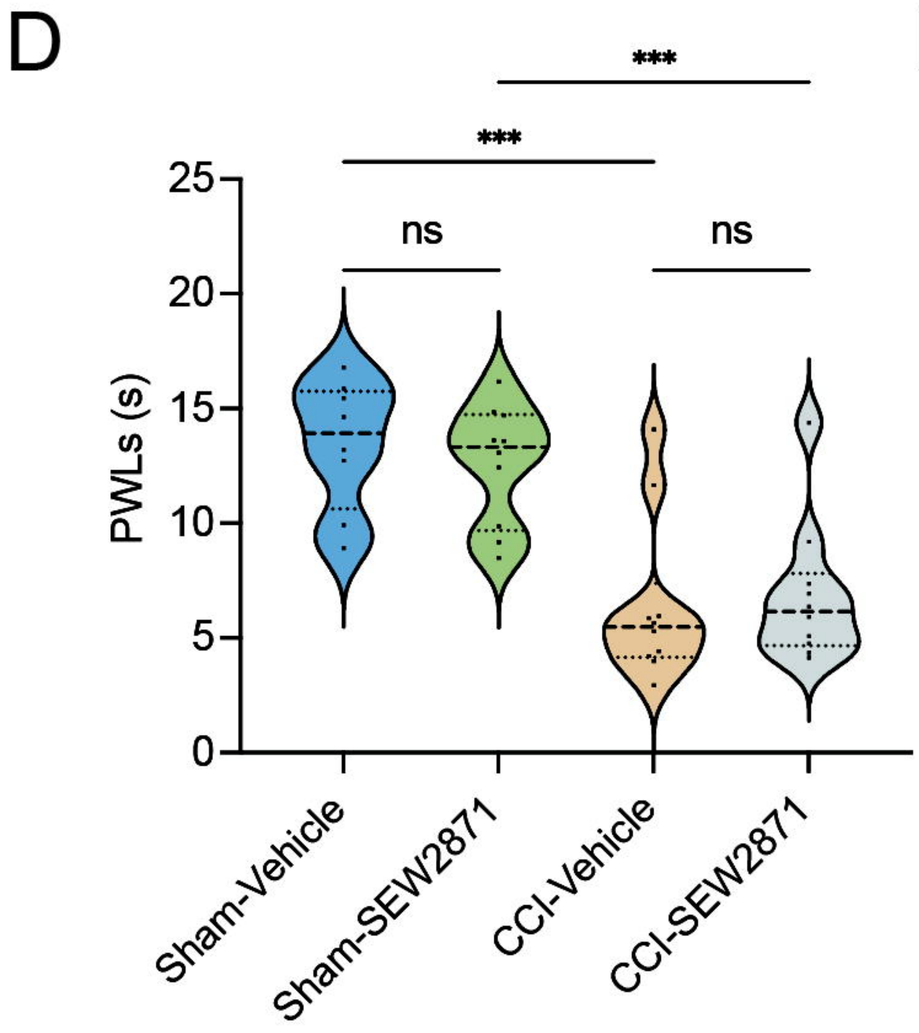

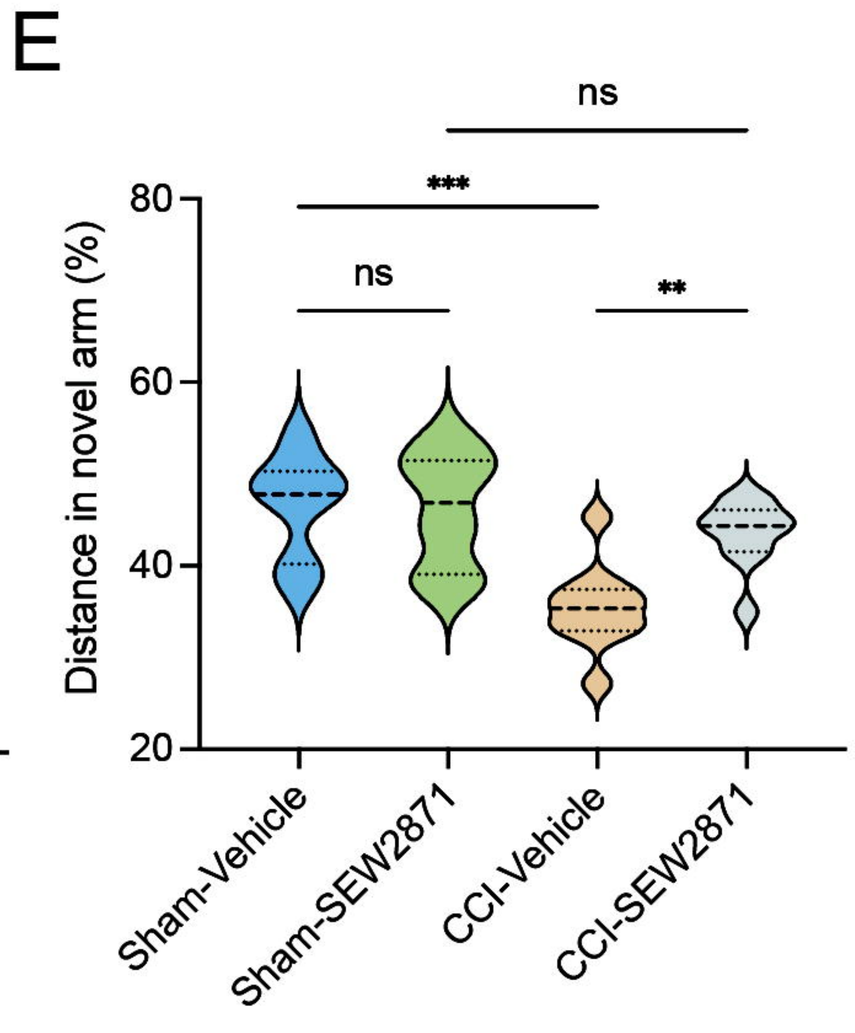

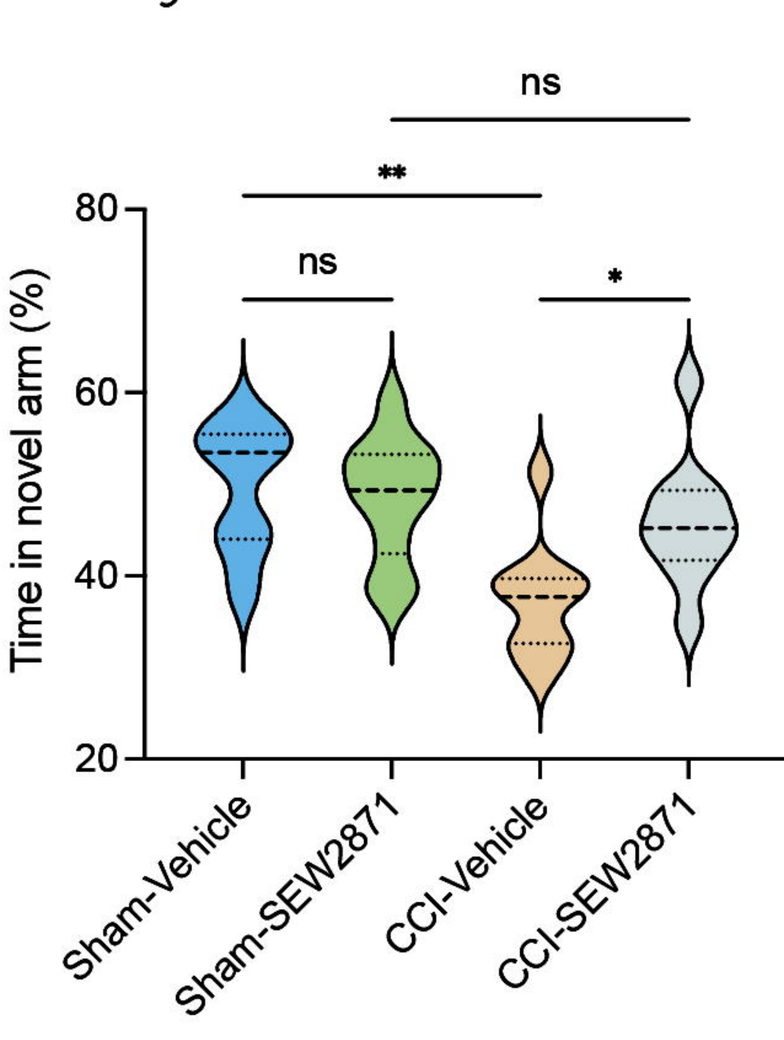

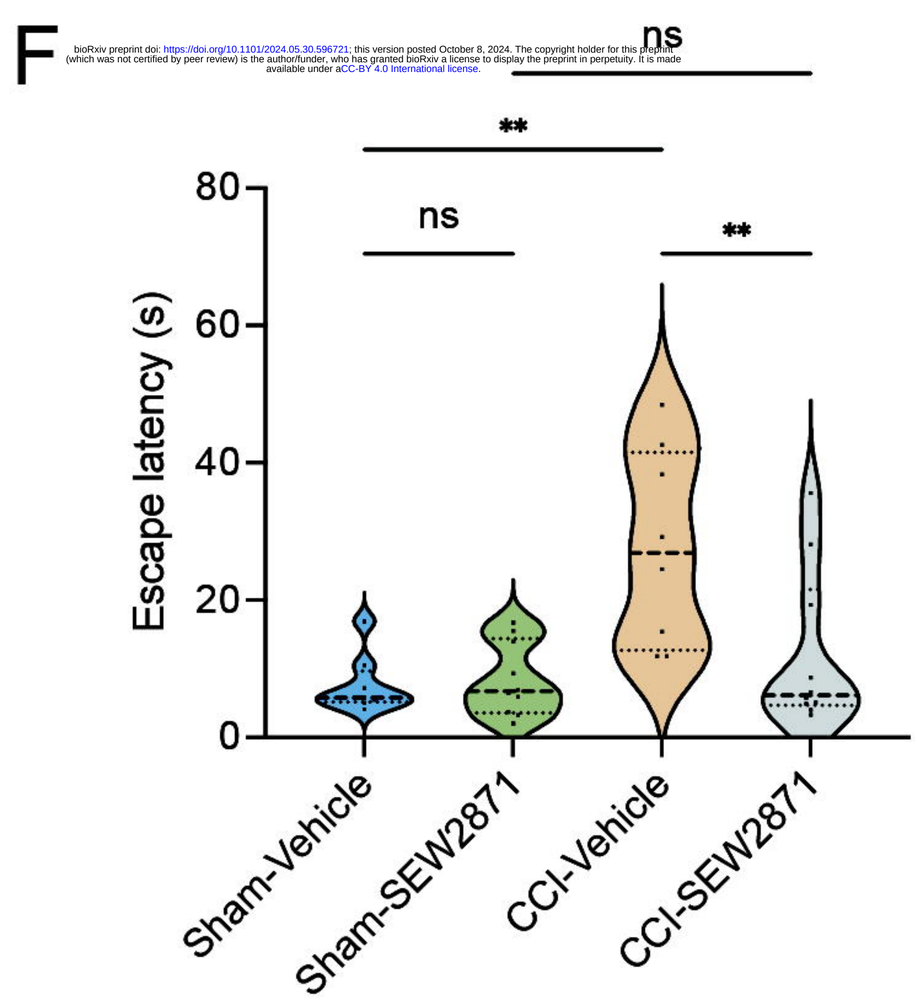

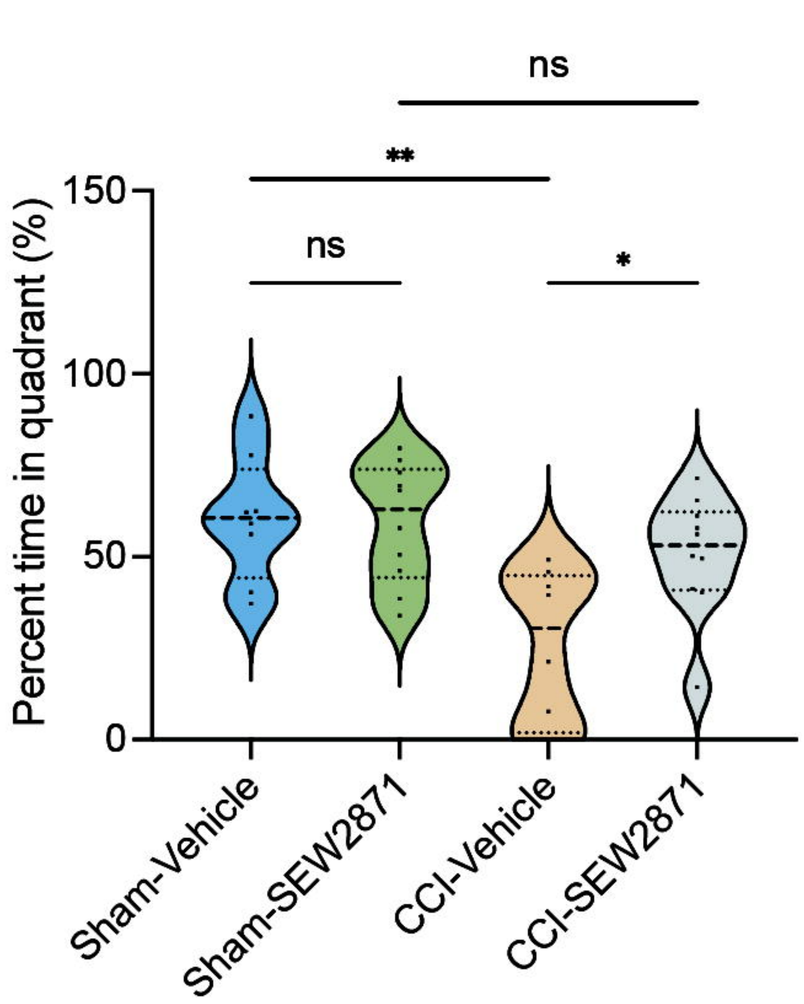

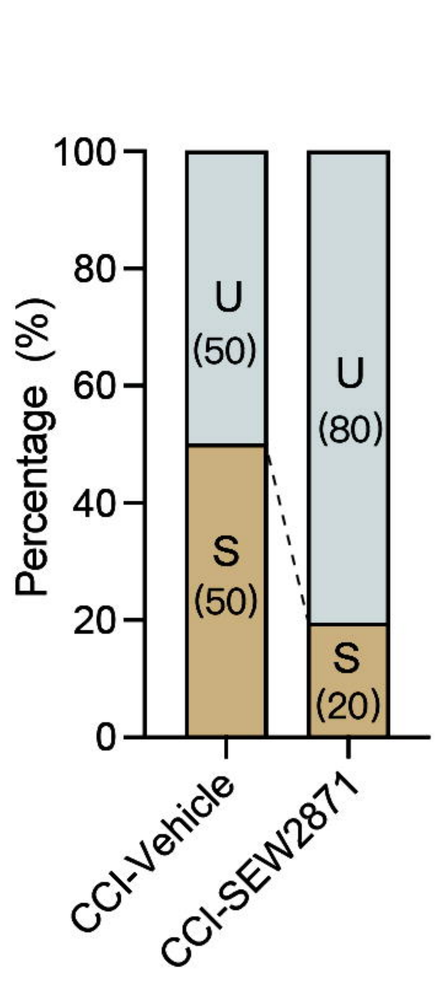

A

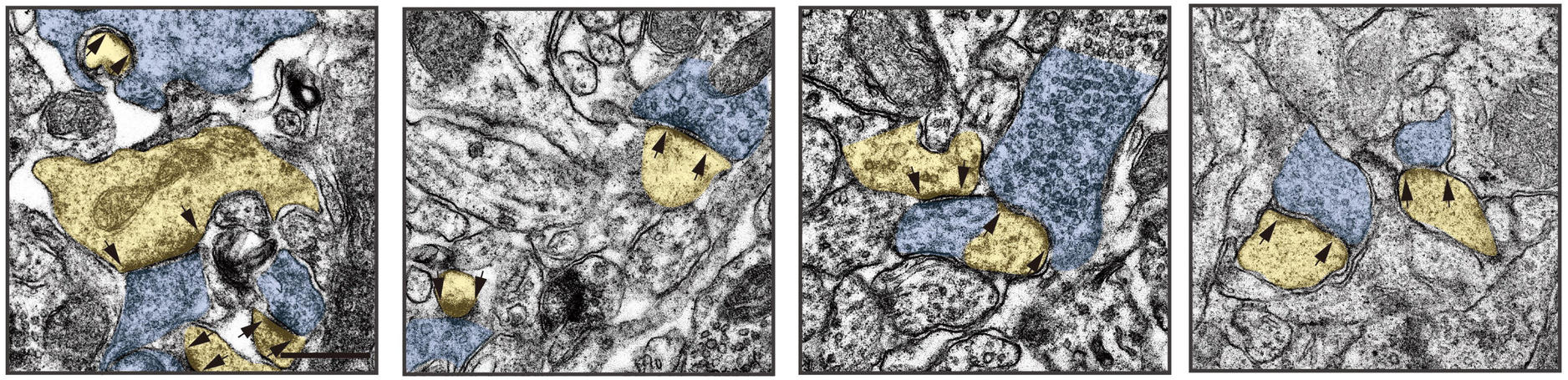
Sham-Scramble
Sham-shs1pr1
CCI-Scramble
CCI-shs1pr1

B

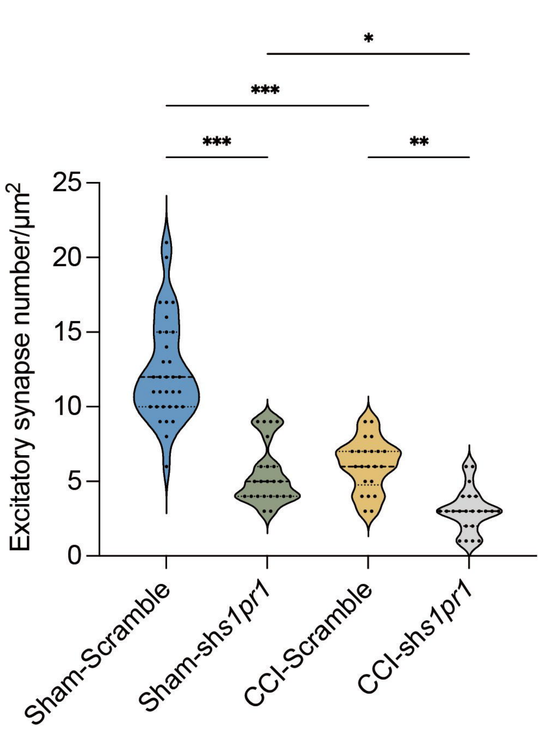
*
***
***
**
Excitatory synapse number/μm²
25
20
15
10
5
0
Sham-Scramble
Sham-shs1pr1
CCI-Scramble
CCI-shs1pr1

C

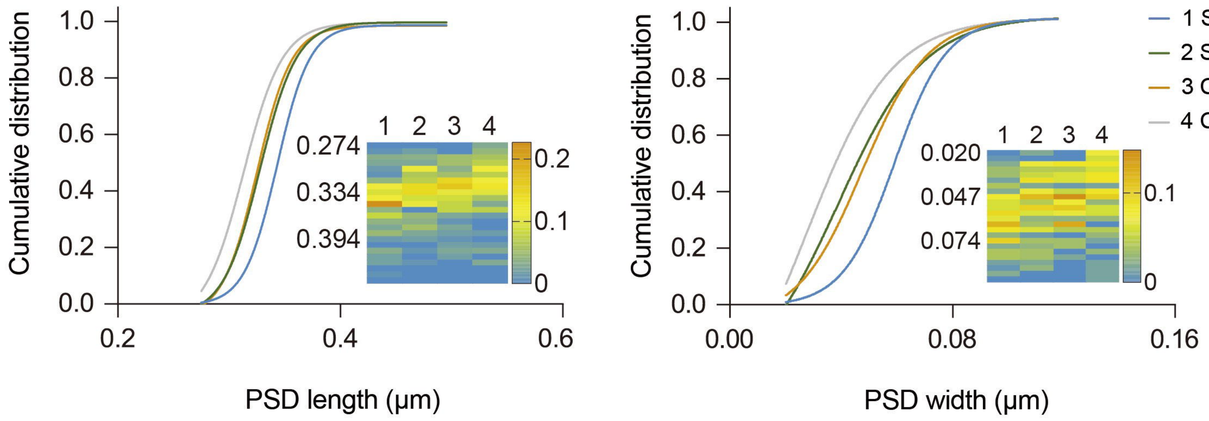
Cumulative distribution
1.0
0.8
0.6
0.4
0.2
0.0
0.2
0.4
0.6
PSD length (μm)
0.274
0.334
0.394
1 2 3 4
0.2
0.1
0
Cumulative distribution
0.00
0.08
0.16
PSD width (μm)
0.020
0.047
0.074
1 Sham-Scramble
2 Sham-shs1pr1
3 CCI-Scramble
4 CCI-shs1pr1

D

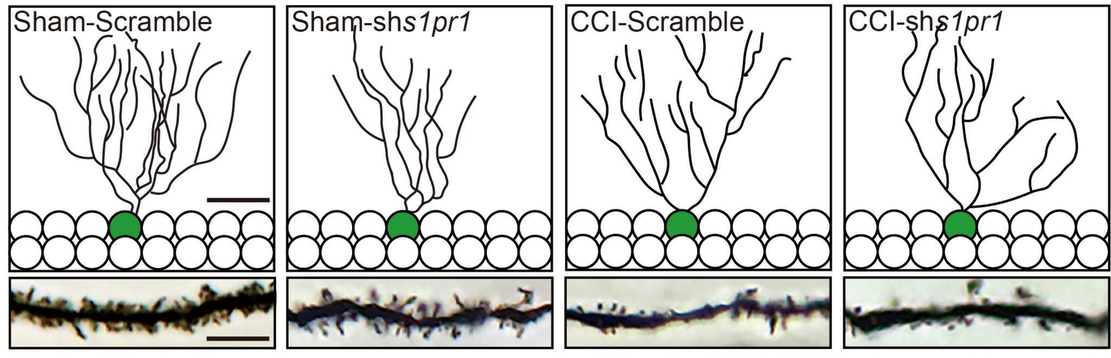
Sham-Scramble
Sham-shs1pr1
CCI-Scramble
CCI-shs1pr1

E

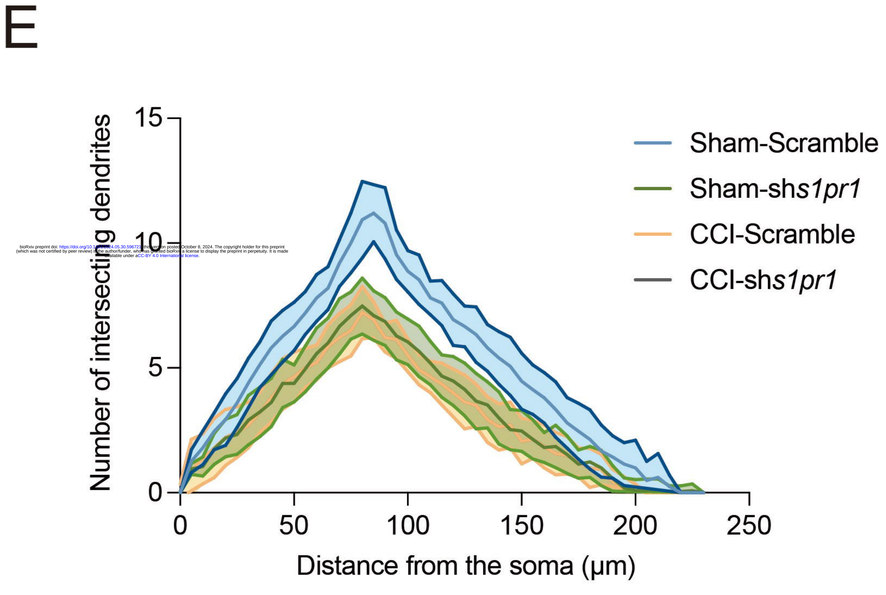
Number of intersecting dendrites
15
10
5
0
0
50
100
150
200
250
Distance from the soma (μm)
Sham-Scramble
Sham-shs1pr1
CCI-Scramble
CCI-shs1pr1

F

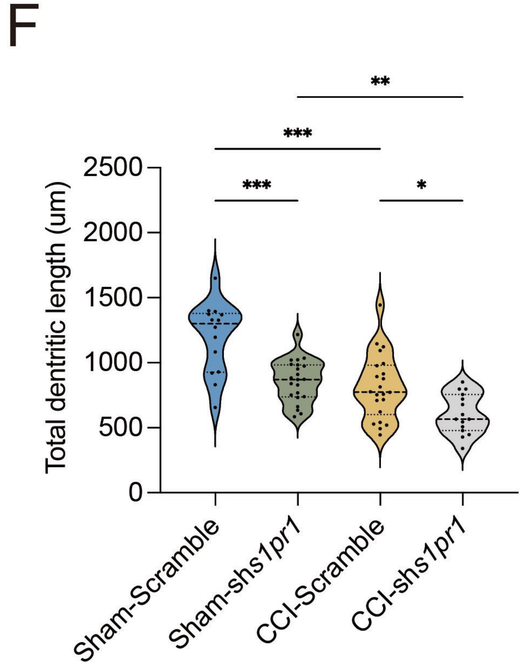
Total dentritic length (um)
2500
2000
1500
1000
500
0
**
***
***
*
Sham-Scramble
Sham-shs1pr1
CCI-Scramble
CCI-shs1pr1

G

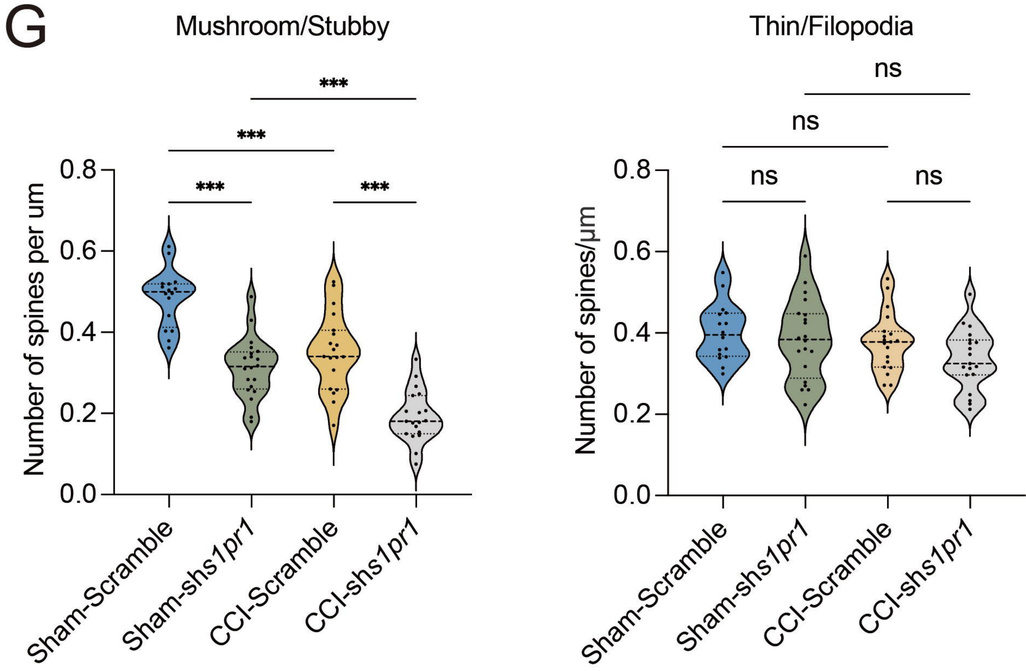
Mushroom/Stubby
Number of spines per um
0.8
0.6
0.4
0.2
0.0
***
***
***
Thin/Filopodia
Number of spines/μm
ns
ns
ns
ns
Sham-Scramble
Sham-shs1pr1
CCI-Scramble
CCI-shs1pr1

A

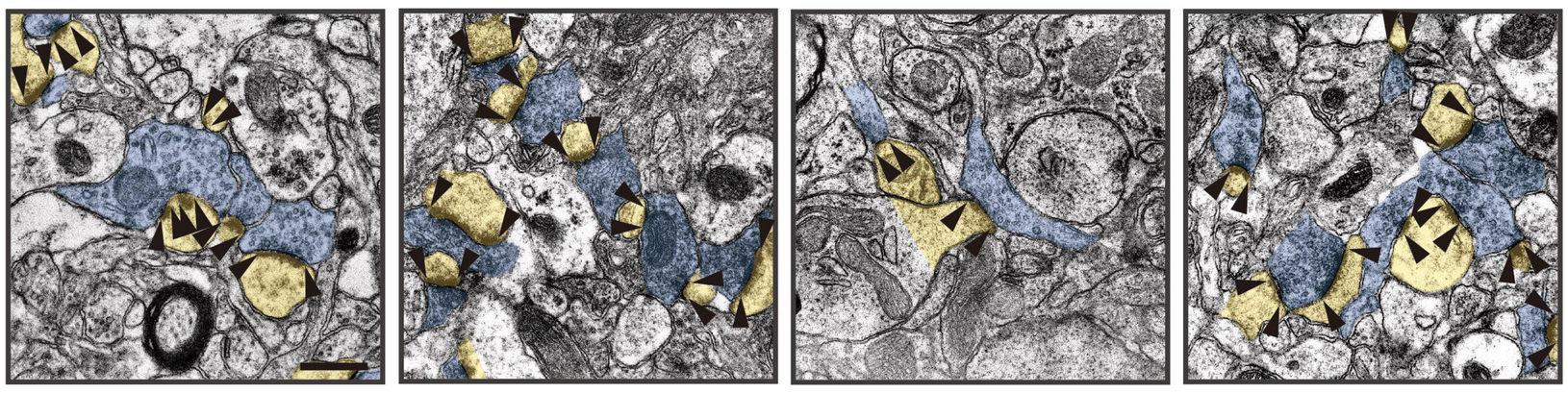

B

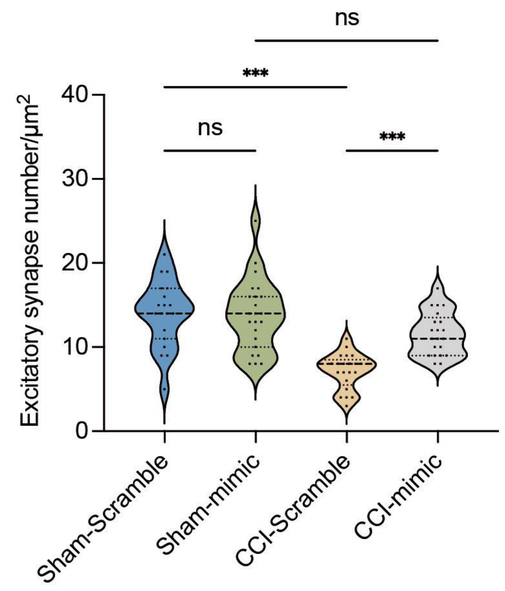

C

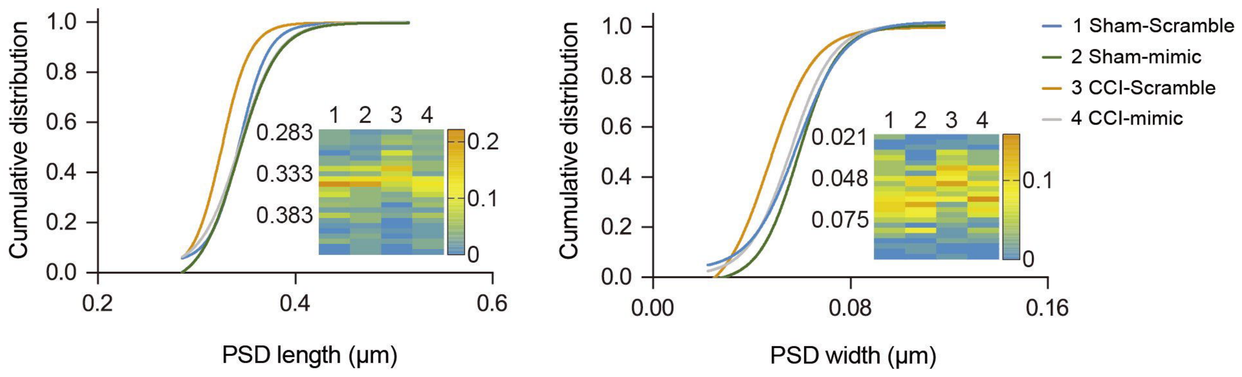

D

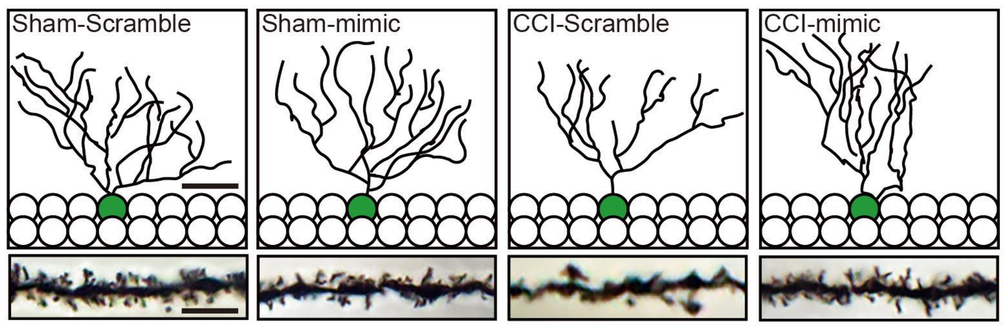

E

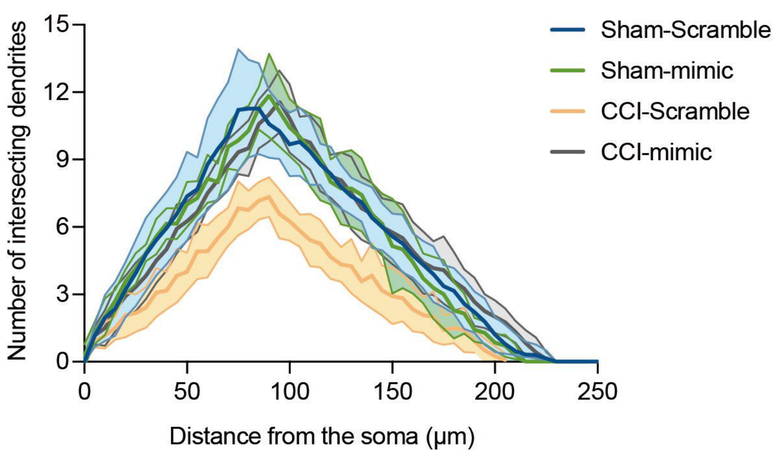

F

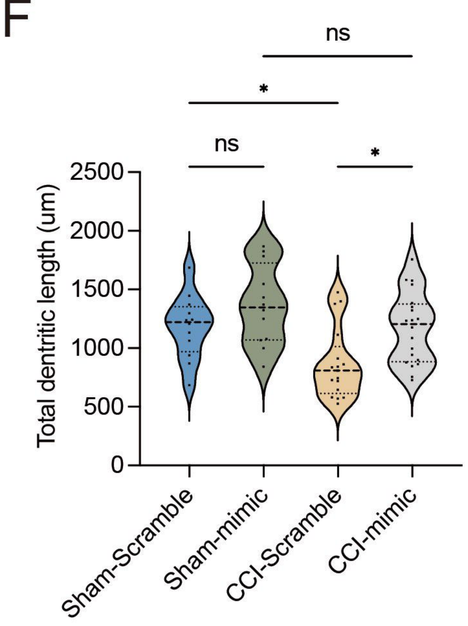

G

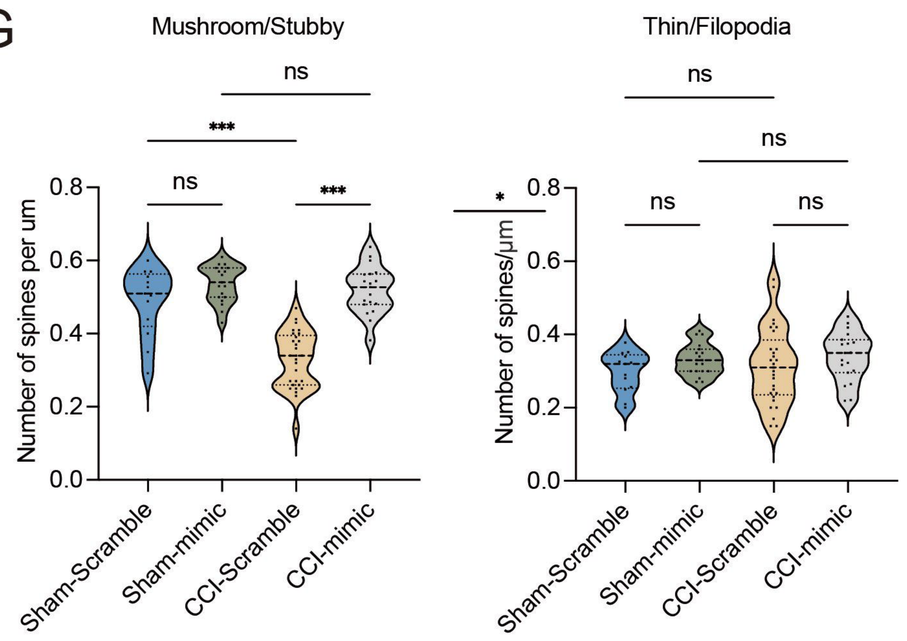

H

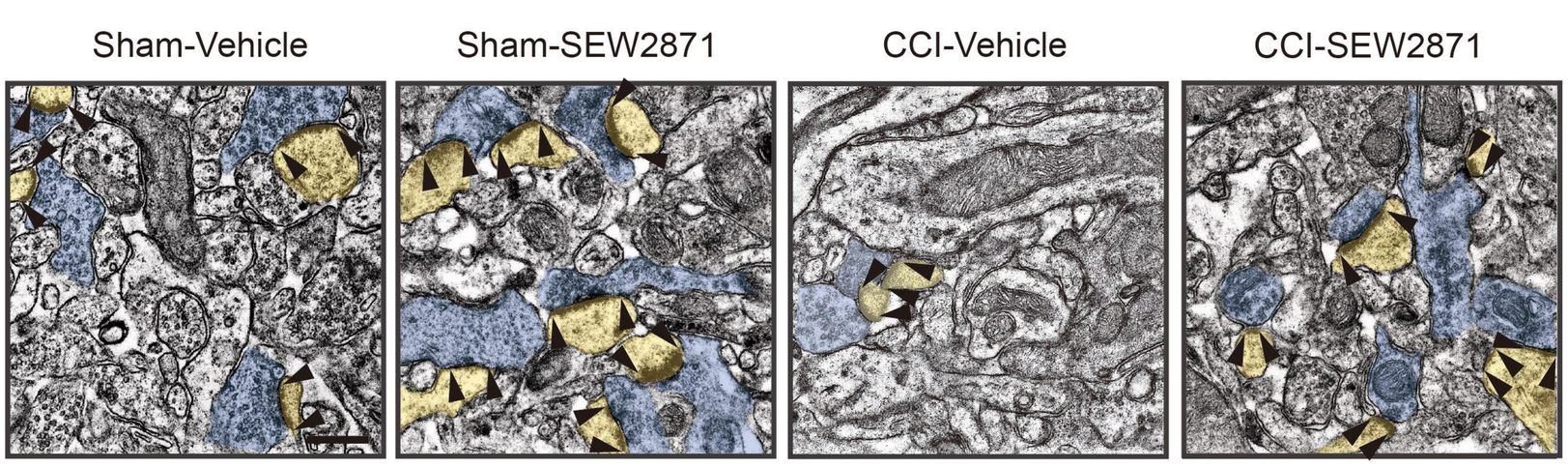

I

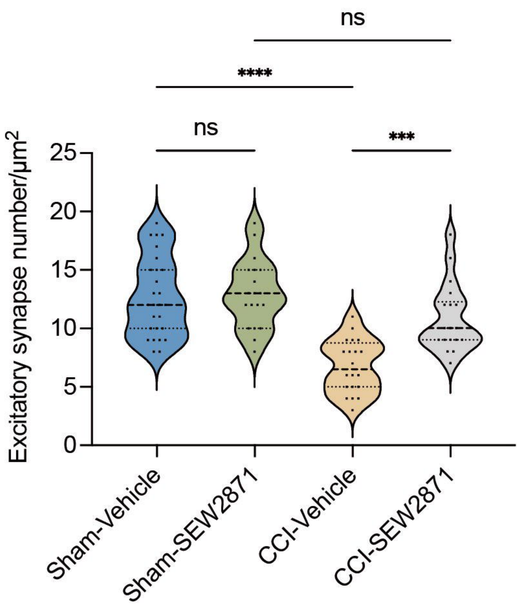

J

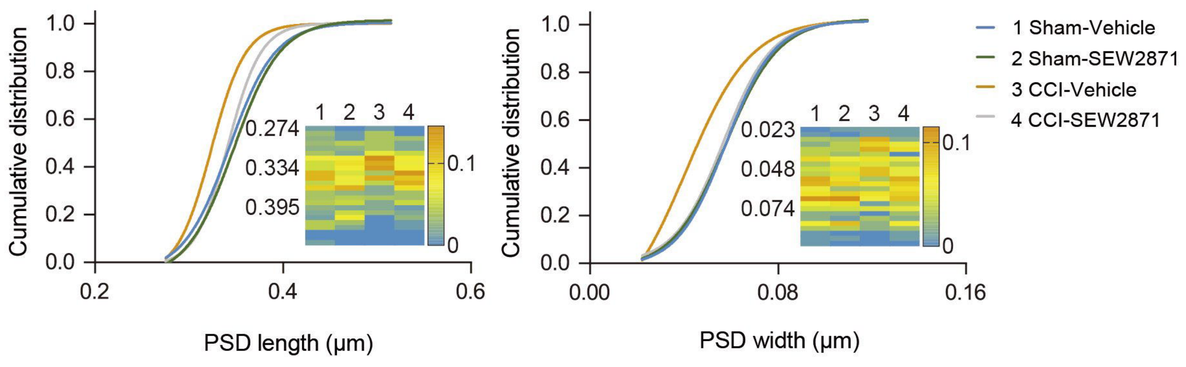

K

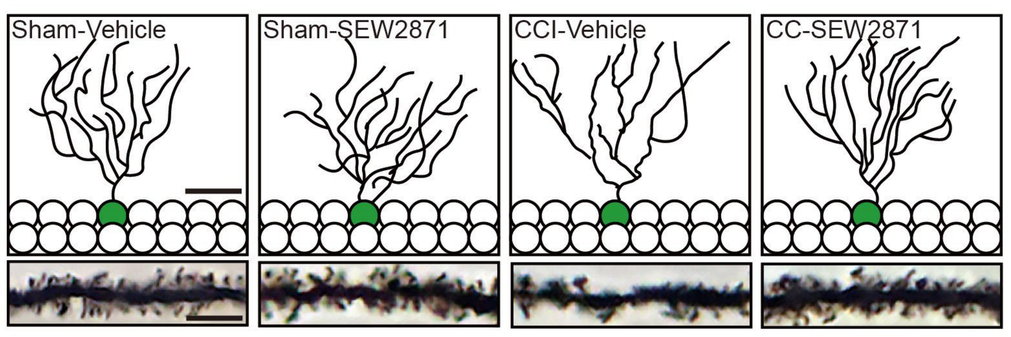

L

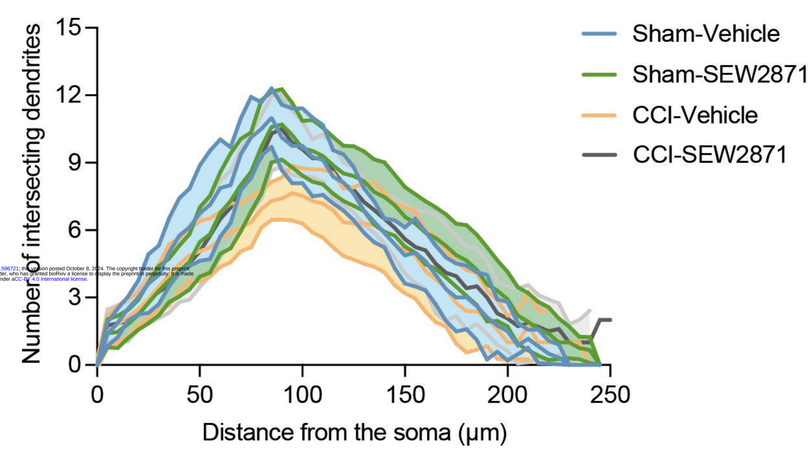

M

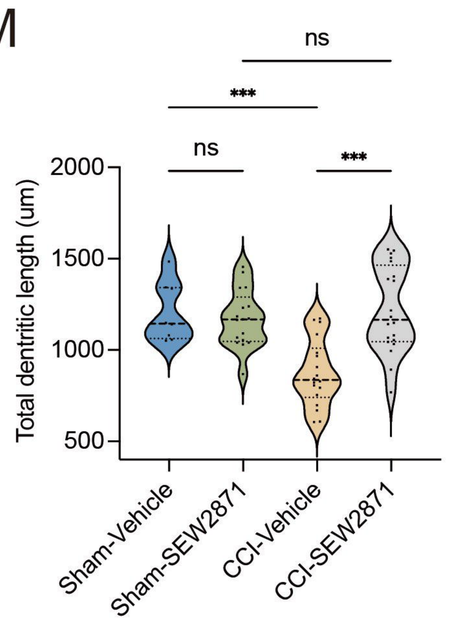

N

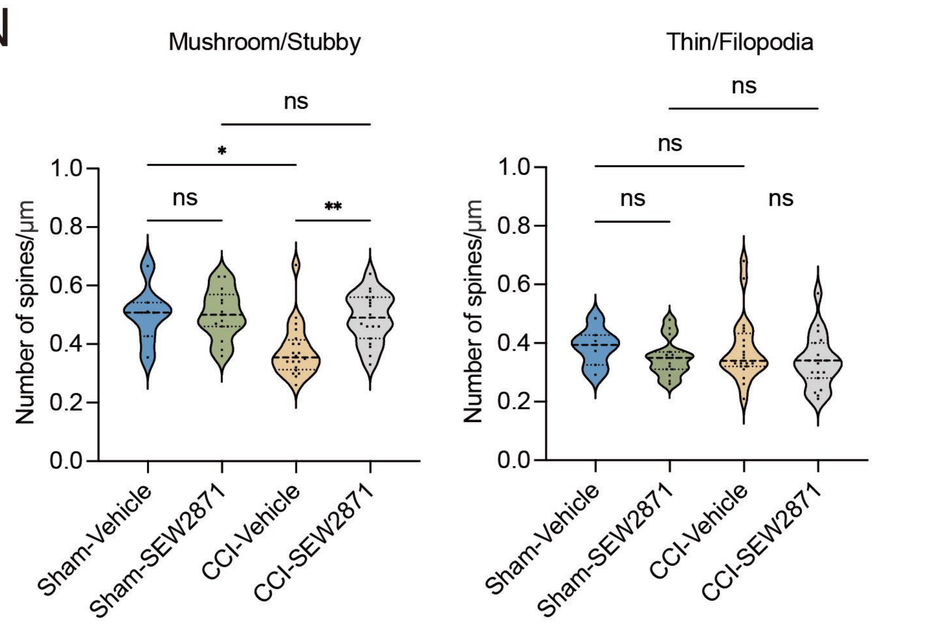

A

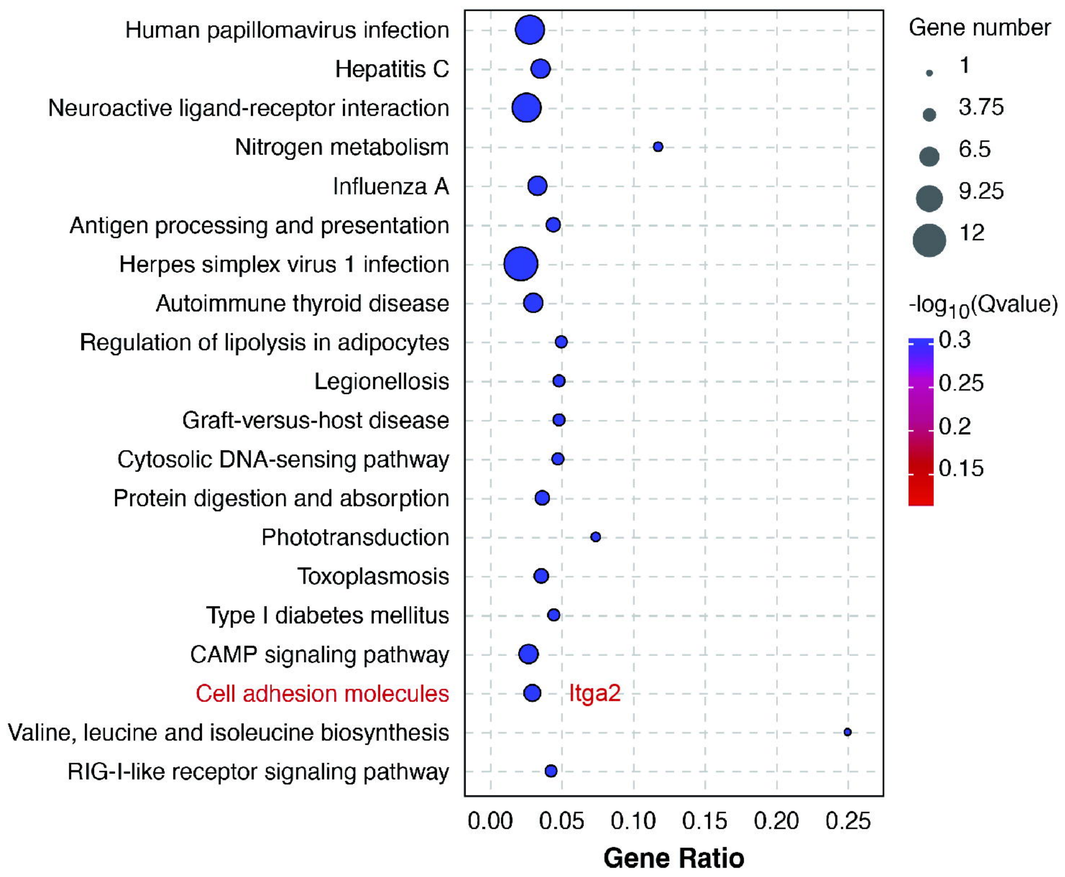
Top 20 KEGG pathway enriment (Sham vs S)
Human papillomavirus infection
Hepatitis C
Neuroactive ligand-receptor interaction
Nitrogen metabolism
Influenza A
Antigen processing and presentation
Herpes simplex virus 1 infection
Autoimmune thyroid disease
Regulation of lipolysis in adipocytes
Legionellosis
Graft-versus-host disease
Cytosolic DNA-sensing pathway
Protein digestion and absorption
Phototransduction
Toxoplasmosis
Type I diabetes mellitus
CAMP signaling pathway
Cell adhesion molecules
Itga2
Valine, leucine and isoleucine biosynthesis
RIG-I-like receptor signaling pathway
0.00 0.05 0.10 0.15 0.20 0.25
Gene Ratio
Gene number
1
3.75
6.5
9.25
12
-log10(Qvalue)
0.3
0.25
0.2
0.15

B

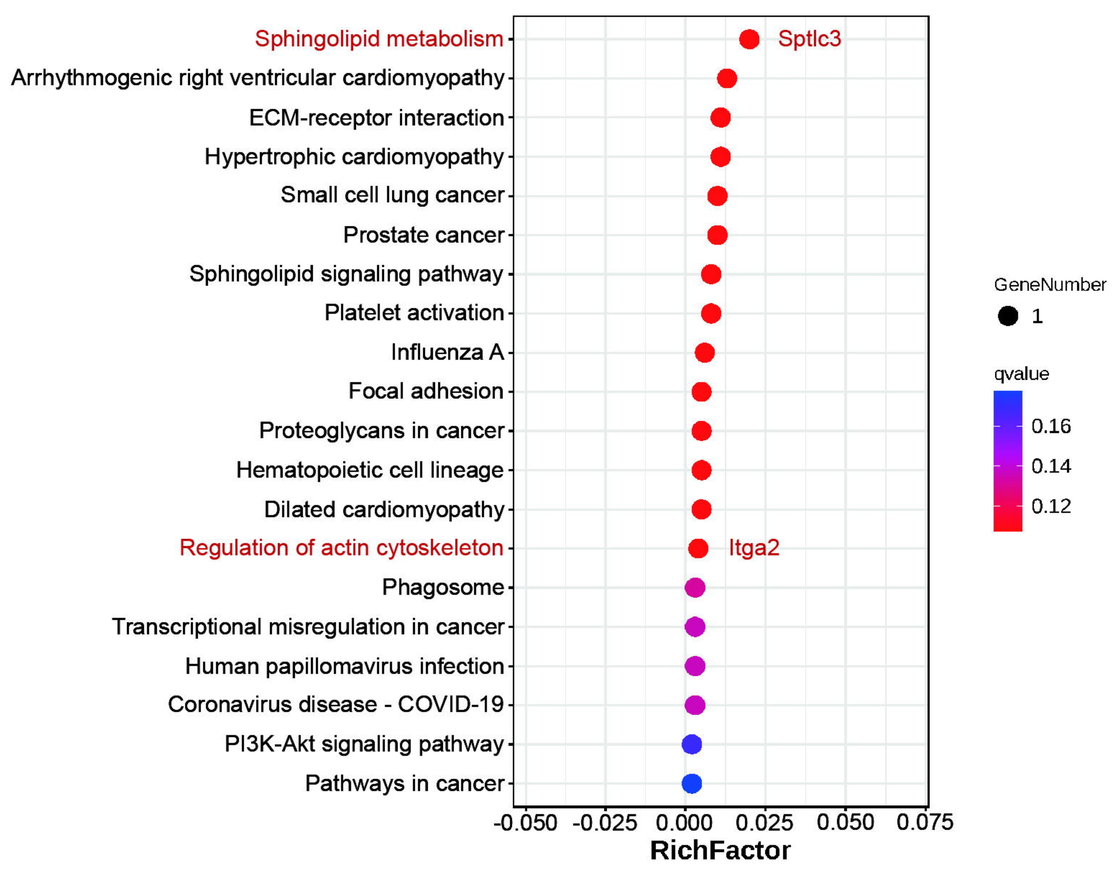
Top 20 KEGG pathway enriment (Sham vs U vs S trend analysis)
Sphingolipid metabolism
Sptlc3
Arrhythmogenic right ventricular cardiomyopathy
ECM-receptor interaction
Hypertrophic cardiomyopathy
Small cell lung cancer
Prostate cancer
Sphingolipid signaling pathway
Platelet activation
Influenza A
Focal adhesion
Proteoglycans in cancer
Hematopoietic cell lineage
Dilated cardiomyopathy
Regulation of actin cytoskeleton
Itga2
Phagosome
Transcriptional misregulation in cancer
Human papillomavirus infection
Coronavirus disease - COVID-19
PI3K-Akt signaling pathway
Pathways in cancer
-0.050 -0.025 0.000 0.025 0.050 0.075
RichFactor
GeneNumber
1
qvalue
0.16
0.14
0.12

C

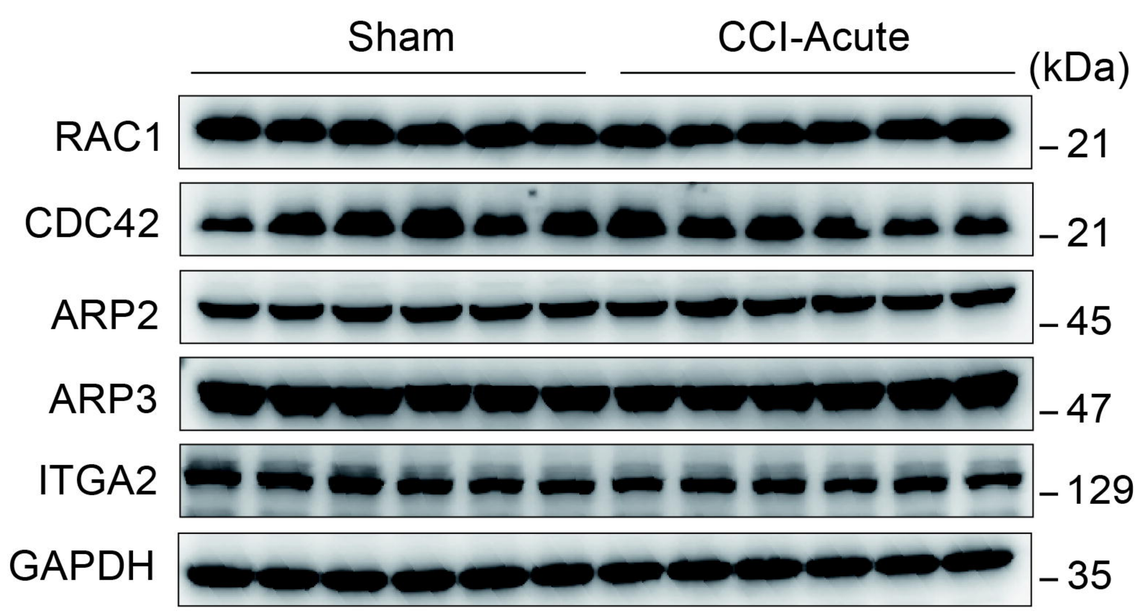
Sham
CCI-Acute
(kDa)
RAC1
21
CDC42
21
ARP2
45
ARP3
47
ITGA2
129
GAPDH
35

D

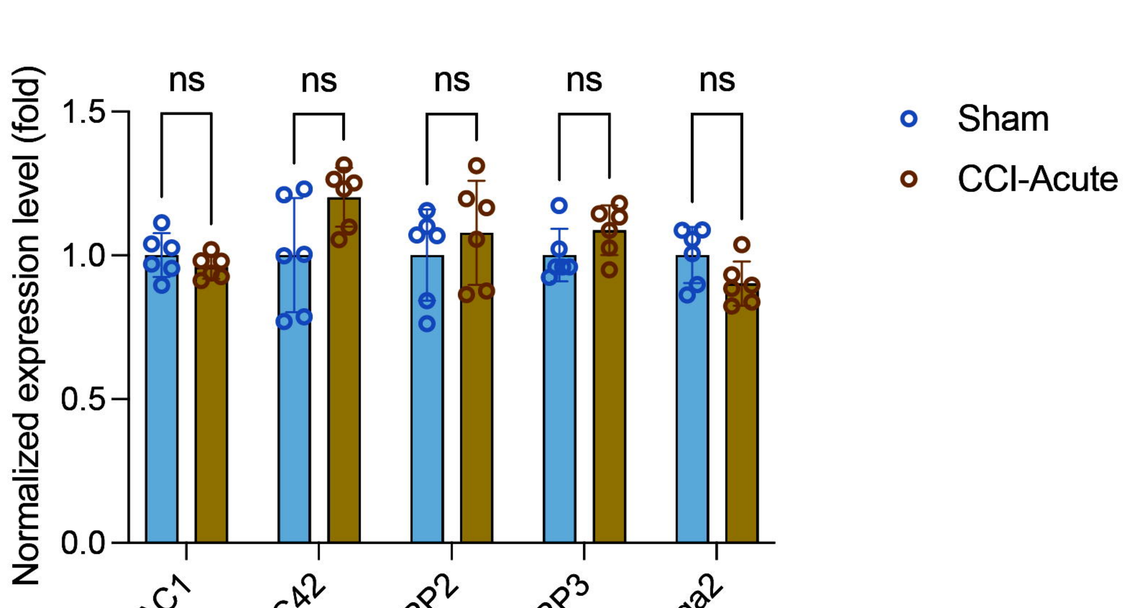
Normalized expression level (fold)
ns
1.5
1.0
0.5
0.0
RAC1
CDC42
ARP2
ARP3
Itga2
Sham
CCI-Acute

E

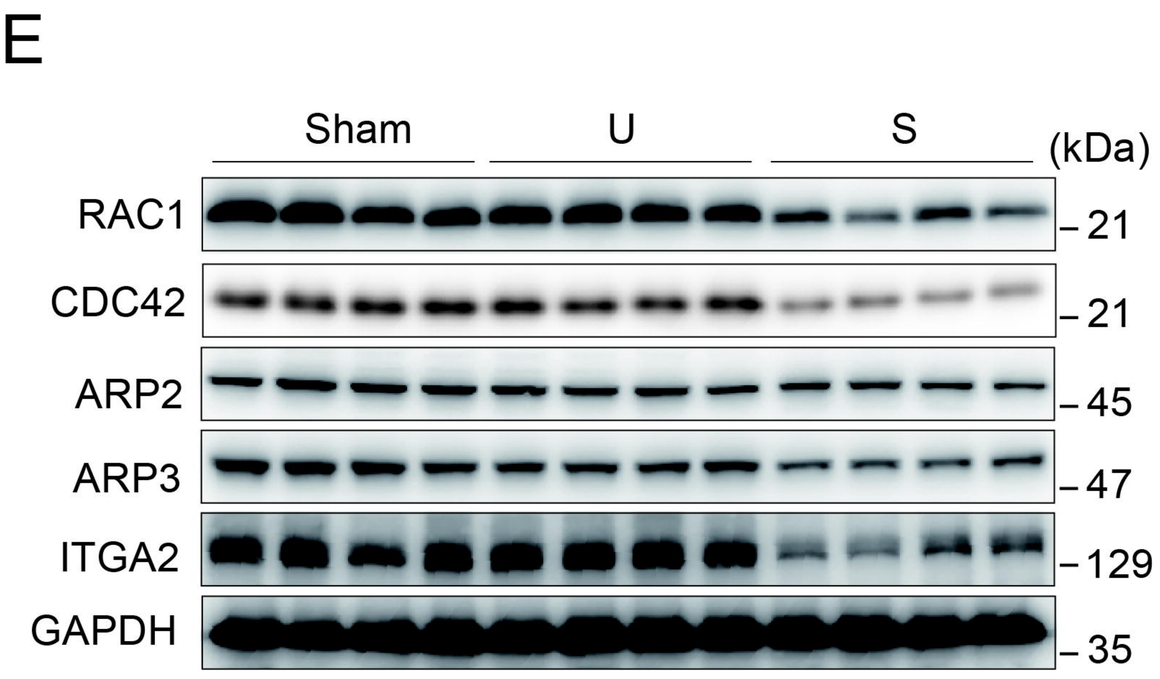
Sham
U
S
(kDa)
RAC1
21
CDC42
21
ARP2
45
ARP3
47
ITGA2
129
GAPDH
35

F

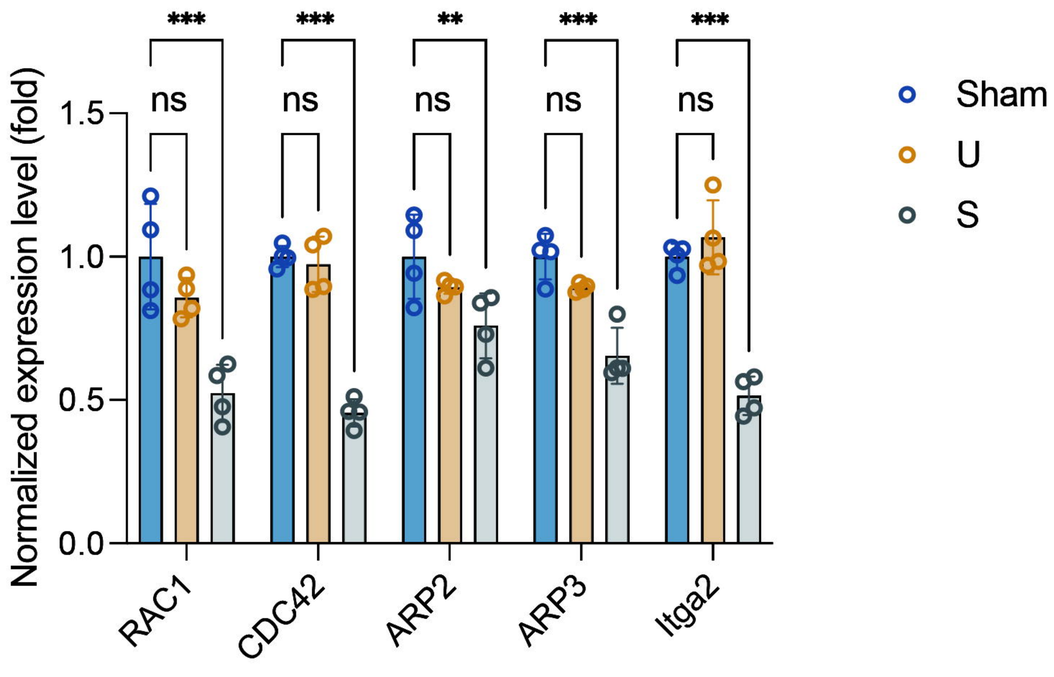
Normalized expression level (fold)
***
**
ns
1.5
1.0
0.5
0.0
RAC1
CDC42
ARP2
ARP3
Itga2
Sham
U
S

G

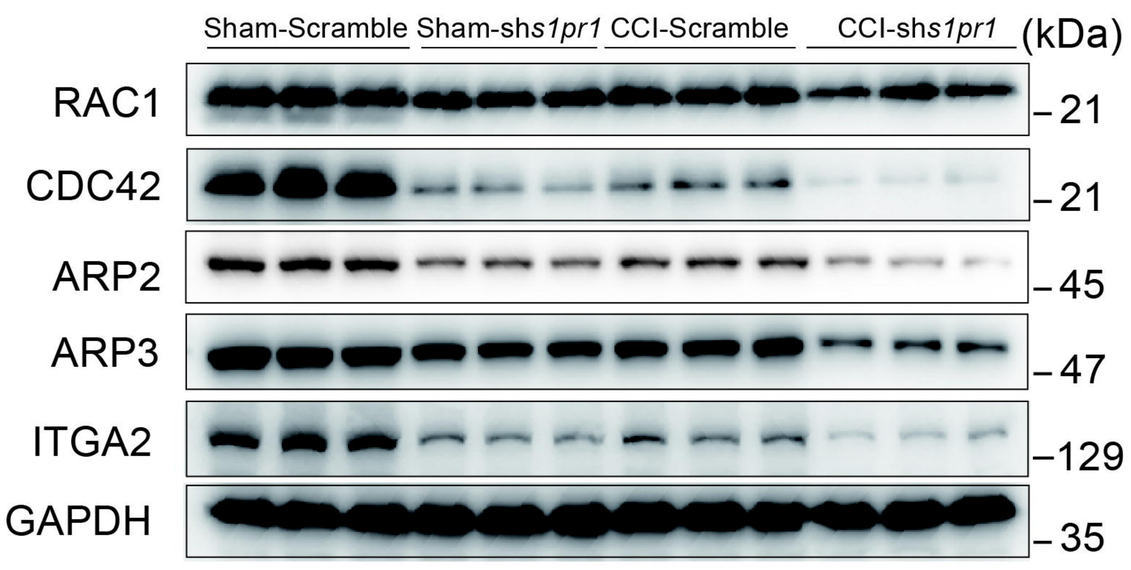
Sham-Scramble
Sham-shs1pr1
CCI-Scramble
CCI-shs1pr1
(kDa)
RAC1
21
CDC42
21
ARP2
45
ARP3
47
ITGA2
129
GAPDH
35

H

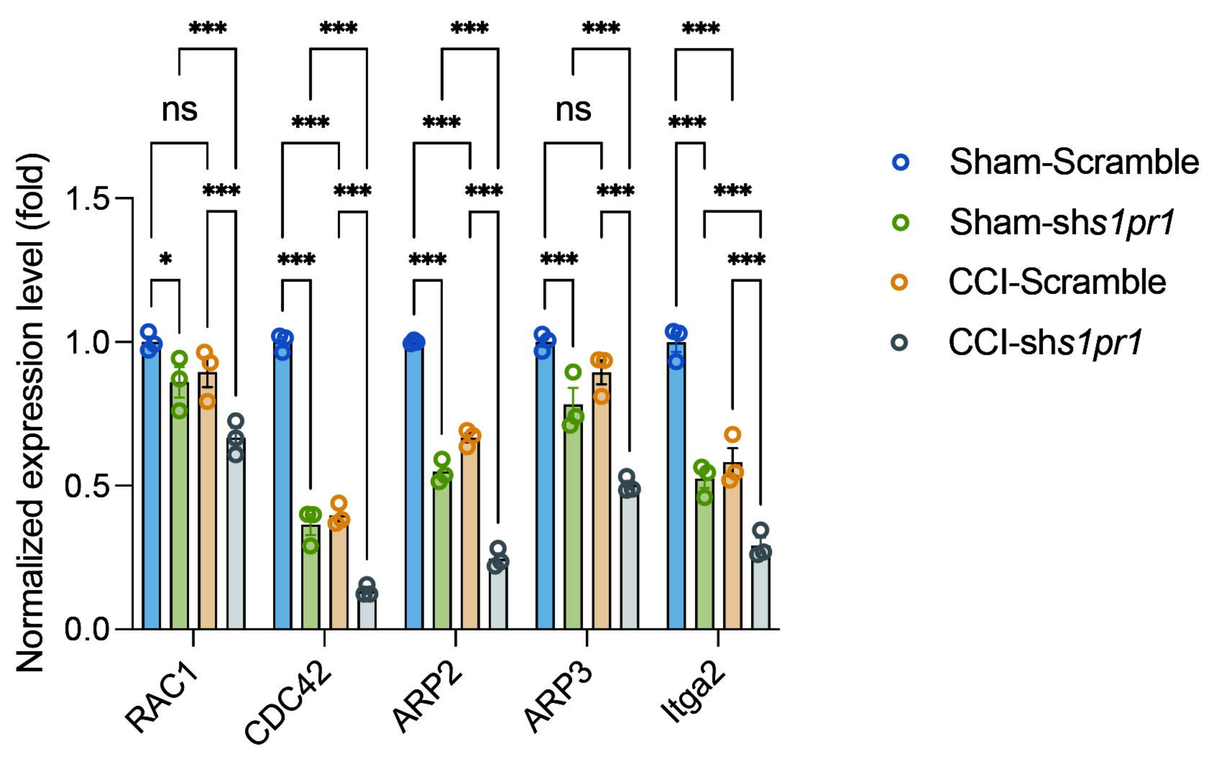
Normalized expression level (fold)
***
*
ns
1.5
1.0
0.5
0.0
RAC1
CDC42
ARP2
ARP3
Itga2
Sham-Scramble
Sham-shs1pr1
CCI-Scramble
CCI-shs1pr1

I

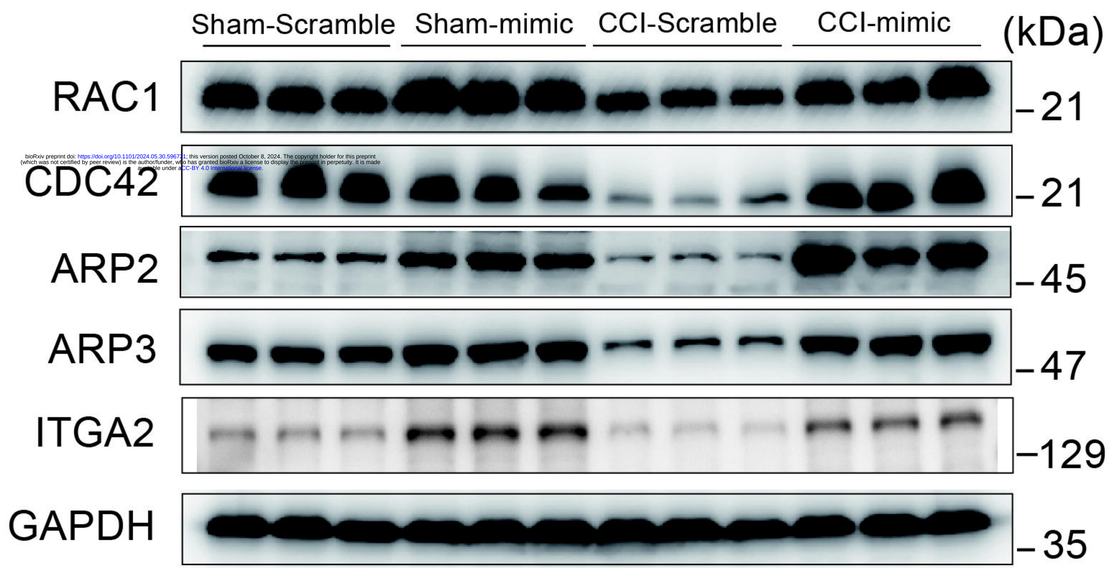
Sham-Scramble
Sham-mimic
CCI-Scramble
CCI-mimic
(kDa)
RAC1
21
CDC42
21
ARP2
45
ARP3
47
ITGA2
129
GAPDH
35

J

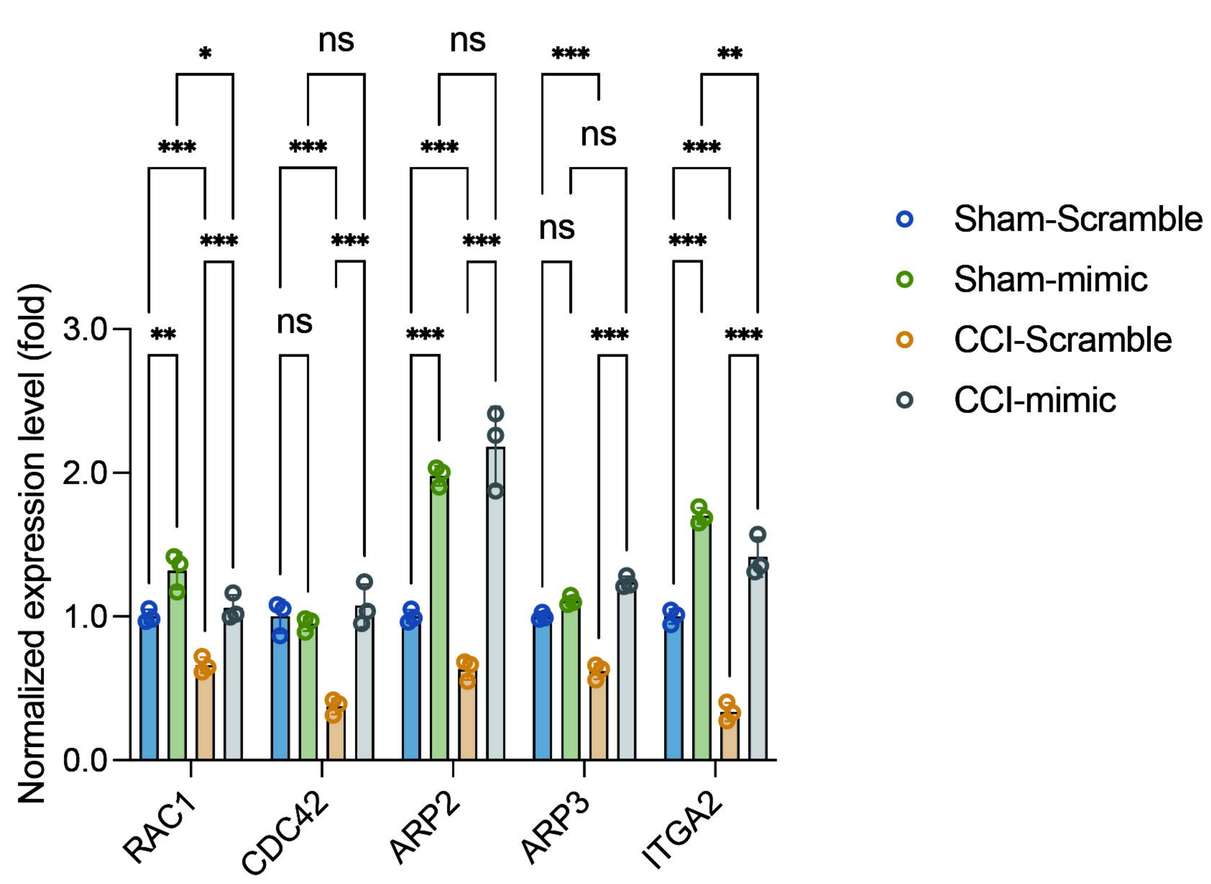
Normalized expression level (fold)
***
**
*
ns
3.0
2.0
1.0
0.0
RAC1
CDC42
ARP2
ARP3
ITGA2
Sham-Scramble
Sham-mimic
CCI-Scramble
CCI-mimic

A Animal model

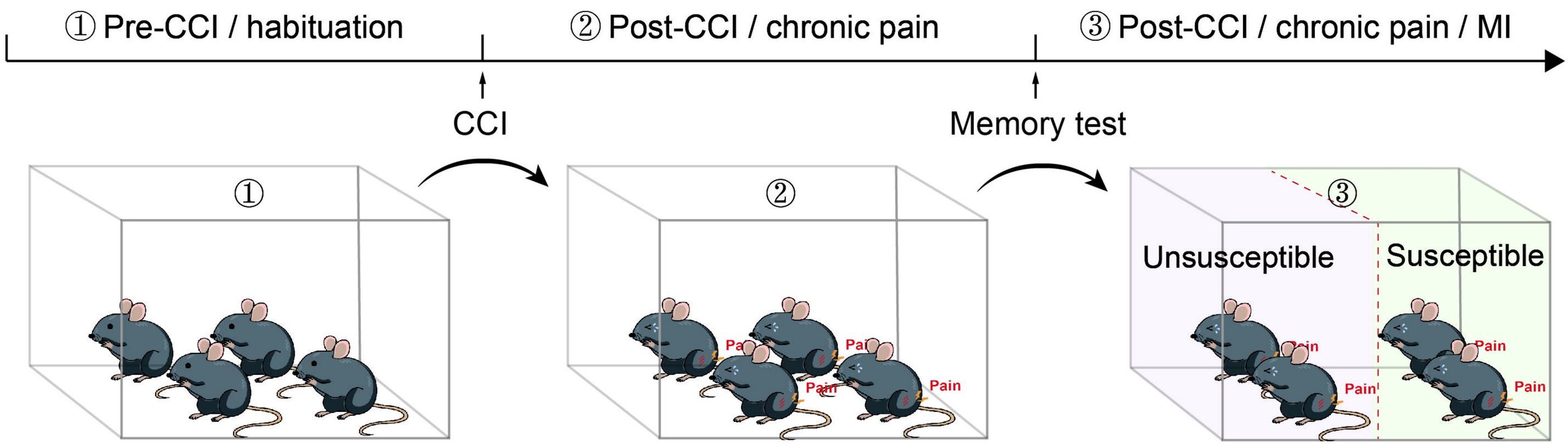

B Signaling (synapse)